

# Contents

<b>Introduction</b>	<b>1</b>
Outline . . . . .	2
<b>1 Model</b>	<b>3</b>
1.1 Spinless extended Hubbard model . . . . .	3
1.1.1 Hamiltonian . . . . .	3
1.1.2 Mapping on 1D Hamiltonian . . . . .	5
1.2 Exact calculations without electron-electron interaction . . . . .	6
1.2.1 Tight binding chain . . . . .	6
1.2.2 Tight binding ladder . . . . .	10
1.3 Exact calculations with electron-electron interaction . . . . .	12
1.3.1 Infinitely-strong correlated hops . . . . .	14
1.3.2 Zero inter-leg hopping . . . . .	15
1.3.3 Very strong inter-leg hopping . . . . .	15
<b>2 Matrix product state method for finite systems</b>	<b>17</b>
2.1 Matrix product states . . . . .	17
2.1.1 Construction of matrix product states . . . . .	17
2.1.2 Details of the $A$ -matrices . . . . .	19
2.1.3 Orthonormalization of effective basis states . . . . .	21
2.1.4 Hilbert space truncation . . . . .	22
2.1.5 Scalar product . . . . .	25
2.1.6 Reduced density matrix . . . . .	26
2.1.7 Operators in an effective basis . . . . .	27
2.1.8 Local operators acting on $ \psi\rangle$ . . . . .	29
2.1.9 Expectation values . . . . .	30

2.2	Variational optimization scheme . . . . .	30
2.2.1	Energy minimization of the current site . . . . .	31
2.2.2	Sweeping details . . . . .	32
2.2.3	Numerical costs . . . . .	35
<b>3</b>	<b>Matrix product state method for infinite systems</b>	<b>37</b>
3.1	Construction of infinite matrix product states . . . . .	37
3.2	Details of infinite matrix product states . . . . .	39
3.2.1	Expectation values . . . . .	39
3.2.2	Reduced density matrix . . . . .	42
3.3	Infinite time evolving block decimation . . . . .	42
3.3.1	Decomposition of the time evolution . . . . .	43
3.3.2	Local operators acting on $ \psi\rangle$ . . . . .	44
3.3.3	Determining the ground state . . . . .	44
<b>4</b>	<b>Correlations</b>	<b>47</b>
4.1	Correlation functions . . . . .	47
4.2	Correlation density matrix . . . . .	48
<b>5</b>	<b>Results</b>	<b>53</b>
5.1	Consistency check for the noninteracting case . . . . .	53
5.1.1	Infinite time evolving block decimation . . . . .	53
5.1.2	Variational matrix product state method . . . . .	54
5.2	Numerical checks on the DMRG results . . . . .	61
5.3	Investigation of correlation functions and expectation values . . . . .	66
5.4	Investigation of the correlation density matrix . . . . .	74
<b>6</b>	<b>Outlook</b>	<b>81</b>
<b>A</b>	<b>Further details</b>	<b>83</b>
A.1	Jordan-Wigner transformation . . . . .	83
A.1.1	Definition . . . . .	83
A.1.2	Commutator relations . . . . .	84
A.1.3	Application to a ladder model . . . . .	85
A.2	Derivation of the orthonormality condition . . . . .	86
A.3	Singular value decomposition . . . . .	87
A.4	Numerical costs of matrix multiplications and index contractions . . . . .	87

List of figures	96
List of tables	97
Bibliography	99
Acknowledgements	101



# Introduction

Important information on a physical model is given in terms of the phase diagram as a function of the model's parameters. To distinguish between different phases, one may look at several correlation functions and determines their behaviour at long distances. This procedure has the disadvantage however, that one has to guess in advance which correlation functions could be dominant and then has to prove or disprove that.

A promising candidate to overcome this weakness is the correlation density matrix [1]. If one has the ground state wave function for an interacting lattice model, one can easily obtain reduced density matrices for any clusters, i.e. connected bunches of sites. Given two separated clusters A and B, the correlation density matrix is defined as the reduced density matrix of their union minus the direct product of their respective reduced density matrices. To identify the operator(s) dominating the correlations, one decomposes the correlation density matrix by numerical singular value decomposition [1].

In this thesis correlations of the spinless extended Hubbard model with infinite nearest neighbour repulsion and correlated hopping on a two-leg ladder are studied [1]. This model is not solvable analytically exact for some limiting cases[2].

To solve this problem numerically for every parameter regime the density matrix renormalization group (DMRG) is applied [3]. In order to obtain comparable results via different techniques, this method is applied in two ways. One is the well-known variational matrix product state method applied on a chain with finite length [4, 5, 6], the other one is the recently suggested infinite time-evolving block decimation algorithm [7].

## Outline

This thesis is organized as follows. In chapter one, the spinless extended Hubbard model on a two-leg ladder is introduced. As the simplest limiting case the tight binding ladder is solved. The solutions of Siew-Ann Cheong and Christopher L. Henley to more interesting limiting cases are presented.

In chapter two, the matrix product state approach for finite chains with open boundary conditions is introduced and all necessary techniques for solving the model are presented (as calculating expectation values, scalar products, reduced density matrices, ...). Then it is shown, how to incorporate the DMRG Hilbert space truncation. Finally it is discussed, how one determines the ground state by variational optimization and an analysis of numerical costs is given.

In chapter three, the application of matrix product states in the context of infinite time-evolving block decimation is explained. Again, the necessary techniques are shown (which are quite different from the previous ones), how one uses DMRG truncation, and how the ground state is obtained.

In chapter four, correlations and especially details of the correlation density matrix are discussed.

In chapter five, our results are presented. As a first test ground, numerical results are compared with the tight binding ladder to obtain a first check on the accuracy of the calculations. Further, numerical calculations for all parameter regimes are presented, where some cases are compared with the exact results of Cheong and Henley.

# Chapter 1

## Model

The Hubbard model is an approximate model and the simplest one of interacting particles in a lattice. It consists of two terms in the Hamiltonian: a kinetic term, allowing for tunneling ('hopping') of particles between neighbouring sites of the lattice, and a potential term, consisting of an on-site interaction. However, as one is considering spinless fermions in this thesis, this model reduces to the tight binding model. For any new physics, one has to investigate the extended Hubbard model which includes interactions between particles of different sites.

### 1.1 Spinless extended Hubbard model

There are various possibilities for interactions in the extended Hubbard model. In this thesis an extra potential term - the nearest neighbour repulsion - and an extra kinetic term - the correlated hopping - are considered. For charged particles, nearest neighbour repulsion arises naturally from Coulomb interaction and is set to infinity in this thesis. For analytical approaches, this presents a great benefit as it reduces the dimension of the Hilbert space, but the numerical approach presented in this thesis does not benefit as much from this fact (see Sec. 2.2.3 for an explanation). So one has to work with an explicit nearest neighbour repulsion term in the Hamiltonian. One motivation for the correlated hopping is that it arises from second order perturbation theory when the nearest neighbour repulsion is finite. Whatever the justification of this term, it is a way to generate superconducting pairing. This particular model is chosen to (i) reproduce the results of [2] and (ii) to expand these results.

#### 1.1.1 Hamiltonian

The Hamiltonian of the spinless extended Hubbard model with infinite nearest neighbour repulsion on a two-leg ladder with fermionic creation and annihilation operators has the form

$$\begin{aligned}
H = & -t_{\parallel} \sum_{a=1}^2 \sum_i (c_{a,i}^{\dagger} c_{a,i+1} + c_{a,i+1}^{\dagger} c_{a,i}) \\
& -t_{\perp} \sum_i (c_{1,i}^{\dagger} c_{2,i} + c_{2,i}^{\dagger} c_{1,i}) \\
& -t_c \sum_i (c_{1,i-1}^{\dagger} n_{2,i} c_{1,i+1} + c_{1,i+1}^{\dagger} n_{2,i} c_{1,i-1} + c_{2,i-1}^{\dagger} n_{1,i} c_{2,i+1} + c_{2,i+1}^{\dagger} n_{1,i} c_{2,i-1}) \quad (1.1) \\
& +V \sum_{a=1}^2 \sum_i n_{a,i} n_{a,i+1} + V \sum_i n_{1,i} n_{2,i},
\end{aligned}$$

where the two legs of the ladder are labeled by  $a$  and the rungs of the ladder are labeled by  $i$  and  $n_{a,i} = c_{a,i}^{\dagger} c_{a,i}$ . In the following the  $a = 1$  leg is referred to as upper leg (denoted by  $\uparrow$ ) and the  $a = 2$  leg as lower leg (denoted by  $\downarrow$ ), see Fig. 1.1. The model is invariant under leg interchange. The length of the ladder is not yet specified. One shall do so later, since both finite and infinite ladders will be considered.

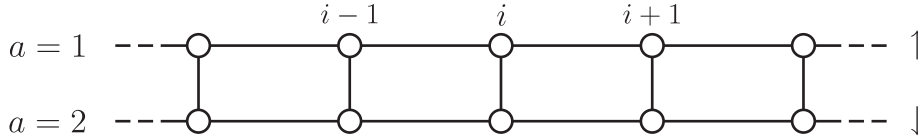


Figure 1.1: Ladder model

All parameters of the Hamiltonian are chosen as real numbers to obtain a problem which can be solved using purely real wave functions. The various terms are depicted schematically in Fig. 1.2. The amplitude of hopping between neighbouring sites along the legs and the rungs is denoted by  $t_{\parallel}$  and  $t_{\perp}$  respectively. The correlated hopping between next-neighbouring sites along the legs is denoted by  $t_c$  and needs the presence of a second particle on the other leg (see Fig. 1.2). Even though the nearest neighbour repulsion should be infinite in this model, it explicitly appears in the Hamiltonian as  $V$ . Due to numerical reasons (i.e. one cannot compute anything with terms being infinite), one has to choose  $V$  finite and thus the corresponding term in the Hamiltonian is well defined. For numerical calculations it is sufficient to set  $V$  to a number several orders of magnitude greater than all the other parameters.

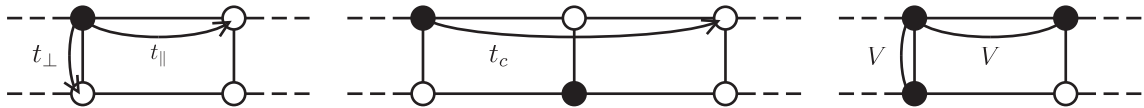


Figure 1.2: Hamiltonian terms (from left to right): rung hopping, leg hopping, correlated hopping and nearest neighbour repulsion. Black circles denote occupied sites and white circles unoccupied ones.

In this model, one hopping amplitude may be chosen to set the reference energy scale because the Hamiltonian does not adopt an energy scale due to another parameter (the finite value of

$V$  is a numerical artefact). In this thesis, the amplitude of hopping along legs normalizes the other hopping amplitudes, i.e.  $t_{\perp}$  and  $t_c$  are given in units of  $t_{\parallel} \equiv 1$ . Numerical calculations are done for  $t_{\perp}$  and  $t_c$  in the range from 0 to 100 and thus it turned out that it suffices to set  $V$  to  $10^4$ .

### 1.1.2 Mapping on 1D Hamiltonian

As the matrix product state method (DMRG) is most useful for one-dimensional systems, a one-dimensional model is considered. To achieve this, the two sites of a rung are mapped onto one effective site. The Hilbert space of this effective site is the direct product of the local Hilbert spaces of the site on the upper leg and the one on the lower leg:

$$\mathcal{H}_{\text{eff}} = \mathcal{H}_{\uparrow} \otimes \mathcal{H}_{\downarrow}. \quad (1.2)$$

Thus the resulting effective local basis is given by  $|\sigma\rangle = \{|0\rangle, |\downarrow\rangle, |\uparrow\rangle, |\uparrow\downarrow\rangle\}$ , with

$$\begin{aligned} |0\rangle \equiv |\text{None Occupied}\rangle &\equiv \begin{pmatrix} 1 \\ 0 \\ 0 \\ 0 \end{pmatrix}, & |\downarrow\rangle \equiv |\text{Lower Occupied}\rangle &\equiv \begin{pmatrix} 0 \\ 1 \\ 0 \\ 0 \end{pmatrix}, \\ |\uparrow\rangle \equiv |\text{Upper Occupied}\rangle &\equiv \begin{pmatrix} 0 \\ 0 \\ 1 \\ 0 \end{pmatrix}, & |\uparrow\downarrow\rangle \equiv |\text{Both Occupied}\rangle &\equiv \begin{pmatrix} 0 \\ 0 \\ 0 \\ 1 \end{pmatrix}. \end{aligned} \quad (1.3)$$

Operator representations in this Hilbert space have to be worked out via the direct product of corresponding operators. Given an operator  $U_i$  acting on the upper site of rung  $i$  and an operator  $L_i$  acting on the lower one, the corresponding operator in the four-dimensional Hilbert space reads as

$$(UL)_i \equiv U_i \otimes L_i, \quad (1.4)$$

for example  $c_{\uparrow i} \rightarrow (CE)_i \equiv c_{\uparrow i} \otimes \mathbb{1}$ ,  $c_{\downarrow i} \rightarrow (EC)_i \equiv \mathbb{1} \otimes c_{\downarrow i}$  and  $c_{\uparrow i}^{\dagger} c_{\downarrow i} \rightarrow (C^{\dagger}C)_i \equiv c_{\uparrow i}^{\dagger} \otimes c_{\downarrow i}$ .

Hamiltonians with fermionic creation and annihilation operators are best handled after performing the Jordan-Wigner transformation (see App. A.1). Combining the mapping onto a one-dimensional problem with the latter, the Hamiltonian reads as

$$\begin{aligned}
H = & -t_{\parallel} \sum_i \left( (C^\dagger Z)_i (CE)_{i+1} + (CZ)_i (C^\dagger E)_{i+1} + (EC^\dagger)_i (ZC)_{i+1} + (EC)_i (ZC^\dagger)_{i+1} \right) \\
& -t_{\perp} \sum_i \left( (C^\dagger C)_i + (CC^\dagger)_i \right) \\
& -t_c \sum_i \left( (C^\dagger Z)_{i-1} (-ZN)_i (CE)_{i+1} + (CZ)_{i-1} (-ZN)_i (C^\dagger E)_{i+1} \right. \\
& \quad \left. + (EC^\dagger)_{i-1} (-NZ)_i (ZC)_{i+1} + (EC)_{i-1} (-NZ)_i (ZC^\dagger)_{i+1} \right) \\
& +V \sum_i \left( (NE)_i (NE)_{i+1} (EN)_i (EN)_{i+1} \right) + V \sum_i (NN)_i, \tag{1.5}
\end{aligned}$$

## 1.2 Exact calculations without electron-electron interaction

There are two cases without electron-electron interaction (i.e.  $V = 0$  and  $t_c = 0$ ) which can be solved exactly very easily. The calculations are done for a finite Fermi energy  $\varepsilon_F$ , which is set to zero afterwards in order to compare the solutions with numerical results. The Fermi wavenumber is defined by  $E(k_F) = \varepsilon_F$ .

### 1.2.1 Tight binding chain

One has a single chain of sites, which are enumerated by an integer  $n$  (the limits of  $n$  do not matter for the moment), with a lattice constant of  $a$ . The position of a site is  $x = na$  (see Fig. 1.3). The whole problem is solved in second quantization where  $c_n^\dagger$  creates a particle at site  $n$ . So the Hamiltonian in the many-particle Hilbert space is

$$H = -t_{\parallel} \sum_n (c_n^\dagger c_{n+1} + c_{n+1}^\dagger c_n). \tag{1.6}$$

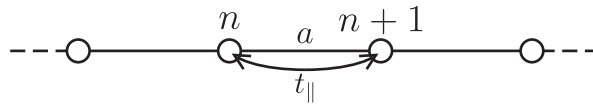


Figure 1.3: Tight binding chain

### Periodic boundary conditions

The total length of the chain is  $L = Na$ , where  $N$  is the total number of considered sites. Periodic boundary conditions require that site  $N + 1$  is identified with site 1.

The creation operators of the eigenstates of the Hamiltonian have the form

$$c_k^\dagger = \frac{1}{\sqrt{N}} \sum_{n=1}^N e^{-ikan} c_n^\dagger, \quad (1.7)$$

where  $\{c_k, c_{k'}^\dagger\} = \delta_{kk'}$ , with eigenvalues  $E(k) = -2t_{\parallel} \cos(ka)$  and allowed  $k$ -values given by  $k = \frac{2\pi m}{L}$  and  $m$  an integer. As the system is translation invariant under translations by  $a$ , it suffices to reduce  $k$  to the interval  $(-\frac{\pi}{a}; \frac{\pi}{a}]$ , so  $|m| \leq \frac{N}{2}$ . The many-particle ground state has all states occupied with energy less than  $\epsilon_F$ , thus the ground state energy per unit cell is given by

$$|\psi^G\rangle = \prod_{|k| \leq k_F} c_k^\dagger |0\rangle, \quad (1.8)$$

$$\langle E \rangle \equiv \frac{E_{\text{tot}}}{N} = \frac{1}{N} \sum_{|k| \leq k_F} E(k), \quad (1.9)$$

where zero is the totally empty state. To calculate the average occupancy  $\langle \hat{n}_n \rangle = \langle c_n^\dagger c_n \rangle$  at site  $n$  one needs the back transformation of Eq. (1.7)

$$\begin{aligned} \langle \hat{n}_n \rangle &= \langle 0 | \left( \prod_{|k'| \leq k_F} c_{k'} \right) \left( \frac{1}{\sqrt{N}} \sum_{k_1} e^{ik_1 an} c_{k_1}^\dagger \right) \left( \frac{1}{\sqrt{N}} \sum_{k_2} e^{-ik_2 an} c_{k_2} \right) \left( \prod_{|k| \leq k_F} c_k^\dagger \right) |0\rangle \\ &= \frac{1}{N} \sum_{k_1, k_2} e^{(ik_1 an - ik_2 an)} \langle 0 | \left( \prod_{|k'| \leq k_F} c_{k'} \right) c_{k_1}^\dagger c_{k_2} \left( \prod_{|k| \leq k_F} c_k^\dagger \right) |0\rangle \\ &\sim \delta_{k_1 k_2} \delta_{k_2 k} \text{ (because } \langle 0 | c_{k_1}^\dagger = 0 = c_{k_2} |0\rangle \text{)} \rightarrow |k_1| \leq k_F, |k_2| \leq k_F \\ &\Rightarrow \sim \delta_{k_1 k_2} \text{ (because } c_{k_1}^\dagger \left( \prod_{|k| \leq k_F} c_k^\dagger \right) = 0 \text{)} \\ &= \frac{1}{N} \sum_{|k| \leq k_F} 1 \equiv \frac{N_{\text{tot}}}{N}. \end{aligned} \quad (1.10)$$

This is site-independent and thus equal to the filling of the chain.

For other expectation values one may use these arguments, to obtain the correlation function  $G_{n+r, n} = \langle c_n^\dagger c_{n+r} \rangle$ , where  $r$  is an integer

$$\langle c_n^\dagger c_{n+r} \rangle = \frac{1}{N} \sum_{|k| \leq k_F} e^{-ikar}. \quad (1.11)$$

The two-particle Green's function  $G_{n+r,n+r+1;n,n+1} = \langle c_n^\dagger c_{n+1}^\dagger c_{n+r} c_{n+r+1} \rangle$  ( $r \geq 2$ ) may be obtained directly from the Green's function. In order to have a contribution, the same two particles that are destroyed by  $c_{n+r} c_{n+r+1}$  must be created by  $c_n^\dagger c_{n+1}^\dagger$ . There are two combinations:  $c_{n+1}^\dagger$  goes with  $c_{n+r}$  and  $c_n^\dagger$  goes with  $c_{n+r+1}$  or  $c_{n+1}^\dagger$  goes with  $c_{n+r+1}$  and  $c_n^\dagger$  goes with  $c_{n+r}$ . According to Eq. (1.11) one obtains

$$G_{n+r,n+r+1;n,n+1} = G_{n+r,n+1} G_{n+r+1,n} - G_{n+r+1,n+1} G_{n+r,n}, \quad (1.12)$$

where the minus sign is due to fermionic anticommutator relations.

As a last correlation function the density-density correlation  $\langle \hat{n}_n \hat{n}_{n+r} \rangle$  is evaluated (with its mean  $\langle \hat{n}_n \rangle \langle \hat{n}_{n+r} \rangle$  subtracted to obtain pure correlations)

$$\begin{aligned} \langle \hat{n}_n \hat{n}_{n+r} \rangle - \langle \hat{n}_n \rangle \langle \hat{n}_{n+r} \rangle &\stackrel{1.12}{=} \langle \hat{n}_n \rangle \langle \hat{n}_{n+r} \rangle - G_{n+r,n} G_{n,n+r} - \langle \hat{n}_n \rangle \langle \hat{n}_{n+r} \rangle \\ &= -|G_{n+r,n}|^2. \end{aligned} \quad (1.13)$$

## Infinite Chain

One can see the infinite chain as the limit  $N \rightarrow \infty$  of the chain with periodic boundary conditions. Thus the sum over discrete  $k$ -states has to be replaced by an integral  $\frac{1}{N} \sum_k \rightarrow a \int \frac{dk}{2\pi}$ . The ground state is similar to Eq. (1.8), with the sum in Eq. (1.9) replaced by the integral:

$$\langle E \rangle \equiv \lim_{N \rightarrow \infty} a \int_{-k_F}^{k_F} E(k) \frac{dk}{2\pi} = -\frac{2t_{\parallel}}{\pi} \sin(k_F a). \quad (1.14)$$

Similarly one obtains for the filling, one-particle correlator, two-particle correlator, and density-density correlation:

$$\frac{N_{tot}}{N} \stackrel{1.10}{=} \lim_{N \rightarrow \infty} a \int_{-k_F}^{k_F} \frac{dk}{2\pi} = \frac{k_F a}{\pi}, \quad (1.15)$$

$$G_{n+r,n} \stackrel{1.11}{=} \lim_{N \rightarrow \infty} a \int_{-k_F}^{k_F} e^{-ikar} \frac{dk}{2\pi} = \frac{ak_F \sin(ak_F r)}{\pi ak_F r}, \quad (1.16)$$

$$G_{n+r,n+r+1;n,n+1} \stackrel{1.12}{=} G_{n+r,n+1} G_{n+r+1,x} - G_{n+r+1,n+1} G_{n+r,x}, \quad (1.17)$$

$$\langle \hat{n}_n \hat{n}_{n+r} \rangle - \langle \hat{n}_n \rangle \langle \hat{n}_{n+r} \rangle \stackrel{1.13}{=} - \left( \frac{ak_F \sin(ak_F r)}{\pi ak_F r} \right)^2. \quad (1.18)$$

### Open boundary conditions

Open boundary conditions means that one has a chain of  $N$  sites with finite length  $L = (N - 1)a$  and to the left of site 1 and to the right of site  $N$  is vacuum, i.e. the state has to be strictly zero there. To solve this problem, one uses a trick: one adds a zeroth site to the left of the first site and a  $(N + 1)$ th site to the right of the  $N$ th site and changes the boundary conditions, such that  $\psi(x = 0) = 0 = \psi(x = (N + 1)a)$ . But this is in principle the setup of a chain with length  $L = (N + 1)a$ , periodic boundary conditions (zeroth site equals  $(N + 1)$ th site), and the additional boundary condition  $\psi(x = 0) = 0$ . See Fig. 1.4 for a pictorial explanation.

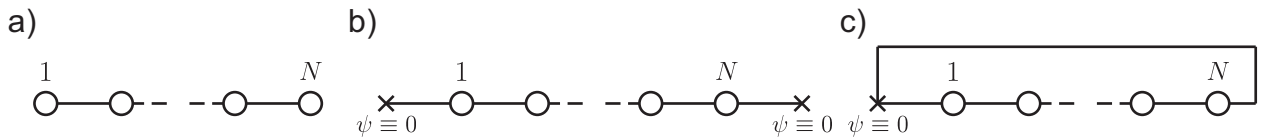


Figure 1.4: Transformation of open boundary conditions: a) Initial boundary conditions. b) Boundary conditions with additional sites at the ends. c) Final periodic boundary conditions.

The unconstrained energy eigenstates without the additional boundary condition have the form

$$c_{k'}^\dagger = \frac{1}{\sqrt{N+1}} \sum_n e^{-ik'an} c_n^\dagger. \quad (1.19)$$

But the additional boundary condition requires that  $c_{n=0} c_{k'}^\dagger = 0$ , which is obviously not fulfilled. The following linear combination fulfills the additional boundary condition

$$c_k^\dagger = \frac{1}{\sqrt{2i}} \left( c_{-k'}^\dagger - c_{k'}^\dagger \right) = \sqrt{\frac{2}{N+1}} \sum_n \sin(kan) c_n^\dagger, \quad (1.20)$$

with new restrictions on  $k$ :  $k = \frac{\pi}{(N+1)a}m$ ;  $1 \leq m < (N+1)$ . In fact, one has a particle in a box which is restricted to certain sites. This leads to a ground state as in Eq. (1.8) and a ground state energy as in Eq. (1.9) with an altered set of discrete  $k$ 's restricted to positive  $k$ 's by convention. This effectively doubles the density of states per  $k$  interval.

One readily obtains the following correlators:

$$\langle \hat{n}_n \rangle \stackrel{1.10}{=} \frac{2}{N+1} \sum_{k \leq k_F} \sin^2(kan), \quad (1.21)$$

$$\frac{N_{tot}}{N} = \frac{1}{N} \sum_{n=1}^N \langle \hat{n}_n \rangle = \frac{1}{N} \sum_{n=1}^N \frac{2}{N+1} \sum_{k \leq k_F} \sin^2(kan) = \frac{1}{N} \sum_{k \leq k_F}, \quad (1.22)$$

$$G_{n+r,n} \stackrel{1.11}{=} \frac{2}{N+1} \sum_{k \leq k_F} \sin(kan) \sin(ka(n+r)), \quad (1.23)$$

$$G_{n+r,n+r+1;n,n+1} \stackrel{1.12}{=} G_{n+r,n+1} G_{n+r+1,x} - G_{n+r+1,n+1} G_{n+r,x}, \quad (1.24)$$

$$\langle \hat{n}_n \hat{n}_{n+r} \rangle - \langle \hat{n}_n \rangle \langle \hat{n}_{n+r} \rangle \stackrel{1.13}{=} - |G_{n+r,n}|^2. \quad (1.25)$$

## Two parallel non-interacting chains

The case where the Hamiltonian Eq. (1.1) reduces to the Hamiltonian Eq. (1.6) - i.e.  $a \equiv 1$ ,  $\epsilon_F = 0$ ,  $t_\perp = 0$ ,  $t_C = 0$ ,  $V = 0$  - describes two parallel non-interacting chains. All results obtained in this section have to be multiplied by two in order to compare with a ladder with the same parameters.

### 1.2.2 Tight binding ladder

One has a ladder of sites with the legs enumerated by integer  $\alpha$  ( $\alpha = 1, 2$ ) and the rungs by  $n$  (the limits of  $n$  do not care for the moment). The lattice constant - both along legs and rungs - is  $a$ . The position of a rung is  $x = na$ . Again, the problem is solved in second quantization and  $c_{\alpha,n}^\dagger$  creates a particle on leg  $\alpha$  at rung  $n$ . So the Hamiltonian in the many-particle Hilbert space is given by

$$H = -t_{\parallel} \sum_{\alpha=1}^2 \sum_n (c_{\alpha,n}^{\dagger} c_{\alpha,n+1} + c_{\alpha,n+1}^{\dagger} c_{\alpha,n}) - t_{\perp} \sum_n (c_{1,n}^{\dagger} c_{2,n} + c_{2,n}^{\dagger} c_{1,n}). \quad (1.26)$$

This model can be solved easily by introducing symmetric and antisymmetric combinations of the sites of a rung

$$\left. \begin{aligned} c_{+,n}^{\dagger} &= \frac{1}{\sqrt{2}} (c_{1,n}^{\dagger} + c_{2,n}^{\dagger}) \\ c_{-,n}^{\dagger} &= \frac{1}{\sqrt{2}} (c_{1,n}^{\dagger} - c_{2,n}^{\dagger}) \end{aligned} \right\} c_{\mu,n}^{\dagger} = \frac{1}{\sqrt{2}} (c_{1,n}^{\dagger} + \mu c_{2,n}^{\dagger}) \quad (\mu = \pm 1). \quad (1.27)$$

In terms of these combinations, the Hamiltonian reads as

$$H = \sum_{\mu} \left( -t_{\parallel} \sum_n (c_{\mu,n}^{\dagger} c_{\mu,n+1} + c_{\mu,n+1}^{\dagger} c_{\mu,n}) - t_{\perp} \sum_n c_{\mu,n}^{\dagger} c_{\mu,n} \right). \quad (1.28)$$

But this represents two independent chains with a constant site energy (i.e. a shift of the Fermi energy effectively) that do not interact with each other. Similar to the previous section one makes the ansatz

$$c_{\mu,k}^{\dagger} = \frac{1}{\sqrt{N}} \sum_n e^{-ikan} c_{\mu,n}^{\dagger}, \quad (1.29)$$

where  $\{c_{\mu,k}, c_{\mu',k'}^{\dagger}\} = \delta_{\mu,\mu'} \delta_{kk'}$ , and obtains eigenenergies  $E_{\mu}(k) = -2t_{\parallel} \cos(ka) - \mu t_{\perp}$ . Effectively one has two chains of the same length as the ladder, one symmetric, the other antisymmetric under leg-interchange, with eigenenergies  $E_{\mu}(k)$ . This holds for all three boundary conditions, and so, according to the appropriate k-space discretization, one has a complete set of energy eigenstates for the ladder problem. As one has two chains, there are two Fermi wavenumbers  $k_{\text{F}}^{\mu}$ . So the ground state becomes

$$|\Psi^{\text{G}}\rangle = \prod_{\mu=\pm 1} \prod_{|k| \leq k_{\text{F}}^{\mu}} c_{\mu,k}^{\dagger} |0\rangle. \quad (1.30)$$

As all operators of the symmetric chain anticommute with all operators of the antisymmetric chain, expectation values are additive, e.g. the ground state energy

$$\langle E \rangle = \sum_{\mu} \langle E \rangle_{\mu}. \quad (1.31)$$

So all results from the previous paragraph may be applied here, one just has to replace  $\varepsilon_{\text{F}}$  by  $\varepsilon_{\text{F}} \mp t_{\perp}$ . An exception is the filling, which has to be divided by two, as the effective chains each consist of  $2N$  sites (instead of  $N$ ).

### 1.3 Exact calculations with electron-electron interaction

The spinless extended Hubbard model with infinite nearest neighbour repulsion and correlated hopping on a two-leg ladder has been studied intensely by S.W. Cheong and C. L. Henley [2]. Their results are included here for the sake of completeness and comparison with ours. They developed an analytical machinery of several mappings to solve this model in the three limiting cases of (i) infinitely-strong correlated hopping, (ii) zero inter-leg hopping and (iii) very strong inter-leg hopping. Assuming an adiabatic connection of all phases to at least one of these limiting cases, they guess a ground-state phase diagram (see Fig. 1.5). The lines, which separate the regimes of limiting behaviour, either in a quantum phase transition or a smooth crossover, are estimated to be along  $t_c = 2t_\perp$ ,  $t_\perp = 2$  and  $t_c = 2$  (as explained in Sec. 1.1.1,  $t_\perp$  and  $t_c$  are given in units of  $t_\parallel \equiv 1$ ).

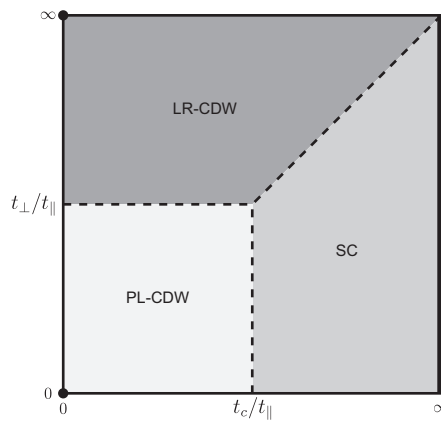


Figure 1.5: The zeroth-order ground-state phase diagram of the quarter-filled spinless extended Hubbard model with infinite nearest neighbour repulsion and correlated hopping on a two-leg ladder. The three limiting cases investigated by Cheong and Henley are depicted by the two dots and the thick solid line. Taken from [2].

#### Overview over the three limiting cases

The leading correlation exponents of various correlation functions decaying as a power law for the three limiting cases are summarized in Tab. 1.1. The correlation functions are classified into three classes:

1. Charge density wave (CDW) correlations, characterized by

$$C_{\text{CDW}}(i, r) = \langle N_i N_{i+r} \rangle - \langle N_i \rangle \langle N_{i+r} \rangle, \quad (1.32)$$

where  $N_i$  is some occupation number operator. There are CDW- $\pi$  correlations (charge density wave for the occupation number operator of bound pairs, see Sec. 1.3.1) and CDW $\pm$  correlations (charge density wave for the symmetric and antisymmetric occupation number operators  $n_{\pm, j} = (n_{1, j} \pm n_{2, j})$ , see Sec. 1.3.2).

2. Super conducting (SC) correlations, characterized by

$$C_{SC}(i, r) = \left\langle C_i^\dagger C_{i+1}^\dagger C_{i+r} C_{i+r+1} \right\rangle, \quad (1.33)$$

where  $C_i^\dagger$  is some creation operator. There are SC correlations of bound pairs (see Sec. 1.3.1) and  $SC\pm$  correlations (similar to CDW by creation operators  $c_{\pm,j}^\dagger = (c_{1,j}^\dagger \pm c_{2,j}^\dagger)$ , see Sec. 1.3.2).

3. Fermi liquid (FL) correlations, characterized by

$$C_{FL}(i, r) = \left\langle c_{a,i}^\dagger c_{a',i+r} \right\rangle, \quad (1.34)$$

with the creation and annihilation operators from Eq. (1.1).

Some correlation functions show oscillatory behaviour, with the corresponding wave vector  $k$  given in terms of  $k_F = \pi\bar{n}$ , where  $\bar{n}$  is the filling fraction of the ladder ( $0 \leq \bar{n} \leq \frac{1}{2}$ ).

### Nearest neighbour exclusion map and intervening-particle expansion

In Secs. 1.3.1 and 1.3.3 the extended Hubbard model is mapped onto a one-dimensional problem of hardcore bosons and spinless fermions, respectively. Afterwards, the nearest neighbour exclusion map is used to map these effective, nearest-neighbour-excluding particles onto nearest-neighbour-including particles, by removing one vacant site (there is at least one) between a pair of effective particles. This map implies that one effectively shortens the total length of the chain depending on the total number of particles. The filling fractions of the ladder model ( $\bar{n}_L$ ) and the one of the effective, mapped *chain* ( $\bar{n}_C$ ) are related by

$$\bar{n}_C = \frac{\bar{n}_L}{\frac{1}{2} - \bar{n}_L}. \quad (1.35)$$

In particular the expectation value  $\langle O_i O_{i+r} \rangle$  of two observables  $O_i$  and  $O_{i+r}$ , acting on sites separated by  $r$ , must be computed as the sum over expectation values with varying separations. This task is accomplished by the intervening-particle expansion, introduced by Cheong and Henley.

limit	correlation function	correlation exponent	wave vector	
(i) $t_c \gg t, t_\perp$	CDW- $\pi$	$\frac{1}{2} + \frac{5}{2} \left( \frac{1}{2} - \bar{n} \right)$	$2k_F$	
		2	0	
	SC	$\frac{1}{2}$	0	
(ii) $t \gg t_\perp, t_c = 0$	CDW+	$\frac{3}{2} \rightarrow \frac{1}{2}$	$2k_F$	
		2	0	
	CDW-	$\frac{1}{2}$	$2k_F$	
		2	0	
	SC+	2	0	
		2	$2k_F$	
	SC-	$\frac{5}{2}$	$2k_F$	
		4	0	
	(iii) $t_\perp \gg t, t_c = 0$	FL	$\frac{1}{4}$	$k_F$
			1	$k_F$
CDW		$\frac{1}{2}$	$2k_F$	
		2	0	
		2	$2k_F$	
SC		$\frac{1}{8}$	0	
		$\frac{1}{4}$	$2k_F$	
	2	0		
	2	$2k_F$		

Table 1.1: Leading correlation exponents of the correlation functions that decay as power laws. Most of them are universal, but some depend on the filling fraction. Taken from [2].

### 1.3.1 Infinitely-strong correlated hops

In this limiting case, correlated hopping dominates over the other two hopping terms and thus pairs of fermions, which are effectively bosons, show up. These extended hardcore bosons - they exclude on-site and nearest-neighbour occupation - can be divided into an even and an odd flavour (see Fig. 1.6) and the corresponding bosonic operators are given by

$$B_{j,+}^\dagger = \begin{cases} c_{1,j}^\dagger c_{2,j+1}^\dagger & j \text{ odd} \\ c_{1,j+1}^\dagger c_{2,j}^\dagger & j \text{ even} \end{cases} \quad B_{j,-}^\dagger = \begin{cases} c_{1,j+1}^\dagger c_{2,j}^\dagger & j \text{ odd} \\ c_{1,j}^\dagger c_{2,j+1}^\dagger & j \text{ even} \end{cases}, \quad (1.36)$$

where + corresponds to even flavour and - to odd flavour.

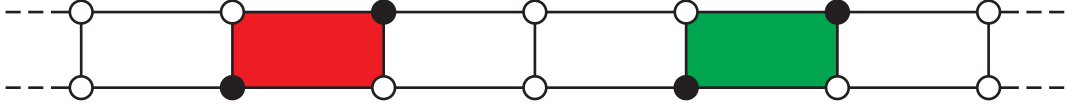


Figure 1.6: Effective extended hardcore bosons with even (red) and odd (green) flavour. It is not possible for an extended hardcore boson to change its flavour by correlated hopping. Taken from [2].

These extended hardcore bosons are mapped onto hardcore bosons by the nearest neighbour exclusion map. This is the most complicated mapping. Finally, the hardcore bosons are mapped onto non-interacting spinless fermions. This is a well-known map and the resulting ground state is the absolute value of the Fermi sea ground state.

### 1.3.2 Zero inter-leg hopping

The zero inter-leg hopping case involves not only  $t_{\perp} = 0$ , but also  $t_c = 0$ , i.e. one has two chains with respect to hopping. Thus  $P_i$  - the number of fermions on leg  $i$  - is a good quantum number. Nevertheless, the chains are not independent due to nearest neighbour repulsion which manifests in the fact that fermions cannot move past each other no matter whether they are on the same leg or not. It turns out that the state with lowest energy is the *staggered ground state*, i.e. that fermions on the upper leg and the lower leg alternate (see Fig. 1.7). The ground state is twofold degenerate, because leg interchange of such a state yields a new state with the same energy, hence one can form the symmetric and antisymmetric linear combination of these two states to obtain eigenstates of the leg-interchange operator. Henley and Cheong map these staggered ground states onto non-interacting spinless fermions on a chain and express it via the Fermi sea ground state wave function. The filling fraction of this chain is twice the filling fraction of the ladder  $\bar{n}_C = 2\bar{n}_L$ .

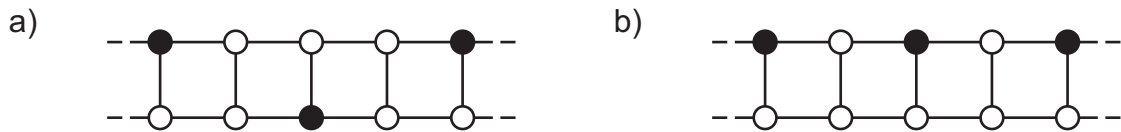


Figure 1.7: Possible configurations of fermions in the zero inter-leg hopping case: a) the staggered ground state with fermions on alternating legs b) another state with the same number of fermions, but all on the same leg. The fermions have less degrees of freedom and thus the state is of higher energy. Taken from [2].

### 1.3.3 Very strong inter-leg hopping

This is the opposite limiting case to Sec. 1.3.1, i.e. rung hopping dominates over the other hopping terms. Obviously, the fermions are very nearly in the rung ground state,

$$C_j^{\dagger} |0\rangle \equiv \frac{1}{\sqrt{2}} (c_{1,j}^{\dagger} + c_{2,j}^{\dagger}) |0\rangle, \quad (1.37)$$

only disturbed by the small leg hopping. A fermion in the state given by Eq. (1.37) is called a *rung fermion*. Thus it is possible to map the ladder problem onto a one-dimensional problem of spinless rung-fermions with infinite nearest neighbour repulsion. Similar to Sec. 1.3.1, this problem is mapped via the nearest neighbour exclusion map onto a chain of spinless fermions which is solved by the Fermi sea ground state.

## Chapter 2

# Matrix product state method for finite systems

In this chapter, the matrix product state method for a finite system with open boundary conditions is introduced. It was developed to deal with the problem of very large Hilbert space dimensions in quantum chain models. The full Hilbert space of such a model consists of the direct product of all the local Hilbert spaces and thus its size increases exponentially with the number of sites, i.e. with the system size. The basic idea of matrix product states is to write single states such as the ground state in a compact and manageable way by introducing new - effective - Hilbert spaces. The matrix product state method in this chapter is based on a matlab program originally written by F. Verstraete [4].

As one is dealing with fermions it is convenient to apply the Jordan-Wigner transformation (see App. A.1). After this transformation one may interchange different basis states without obtaining a minus sign. So the order of basis states becomes irrelevant.

## 2.1 Matrix product states

### 2.1.1 Construction of matrix product states

If one considers a chain with open boundary conditions consisting of  $N$  equal sites with a local Hilbert space dimension of  $d$ , a state  $|\psi\rangle$  is described by

$$|\psi\rangle = \sum_{\sigma_1, \dots, \sigma_N} \psi_{\sigma_1, \dots, \sigma_N} |\sigma_1\rangle \dots |\sigma_N\rangle , \quad (2.1)$$

where  $\sigma_i = 1, \dots, d$  labels the local basis states of site  $i$ . In general, the size of the coefficient space  $\psi$  scales with  $\mathcal{O}(d^N)$ . This can be rewritten in a matrix decomposition

$$|\psi\rangle = \sum_{\sigma_1, \dots, \sigma_N} tr (A^{[\sigma_1]} \dots A^{[\sigma_N]}) |\sigma_1\rangle \dots |\sigma_N\rangle , \quad (2.2)$$

with a set of  $N$  times  $d$  matrices  $A^{[\sigma_k]}$ .<sup>1</sup> If these  $A$ -matrices are sufficiently large this decomposition is formally exact; by choosing them smaller, it also opens the opportunity to decrease resources drastically in a very intuitive way and still have a very good approximation of the state  $|\psi\rangle$ . If one selects a certain site  $i$ , the state can be rewritten as

$$|\psi\rangle = \sum_{l_k, r_k, \sigma_k} A_{l_k r_k}^{\sigma_k} |l_k\rangle |\sigma_k\rangle |r_k\rangle \sum_{l_k, r_k, \sigma_k} A_{l_k r_k}^{\sigma_k} |l_k\rangle |\sigma_k\rangle |r_k\rangle . \quad (2.3)$$

The effective 'left' basis  $|l_k\rangle = \sum_{\sigma_1, \dots, \sigma_{k-1}} A^{[\sigma_1]} \dots A^{[\sigma_{k-1}]} |\sigma_1\rangle \dots |\sigma_{k-1}\rangle$  consists of all sites  $j = 1, \dots, k-1$ , the effective 'right' basis  $|r_k\rangle$  is defined similarly by the sites  $j = k+1, \dots, N$ .<sup>2</sup> Site  $k$  is called the *current* site, as the state is expressed in the  $A$ -matrix of this site (see Fig. 2.1).

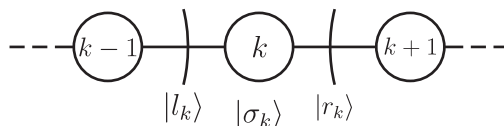


Figure 2.1: Current site with effective basis sets.

So far Eq. (2.1) and Eq. (2.3) are equivalent, but now one has a representation of the state where one can easily truncate the Hilbert space, namely the effective Hilbert spaces  $\mathcal{H}^{l_k}$  and  $\mathcal{H}^{r_k}$ . If one introduces a parameter  $D$  and truncates all effective Hilbert spaces of all sites to the dimension  $D$ , each  $A^{[\sigma_k]}$ -matrix has at most the dimension  $D \times D$ . Of course, Hilbert spaces with dimension less than  $D$  are not altered. So one has reduced the resources, needed to describe a state from  $\mathcal{O}(d^N)$  to  $\mathcal{O}(ND^2d)$  which is linear in the system size, assuming the size for  $D$  to accurately describe the state grows significantly slower than linearly in  $N$ . This is in fact the case for ground state calculations [4]! The way in which the Hilbert spaces are truncated and an estimate to the occurring error is given in Sec. 2.1.4.

Matrix product states can be seen in two alternative ways: a global view and a local view. The two perceptions are equivalent and both have their applications. In the global view the state is expressed as in Eq. (2.2), i.e. the effective Hilbert spaces have been used 'only' to reduce resources. The state is stored in the  $A$ -matrices, but the effective basis sets will be contracted out. One has to work very careful in this perception, because contracting out the effective basis sets leads to higher costs in resources! In the local view the state is expressed as in Eq. (2.3). It is called local because there is one special site, the *current* site, and all other sites are combined in effective orthonormalized basis sets. Usually, the local view is used iteratively for every site. In this perception, one needs effective descriptions of operators contributing to the Hamiltonian acting on other sites than the current site (see Sec. 2.1.7).

<sup>1</sup>For details of the  $A$ -matrices see Sec. 2.1.2.

<sup>2</sup>The trace in Eq. (2.2) vanished in Eq. (2.3) due to the finite length of the chain (see Sec. 2.1.2).

### 2.1.2 Details of the $A$ -matrices

Regardless of the truncation scheme one can consider some details of the  $A$ -matrices. First of all, one has to notice that by construction  $\dim(\mathcal{H}^{r_{k-1}}) \equiv \dim(\mathcal{H}^{l_k})$ , otherwise the matrix products in Eq. (2.2) would be ill-defined. Based on this, one finds another interpretation of the  $A$ -matrices in the local view. Let  $|l_k\rangle$  be the effective basis for the part left of site  $k$  (where  $k$  is far from the ends of the chain for simplicity). One has to keep in mind that this basis is build of truncated  $A$ -matrices:

$$\begin{aligned}
|l_k\rangle &= \sum_{\sigma_1, \dots, \sigma_{k-1}} (A^{[\sigma_1]} \dots A^{[\sigma_{k-1}]})_{\mathbb{1}l_k} |\sigma_1\rangle \dots |\sigma_{k-1}\rangle \\
&= \sum_{\sigma_{k-1}} \sum_{l_{k-1}} \underbrace{\sum_{\sigma_1, \dots, \sigma_{k-2}} (A^{[\sigma_1]} \dots A^{[\sigma_{k-2}]})_{\mathbb{1}l_{k-1}} |\sigma_1\rangle \dots |\sigma_{k-2}\rangle}_{|l_{k-1}\rangle} A_{l_{k-1}, l_k}^{[\sigma_{k-1}]} |\sigma_{k-1}\rangle \\
&= \sum_{\sigma_{k-1}, l_{k-1}} A_{l_{k-1}, l_k}^{[\sigma_{k-1}]} |l_{k-1}\rangle |\sigma_{k-1}\rangle . \tag{2.4}
\end{aligned}$$

So the  $A^{[\sigma_{k-1}]}$ -matrix maps the effective left basis  $|l_{k-1}\rangle$  together with the local  $|\sigma_{k-1}\rangle$  basis onto the effective left basis  $|l_k\rangle$ ! The same argument applied on the effective right basis of site  $k$  leads to the transformation of  $|r_{k+1}\rangle$  and  $|\sigma_{k+1}\rangle$  onto  $|r_k\rangle$  via the  $A^{[\sigma_{k+1}]}$ -matrix (see Eq. (2.5)).

$$|r_k\rangle = \sum_{\sigma_{k+1}, r_{k+1}} A_{r_k r_{k+1}}^{[\sigma_{k+1}]} |\sigma_{k+1}\rangle |r_{k+1}\rangle . \tag{2.5}$$

So far, this may be any transformation, but one may impose unitarity on the transformation (see below).

A special case are the  $A$ -matrices towards the ends of the chain. There is the vacuum state, left of site one and right of site  $N$  due to open boundary conditions. That means that  $\dim(\mathcal{H}^{l_1}) = 1 = \dim(\mathcal{H}^{r_N})$  and thus the trace may be dropped in Eq. (2.3). Thus, departing from the ends of the chain, the effective Hilbert spaces acquire dimension  $d^1, d^2, \dots$  until they become larger than  $D$  and need to be truncated. Correspondingly, the dimension of matrix  $A^{[\sigma_k]}$  is  $D_{k-1} \times D_k$ , where  $D_k = \min(d^k, d^{N-k}, D)$ . There is no truncation needed if  $\dim(\mathcal{H}^{l_k}) * d = \dim(\mathcal{H}^{r_k})$  or  $\dim(\mathcal{H}^{r_k}) * d = \dim(\mathcal{H}^{l_k})$ , so one may simply choose  $A_{(l_k \sigma_k) r_k} = \mathbb{1}$  and  $A_{l_k (r_k \sigma_k)} = \mathbb{1}$ , respectively.

Summarizing, the  $A$ -matrices have two functions. If site  $i$  is the current site in Eq. (2.3), the  $A^{[\sigma]}$ -matrices represent the state, i.e. its coefficients specify the linear combination of basis states  $|l_k\rangle$ ,  $|\sigma_k\rangle$  and  $|r_k\rangle$ . On the other hand, if not the current site, the  $A$ -matrices are used as a mapping to build the effective orthonormal basis for the current site.

#### Orthonormal basis sets

In the local view, the whole system is described by the  $A$ -matrices of the current site  $k$  in the effective left basis, the effective right basis, and the local basis of site  $k$ . A priori, the basis

states form an orthonormal set only for the local basis set. As mentioned in the previous section, one may ask for the effective basis sets  $|l\rangle$  and  $|r\rangle$ <sup>3</sup> to be orthonormal, too, i.e. require them to obey:

$$\begin{aligned}\langle l'|l\rangle &= \delta_{l'l}, \\ \langle r'|r\rangle &= \delta_{r'r}.\end{aligned}\tag{2.6}$$

This immediately implies the condition on the  $A^{[\sigma_j]}$ -matrices, using Eqs. (2.4) and (2.5) (see App. A.2):

$$\begin{aligned}\sum_{\sigma_j} (A^{[\sigma_j]})^\dagger A^{[\sigma_j]} &= \mathbb{1} \text{ for } j < k, \\ \sum_{\sigma_j} A^{[\sigma_j]} (A^{[\sigma_j]})^\dagger &= \mathbb{1} \text{ for } j > k.\end{aligned}\tag{2.7}$$

This orthonormality (i.e.  $\langle l'|l\rangle = \mathbb{1}$  and  $\langle r'|r\rangle = \mathbb{1}$ ) holds only for the current site. For the other sites there is always only one orthonormal effective basis.

## Graphical representation

Matrix product states can be depicted a convenient graphical representation (see Fig. 2.2). In this representation,  $A$ -matrices are displayed as boxes and  $A^{[\sigma_k]}$  is replaced by  $A_k$  for brevity. Indices correspond to links from the boxes. The left link connects to the effective left basis, the right link to the right one, and the link at the bottom to the local basis. Sometimes indices are explicitly written on the links to emphasize the structure of the sketch. Connected links denote a summation over the indices (also called contraction) of the corresponding  $A^{[\sigma]}$ -matrices. At the boundaries of the chain, a cross is used to indicate the vacuum state.

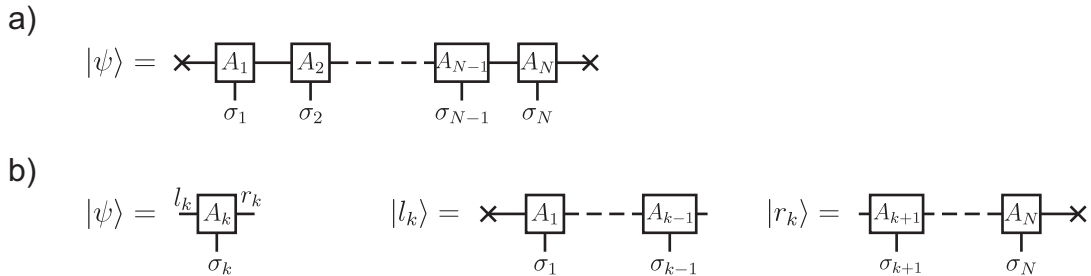


Figure 2.2: Graphical representation of a matrix product state in the a) global view and b) local view.

<sup>3</sup>From now on the index  $k$  is only displayed when several sites are involved. For the current site or in the case when only one  $A$ -matrix is considered the index will be dropped.

### 2.1.3 Orthonormalization of effective basis states

It is convenient to describe a state in the local view with orthonormal effective basis sets. It should be emphasized that this really just rewrites the state using the freedom that one always can insert any  $X^{-1}X = \mathbb{1}$  at any position in the matrix product state without altering it.

Assume site  $k$  to be the current site. Following the proof in App. A.2, one needs a procedure to ensure that site  $k + 1$  has an orthonormal effective left basis if site  $k$  has such a basis. A similar construction can be used to ensure that site  $k - 1$  has an orthonormal right basis, if  $k$  has such a basis. To this purpose one uses the singular value decomposition (SVD, see App. A.3). As the latter only works for matrices, one rewrites  $A_{l_k r_k}^{[\sigma_k]}$  by *fusing* the indices  $l_k$  and  $\sigma_k$ :

$$A_{l_k r_k}^{[\sigma_k]} \hat{=} A_{(l_k \sigma_k), r_k} = \sum_{m, n} u_{(l_k \sigma_k), m} s_{mn} (v^\dagger)_{nr_k} \hat{=} \sum_m u_{l_k m}^{[\sigma_k]} (sv^\dagger)_{mr_k}, \quad (2.8)$$

where  $m$ ,  $n$  and  $r_k$  have the same index range. Specifically,  $u$  fulfills

$$\mathbb{1} = u^\dagger u = \sum_{(l_k \sigma_k)} u_{(l_k \sigma_k), m}^* u_{(l_k \sigma_k), m}, \quad (2.9)$$

which is equivalent to the orthonormality condition Eq. (2.7) for the  $A^{[\sigma_k]}$ -matrices (see Fig. 2.3)!

Figure 2.3: Singular value decomposition of the  $A$ -matrices

As  $u$  replaces  $A^{[\sigma_k]}$  and  $sv^\dagger$  is contracted onto  $A^{[\sigma_{k+1}]}$ , this leaves the overall state unchanged (for a graphical depiction see Fig. 2.4):

$$\begin{aligned} A^{[\sigma_k]} A^{[\sigma_{k+1}]} &= \sum_{(r_k=l_{k+1})} A_{l_k r_k}^{[\sigma_k]} A_{l_{k+1} r_{k+1}}^{[\sigma_{k+1}]} = \sum_{(r_k=l_{k+1})} \sum_m u_{l_k m}^{[\sigma_k]} (sv^\dagger)_{mr_k} A_{l_{k+1} r_{k+1}}^{[\sigma_{k+1}]} \\ &= \sum_m u_{l_k m}^{[\sigma_k]} (sv^\dagger A_{k+1})_{mr_{k+1}}^{[\sigma_{k+1}]} \\ &= u^{[\sigma_k]} (sv^\dagger A_{k+1})^{[\sigma_{k+1}]} \hat{=} \tilde{A}^{[\sigma_k]} \tilde{A}^{[\sigma_{k+1}]} . \end{aligned} \quad (2.10)$$

Figure 2.4: Rearrangement of the  $A$ -matrices to switch the current site from site  $k$  to  $k + 1$ .

Site  $k + 1$  now has an orthonormal effective left basis. A similar procedure works for the effective right basis, see Fig. 2.5.

$$\begin{array}{c}
 l_{k-1} \quad \boxed{A_{k-1}} \quad \text{---} \quad \boxed{A_k} \quad r_k \\
 \quad \quad \quad \downarrow \quad \quad \quad \downarrow \\
 \quad \quad \quad \sigma_{k-1} \quad \quad \quad \sigma_k
 \end{array}
 =
 \begin{array}{c}
 l_{k-1} \quad \boxed{A_{k-1}us} \quad \text{---} \quad \boxed{v^\dagger} \quad r_k \\
 \quad \quad \quad \downarrow \quad \quad \quad \downarrow \\
 \quad \quad \quad \sigma_{k-1} \quad \quad \quad \sigma_k
 \end{array}$$

Figure 2.5: Orthonormal effective right basis for site  $k - 1$

To obtain an orthonormal effective left basis for the current site  $k$ , one starts with the first site, updates  $A^{[\sigma_1]}$  and  $A^{[\sigma_2]}$ , moves to the next site, updates  $A^{[\sigma_2]}$  and  $A^{[\sigma_3]}$ , and so on until site  $k - 1$ . For an orthonormal effective right basis, one starts with site  $N$ , updates  $A^{[\sigma_N]}$  and  $A^{[\sigma_{N-1}]}$ , and so on until site  $k + 1$  in a similar fashion.

If one has a description of the state  $|\psi\rangle$  in terms of orthonormal basis sets  $|l_k\rangle$ ,  $|\sigma_k\rangle$ ,  $|r_k\rangle$  for site  $k$ , it is now very easy to change the current site to site  $k \pm 1$ , with corresponding new orthonormal basis sets  $|l_{k\pm 1}\rangle$ ,  $|\sigma_{k\pm 1}\rangle$ ,  $|r_{k\pm 1}\rangle$ . Suppose one wants to change the current site with orthonormal basis sets from site  $k$  to site  $k + 1$ . Following the procedure described above, site  $k + 1$  already has an orthonormal right basis and all sites left of site  $k$  fulfill the orthonormality condition. All that is left to do, is to update site  $k$  and  $k + 1$  to obtain an orthonormal left basis for site  $k + 1$ . This is called a *switch* of the current site from site  $k$  to  $k + 1$ . The switch from site  $k$  to site  $k - 1$  is done analogous.

### 2.1.4 Hilbert space truncation

The Hilbert space truncation scheme applied is in complete analogy to DMRG [6]. The DMRG truncation scheme is based on discarding that part of the Hilbert space, on which a certain density matrix has sufficiently small weight. There are two ways to obtain an appropriate reduced density matrix. Two-site DMRG [3] and one-site DMRG [3]. In this thesis only one-site DMRG truncation is used.

#### Two-site DMRG

In two-site DMRG one has two current sites, say  $k$  and  $k + 1$ , and the cutoff dimension may be chosen site-dependent  $D \rightarrow D_k \equiv \dim(\mathcal{H}^{l_k})$ . Following the previous section, one may assume site  $k$  having an orthonormal left basis and site  $k + 1$  having an orthonormal right basis. After contracting the indices connecting  $A^{[\sigma_k]}$  and  $A^{[\sigma_{k+1}]}$  (see Fig. 2.6), the state is described by  $A_{l_k r_{k+1}}^{[\sigma_k, \sigma_{k+1}]}$ . In this description one determines the ground state (in whichever way one finds convenient). Afterwards, one needs to decompose  $A_{l_k r_{k+1}}^{[\sigma_k, \sigma_{k+1}]}$  into  $A^{[\sigma_k]}$  and  $A^{[\sigma_{k+1}]}$  again. This can be accomplished via singular value decomposition (see App. A.3) by fusing the indices  $l_k, \sigma_k \rightarrow (l_k \sigma_k)$  and  $r_{k+1}, \sigma_{k+1} \rightarrow (r_{k+1} \sigma_{k+1})$  (see Fig. 2.6). One obtains  $A_{l_k r_{k+1}}^{[\sigma_k, \sigma_{k+1}]} = \sum_i u_{l_k i}^{[\sigma_k]} s_i (v^\dagger)_{i r_{k+1}}^{[\sigma_{k+1}]}$ , where  $i = 1 \dots \min(dD_k, dD_{k+1})$ . The state is written as

$$\begin{aligned}
|\psi\rangle &= \sum_{l_k r_{k+1} \sigma_k \sigma_{k+1}} \left( \sum_i u_{l_k i}^{[\sigma_k]} s_i (v^\dagger)_{i r_{k+1}}^{[\sigma_{k+1}]} \right) |l_k\rangle |\sigma_k\rangle |\sigma_{k+1}\rangle |r_{k+1}\rangle \\
&= \sum_i s_i \underbrace{\left( \sum_{l_k \sigma_k} u_{l_k i}^{[\sigma_k]} |l_k\rangle |\sigma_k\rangle \right)}_{|\tilde{l}_i\rangle} \underbrace{\left( \sum_{r_{k+1} \sigma_{k+1}} (v^\dagger)_{i r_{k+1}}^{[\sigma_{k+1}]} |\sigma_{k+1}\rangle |r_{k+1}\rangle \right)}_{|\tilde{r}_i\rangle} \\
&= \sum_i s_i |\tilde{l}_i\rangle |\tilde{r}_i\rangle, \tag{2.11}
\end{aligned}$$

where the new set of basis states  $|\tilde{l}_i\rangle$  and  $|\tilde{r}_i\rangle$  is orthonormal with  $\langle \tilde{l}_{i'} | \tilde{l}_i \rangle = \delta_{i'i}$  and  $\langle \tilde{r}_{i'} | \tilde{r}_i \rangle = \delta_{i'i}$ , due to the column unitarity of  $u$  and the row unitarity of  $v^\dagger$ . This representation of the state may be seen as residing on the bond between  $k$  and  $k+1$ , with effective orthonormal basis sets for the parts of the system to the left and right of the bond. Reduced density matrices for these parts of the system, obtained by tracing out the respective complementary part, look like

$$\rho^{[L]} = \sum_i s_i^2 |\tilde{l}_i\rangle \langle \tilde{l}_i|, \quad \rho^{[R]} = \sum_i s_i^2 |\tilde{r}_i\rangle \langle \tilde{r}_i|. \tag{2.12}$$

Here one has an expression where the DMRG truncation scheme applies. One could keep all singular values greater than a certain cutoff, thereby specifying a value for  $D_{k+1}$  between 1 and  $\min(dD_k, dD_{k+2})$ , or – if one chooses  $D_k = D$  to be site-independent for simplicity – one could obtain a measure for the lost information. The 'lost' information (entropy), using the von Neumann entropy  $S = -Tr(\rho \ln \rho)$ , is given by

$$\varepsilon \equiv - \sum_{i>D} s_i^2 \ln(s_i^2), \tag{2.13}$$

where  $\sum s_i^2 = 1$  due to normalization of  $|\psi\rangle$ .



Figure 2.6: Procedure for site update within two-site DMRG. The grey line under the  $s$  indicates that  $s$  is the diagonal matrix of singular values.

### One-site DMRG

In contrast to the two-site DMRG, one-site DMRG does not allow for dynamical truncation during the calculation. The truncation is fixed by the initial choice of  $D$ . But it is possible to

determine an estimate on the error of this truncation by still analyzing the reduced density matrix. Starting from an expression for the full density matrix in the local view (current site  $k$  with orthonormal effective basis sets)

$$\begin{aligned}\rho = |\psi\rangle\langle\psi| &= \left( \sum_{lr\sigma} A_{lr}^\sigma |l\rangle|\sigma\rangle|r\rangle \right) \left( \sum_{l'r'\sigma'} (A_{l'r'}^{\sigma'})^* \langle l'|\langle\sigma'|\langle r'| \right) \\ &= \sum_{lr\sigma l'r'\sigma'} A_{lr}^\sigma (A_{l'r'}^{\sigma'})^* |l\rangle\langle l'|\sigma\rangle\langle\sigma'|r\rangle\langle r'|, \end{aligned} \quad (2.14)$$

one traces over the effective right basis and obtains a reduced density matrix for the current site and the left part of the system

$$\rho^{[l_{k+1}]} = \sum_{lr\sigma l'\sigma'} A_{lr}^\sigma (A_{l'r'}^{\sigma'})^* |l\rangle\langle l'|\sigma\rangle\langle\sigma'|. \quad (2.15)$$

This reduced density matrix is labeled with  $l_{k+1}$  because that's exactly what  $|l_{k+1}\rangle\langle l_{k+1}|$  describes. So if one switches the current site from site  $k$  to site  $k+1$ , one can check on the error of the truncation of  $\mathcal{H}^{l_{k+1}}$ . Fusing the indices  $l$  and  $\sigma$ , one obtains

$$\begin{aligned}\rho^{[l_{k+1}]} &= \sum_{lr\sigma l'\sigma'} A_{(l\sigma)r} A_{(l'\sigma')r}^* |(l\sigma)\rangle\langle(l'\sigma')| = \sum_{lr\sigma l'\sigma'} A_{(l\sigma)r} A_{r(l'\sigma')}^\dagger |(l\sigma)\rangle\langle(l'\sigma')| \\ &= \sum_{l\sigma l'\sigma'} (AA^\dagger)_{(l\sigma)(l'\sigma')} |(l\sigma)\rangle\langle(l'\sigma')|. \end{aligned} \quad (2.16)$$

One could diagonalize the coefficient matrix  $(AA^\dagger)_{(l\sigma)(l'\sigma')}$  to determine the largest weights of the density matrix, but there is a better way [3, 8]. Just as for the creation of orthonormal basis sets (see Sec. 2.1.3), one applies a singular value decomposition on the matrix  $A = usv^\dagger$  (this is not the usual  $A$ -matrix, but the rearranged form). Then the reduced density matrix reads as

$$\rho^{[l_{k+1}]} \equiv AA^\dagger = usv^\dagger vsu^\dagger = us^2u^\dagger, \quad (2.17)$$

and this is the diagonalization of  $\rho^{[l_{k+1}]}$ . So the weights of the density matrix are equal  $s^2$ ! Of course this works also for the right effective basis. With such an expression, one may check whether the effective Hilbert space dimension  $D$  of  $\mathcal{H}^{l_{k+1}}$  is too small or not. For example, one could ask for the smallest singular value  $s_D$  to be at least  $n$  orders of magnitude smaller than the greatest one  $s_1$ , i.e. the respective weights in the density matrix would be  $2n$  orders of magnitude apart. If the singular values do not decrease that strong, one has to choose a greater  $D$ .

### 2.1.5 Scalar product

The scalar product of two states  $|\psi\rangle$  and  $|\psi'\rangle$  is one of the simplest operations one can perform with matrix product states. It is calculated in the global view because then one does not need to care about orthonormalization of the  $A$ -matrices.

$$\begin{aligned} \langle\psi'|\psi\rangle &= \langle\sigma'_1|\dots\langle\sigma'_N| \left( \sum_{\sigma'_1,\dots,\sigma'_N} (A'^{[\sigma'_1]} \dots A'^{[\sigma'_N]})^* \right) \left( \sum_{\sigma_1,\dots,\sigma_N} (A^{[\sigma_1]} \dots A^{[\sigma_N]}) \right) |\sigma_1\rangle \dots |\sigma_N\rangle \\ &= \sum_{\sigma_1,\dots,\sigma_N} (A'^{[\sigma_1]} \dots A'^{[\sigma_N]})^* (A^{[\sigma_1]} \dots A^{[\sigma_N]}), \end{aligned} \quad (2.18)$$

using the orthonormality of the local basis  $\langle\sigma'_k|\sigma_l\rangle = \delta_{kl}\delta_{\sigma'_k\sigma_k}$ . In principle the order in which these contractions are carried out is irrelevant. It is possible to choose an order in which this summation over the full Hilbert space is carried out more efficiently due to the one-dimensional structure of the matrix product state (see Fig. 2.7 for a graphical explanation). For details on the numerical costs, see App. A.4. Intermediary, calculations in method b) are of order  $\mathcal{O}(dD^3)$ , where in method a) they would be of order  $\mathcal{O}(d^N)$ . Thus, in practice, method a) is significantly slower than the first one and has significantly larger intermediary results.

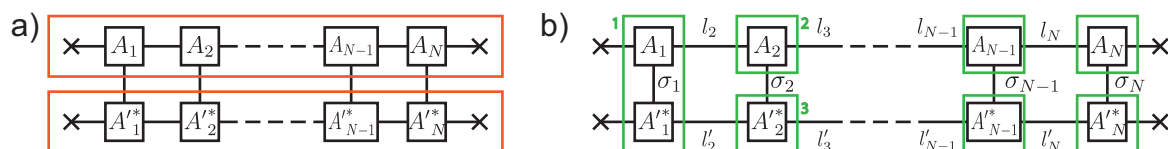


Figure 2.7: Scalar product, computed in two different orders. a) First all  $A$ -matrices of  $|\psi\rangle$  and  $|\psi'\rangle$  are contracted and then one contracts over the local indices. This last contraction is carried out over the full Hilbert space, i.e. a  $1 \times d^N$  matrix is multiplied with a  $d^N \times 1$  matrix, and thus of order  $\mathcal{O}(d^N)$ , which is completely unfeasible for practical purposes. b) First, for site one, one contracts over the local indices of  $A_1$  and  $A'_1$ . Then one contracts over the effective index between  $A_1$  and  $A_2$  and afterwards over the indices between the resulting object and  $(A'_2)^*$ . One proceeds with site three and so on over the whole chain. The most 'expensive' contraction is in the middle of the chain, say at site  $k$ , and it is of order  $\mathcal{O}(dD^3)$ . Here the  $A$ -matrices are viewed as three-index objects  $A_{l_k r_k \sigma_k}$  with dimension  $D \times D \times d$ . All sites left of site  $k$  are represented by a  $D \times D$  matrix, say  $L_{l'_k}^{l_k}$ . Contracting this with the matrix at site  $k$  yields the object  $\sum_{l_k} L_{l'_k}^{l_k} A_{l_k r_k \sigma_k}$ , which has dimensions  $D \times D \times d$ , and since the  $s$  contains  $D$  terms, the overall cost is  $\mathcal{O}(dD^3)$ .

#### Norm

The norm is defined as usual  $\|\psi\| = \sqrt{\langle\psi|\psi\rangle}$ . One may use the global view as in Eq. (2.18). However, in the local view with orthonormal effective basis sets one simply obtains

$$\begin{aligned}
\|\psi\|^2 = \langle \psi | \psi \rangle &= \left( \langle l' | \langle \sigma' | \langle r' | \sum_{l'r'\sigma'} (A_{l'r'}^{\sigma'})^* \right) \left( \sum_{lr\sigma} A_{lr}^\sigma |l\rangle |\sigma\rangle |r\rangle \right) \\
&= \sum_{lr\sigma} |A_{lr}^\sigma|^2.
\end{aligned} \tag{2.19}$$

Thus the norm is determined by the  $A$ -matrix of the current site only.

### Partial product

Sometimes it is required to calculate a product over a part of the matrix product state. This is done the same way as the scalar product:s

$$(P^{[l_k]})_{l_k l'_k} \equiv \sum_{\sigma_1, \dots, \sigma_{k-1}} (A^{[\sigma_1]} \dots A^{[\sigma_{k-1}]} )_{l'_k}^* (A^{[\sigma_1]} \dots A^{[\sigma_{k-1}]} )_{l_k}, \tag{2.20a}$$

$$(P^{[r_k]})_{r_k r'_k} \equiv \sum_{\sigma_{k+1}, \dots, \sigma_N} (A^{[\sigma_{k+1}]} \dots A^{[\sigma_N]} )_{r'_k}^* (A^{[\sigma_{k+1}]} \dots A^{[\sigma_N]} )_{r_k}, \tag{2.20b}$$

$$(P^{[kk']})_{r_k r'_k, l_k l'_k} \equiv \sum_{\sigma_{k+1}, \dots, \sigma_{k'-1}} (A^{[\sigma_{k+1}]} \dots A^{[\sigma_{k'-1}]} )_{r'_k l'_k}^* (A^{[\sigma_{k+1}]} \dots A^{[\sigma_{k'-1}]} )_{r_k l_k} \tag{2.20c}$$

One has to notice that  $P^{[l_k]}$  and  $P^{[r_k]}$  are matrices in the index  $l_k$  and the index  $r_k$ , respectively (see Fig. 2.8). In fact, they correspond to the overlap matrices  $\langle l'_k | l_k \rangle$  and  $\langle r'_k | r_k \rangle$ , respectively.

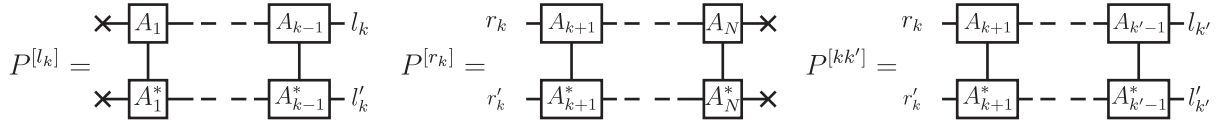


Figure 2.8: Partial products associated with site  $k$ .

### 2.1.6 Reduced density matrix

The pure density matrix given by the matrix product state  $|\psi\rangle$  is defined as  $\rho = |\psi\rangle \langle \psi|$  (see Fig. 2.9).

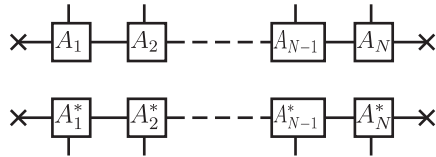


Figure 2.9: Density Matrix

The reduced density matrix is calculated as follows. Let  $I$  be a set of sites of which one wants a reduced density matrix, and  $\sigma_s = \{\sigma_{k \in I}\}$  be a fused index for their local states. All other sites with combined index  $\sigma_b = \{\sigma_{k \notin I}\}$  are traced out. The subscripts s and b stand for system and bath.

$$\rho_I = \sum_{\sigma_1, \dots, \sigma_N, \sigma'_1, \dots, \sigma'_N} \delta_{\sigma_b, \sigma'_b} \left( A^{[\sigma'_1]} \dots A^{[\sigma'_N]} \right)^* \left( A^{[\sigma_1]} \dots A^{[\sigma_N]} \right) |\sigma_s\rangle \langle \sigma'_s|. \quad (2.21)$$

This is a completely general expression, but in the cases where  $I = \{k\}$  or  $I = \{k, k'\}$  it reduces to (see Fig. 2.10)

$$\rho_{\{k\}} = P^{[k]} \left( A^{[\sigma_k]} \otimes \left( A^{[\sigma'_k]} \right)^* \right) P^{[r_k]} |\sigma_k\rangle \langle \sigma'_k|, \quad (2.22a)$$

$$\rho_{\{kk'\}} = P^{[k]} \left( A^{[\sigma_k]} \otimes \left( A^{[\sigma'_k]} \right)^* \right) P^{[kk']} \left( A^{[\sigma_{k'}]} \otimes \left( A^{[\sigma'_{k'}]} \right)^* \right) P^{[r_{k'}]} |\sigma_k\rangle |\sigma_{k'}\rangle \langle \sigma'_k| \langle \sigma'_{k'}|. \quad (2.22b)$$

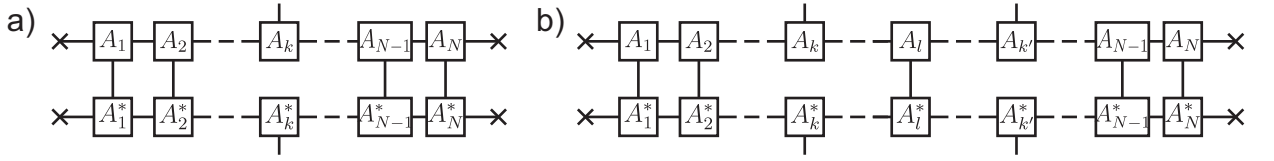


Figure 2.10: Reduced density matrix a)  $\rho_{\{k\}}$  for site  $k$  and b)  $\rho_{\{kk'\}}$  for sites  $k$  and  $k'$ , where  $k < l < k'$ .

### 2.1.7 Operators in an effective basis

Let  $k$  be the current site with orthonormal effective basis sets  $|l_k\rangle$  and  $|r_k\rangle$ . Consider an operator  $B$ , which acts on the local basis of site  $k-1$  only, with matrix elements  $B_{\sigma'_{k-1}\sigma_{k-1}} = \langle \sigma'_{k-1} | B | \sigma_{k-1} \rangle$ . This is called the  $(k-1)$ -local-representation of  $B$ . To represent  $B$  in the effective left basis of site  $k$ , called the  $k$ -left-representation of  $B$ , one may use the following formula (see Fig. 2.11):

$$\begin{aligned} \langle l'_k | B | l_k \rangle &= \left( \langle l'_{k-1} | \langle \sigma'_{k-1} | \sum_{l'_{k-1}, \sigma'_{k-1}} \left( A_{l'_{k-1} l'_k}^{[\sigma'_{k-1}]} \right)^* \right) B_{\sigma'_{k-1} \sigma_{k-1}} \left( \sum_{l_{k-1}, \sigma_{k-1}} A_{l_{k-1} l_k}^{[\sigma_{k-1}]} | l_{k-1} \rangle | \sigma_{k-1} \rangle \right) \\ &= \sum_{l_{k-1}, \sigma'_{k-1}, \sigma_{k-1}} \left( A_{l_{k-1} l'_k}^{[\sigma'_{k-1}]} \right)^* A_{l_{k-1} l_k}^{[\sigma_{k-1}]} B_{\sigma'_{k-1} \sigma_{k-1}}. \end{aligned} \quad (2.23)$$

The only condition that was used to derive these results, was that site  $k-1$  has an orthonormal effective left basis. So one can extend this result to sites farther left of site  $k$  because all sites left of site  $k$  have orthonormal effective left basis sets.

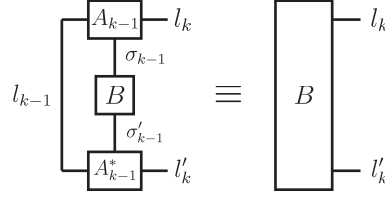


Figure 2.11: The  $k$ -left-representation of the operator  $B$ , obtained from its  $(k-1)$ -local-representation.

Similarly, if the  $(k-1)$ -left-representation of an operator  $C$  is known, its  $k$ -left-representation can be obtained from (see Fig. 2.12):

$$\begin{aligned}
 \langle l'_k | C | l_k \rangle &= \left( \langle l'_{k-1} | \langle \sigma'_{k-1} | \sum_{l'_{k-1}, \sigma'_{k-1}} \left( A_{l'_{k-1} l'_k}^{[\sigma'_{k-1}]} \right)^* \right) C_{l'_{k-1} l_{k-1}} \left( \sum_{l_{k-1} \sigma_{k-1}} A_{l_{k-1} l_k}^{[\sigma_{k-1}]} | l_{k-1} \rangle | \sigma_{k-1} \rangle \right) \\
 &= \sum_{l_{k-1} l'_{k-1} \sigma_{k-1}} \left( A_{l'_{k-1} l'_k}^{[\sigma_{k-1}]} \right)^* A_{l_{k-1} l_k}^{[\sigma_{k-1}]} C_{l'_{k-1} l_{k-1}}. \quad (2.24)
 \end{aligned}$$

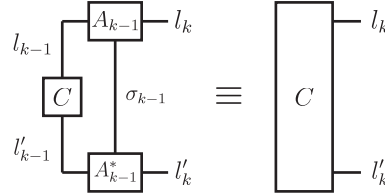


Figure 2.12: The  $k$ -left-representation of the operator  $C$ , obtained from its  $(k-1)$ -left-representation.

Eqs. (2.23) and (2.24) can be used iteratively to transcribe the  $i$ -local-representation of  $B$  into its  $k$ -left-representation for any  $k > i$  (see Fig. 2.13).

$$B_{\sigma'_i \sigma_i} \longrightarrow B_{l'_{i+1} l_{i+1}} \longrightarrow B_{l'_{i+2} l_{i+2}} \longrightarrow \dots \longrightarrow B_{l'_k l_k}$$

Figure 2.13: Iterative calculation of the  $k$ -left-description of an operator  $B$ , given in the  $i$ -local-description, by Eqs. (2.23) and (2.24) for any  $k > i$ .

This reasoning applies also to the right site of site  $k$  and so it is possible to obtain a description of a single operator on any site. To obtain a description of a pair of operators one has to use the following procedure. Let site  $k$  be the current site with orthonormal effective basis sets and  $B, C$  two operators acting locally on site  $i$  and  $j$  respectively ( $i < j < k$ ). First one obtains the  $j$ -left-representation of  $B$ ,  $B_{l'_j l_j}$  as described above. Then both operators are transformed together into the  $(j+1)$ -left-representation (see Fig. 2.14),

$$\langle l'_{j+1} | (BC) | l_{j+1} \rangle = \sum_{l'_j, \sigma'_j} \left( A_{l'_j l'_{j+1}}^{[\sigma'_j]} \right)^* A_{l_j l_{j+1}}^{[\sigma_j]} B_{l'_j l_j} C_{\sigma'_j \sigma_j}, \quad (2.25)$$

which in turn can be transformed iteratively into the desired  $k$ -left-representation of the operators  $B$  and  $C$ .

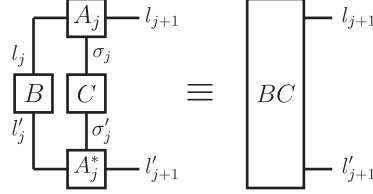


Figure 2.14: The  $(j + 1)$ -left-representation of the operator  $C$ , given in the  $j$ -local-representation, and  $B$ , given in the  $j$ -left-representation.

### 2.1.8 Local operators acting on $|\psi\rangle$

Any combination of operators can be calculated directly in the global view or in the local view, via the effective descriptions introduced in the previous section.

#### Global view

The operators, known in the local basis of the site they are acting on, are contracted directly with the corresponding  $A$ -matrix. For example, the formula for a nearest neighbour hopping term  $c_k^\dagger c_{k+1}$  (see Fig. 2.15) reads as

$$c_k^\dagger c_{k+1} |\psi\rangle = \sum_{\sigma_1, \dots, \sigma_N} \left( \sum_{\sigma'_k} (c_k^\dagger)_{\sigma'_k \sigma_k} \right) \left( \sum_{\sigma'_{k+1}} (c_{k+1})_{\sigma'_{k+1} \sigma_{k+1}} \right) (A^{[\sigma_1]} \dots A^{[\sigma_N]}) |\sigma_1\rangle \dots |\sigma_{k-1}\rangle |\sigma'_k\rangle |\sigma'_{k+1}\rangle |\sigma_{k+2}\rangle \dots |\sigma_N\rangle. \quad (2.26)$$

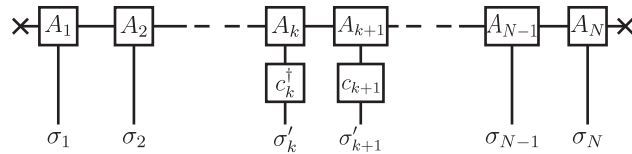


Figure 2.15: The nearest neighbour hopping term  $c_k^\dagger c_{k+1}$  acting on  $|\psi\rangle$  in the global view.

### Local view

Let  $k$  be the current site with orthonormal effective basis sets. If one wants to evaluate operators acting on other sites than the current site  $k$ , one needs an effective description of these operators in one of the effective basis sets of site  $k$  and then one can contract these operators with the  $A$ -matrix of the current site. For example, to calculate the action of the nearest neighbour hopping term  $c_k^\dagger c_{k+1}$  on  $|\psi\rangle = A_{lr}^{[\sigma]} |l\rangle |\sigma\rangle |r\rangle$ , one needs  $(c_k^\dagger)_{\sigma'\sigma}$  and  $(c_{k+1})_{r'r}$  and obtains (see Fig. 2.16)

$$c_k^\dagger c_{k+1} |\psi\rangle = \sum_{r\sigma} \left( \sum_{\sigma'} (c_k^\dagger)_{\sigma'\sigma} \right) \left( \sum_{r'} (c_{k+1})_{r'r} \right) A_{lr}^{[\sigma]} |l\rangle |\sigma'\rangle |r'\rangle . \quad (2.27)$$

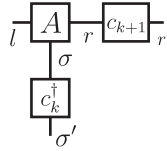


Figure 2.16: The nearest neighbour hopping term  $c_k^\dagger c_{k+1}$  acting on  $|\psi\rangle$  in the local view.

### 2.1.9 Expectation values

Expectation values are merely the scalar product between the state with itself including the action of an operator and can so easily be worked out in both the global and the local view (see Fig. 2.17).

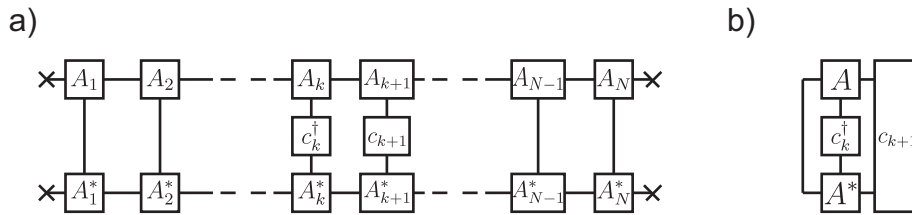


Figure 2.17: The expectation value of the nearest neighbour hopping  $c_k^\dagger c_{k+1}$  in a) the global view and b) the local view.

Since both methods are equivalent, the local variant is much more efficient as it involves much less matrix multiplications. However, it requires careful orthonormalization of the remainder of the  $A$ -matrices. The iterative scheme, introduced in Sec. 2.2, allows for that and works in the local picture.

## 2.2 Variational optimization scheme

All the basic principles introduced in the previous sections strongly suggest an iterative scheme to determine the ground state in the usual DMRG sense. This scheme starts at some

site as current site, for example the first site where truncation occurs, and minimizes the energy of  $|\psi\rangle$  with respect to that site. Afterwards the current site is shifted to the next site, and the energy of  $|\psi\rangle$  with respect to that site is minimized. This is repeated until the last site where truncation occurrence is reached and the direction of the switches is reversed. When the starting site is reached again, one *sweep* has been finished (see Fig. 2.18). These sweeps are repeated until  $|\psi\rangle$  converges.

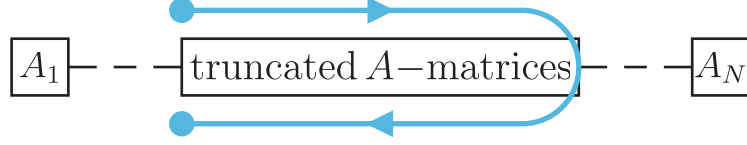


Figure 2.18: One complete sweep.

### 2.2.1 Energy minimization of the current site

In order to find the ground state of the system one has to minimize the energy  $E = \langle\psi| H |\psi\rangle$  of the matrix product state  $|\psi\rangle$  with the constraint that the norm of  $|\psi\rangle$  must not change. Introducing  $\lambda$  as Lagrange multiplier [4] to ensure proper normalization, one obtains

$$\min_{|\psi\rangle} (\langle\psi| H |\psi\rangle - \lambda \langle\psi|\psi\rangle) . \quad (2.28)$$

In the sweeping procedure introduced above, one changes the current site from one site to the next and minimizes the energy in each local description. Thus, one needs Eq. (2.28) in terms of the parameters of the current site. Inserting Eq. (2.3) into Eq. (2.28) yields (see Fig. 2.19)

$$\min_{A^{[\sigma]}} \left( \sum_{lr\sigma'l'r'\sigma'} (A_{l'r'}^{[\sigma']})^* H_{l'r'\sigma'l'r\sigma} A_{lr}^{[\sigma]} - \lambda \sum_{lr\sigma} (A_{lr}^{[\sigma]})^* A_{lr}^{[\sigma]} \right) , \quad (2.29)$$

where  $H_{l'r'\sigma'l'r\sigma} = \langle l' | \langle \sigma' | \langle r' | H | l \rangle | \sigma \rangle | r \rangle$  is the Hamiltonian expressed in the two orthonormal effective basis sets and the local basis of the current site.

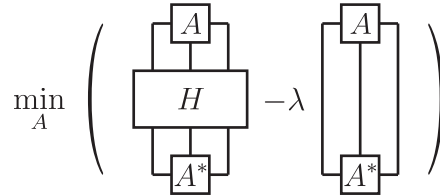


Figure 2.19: The minimization problem expressed in the current site.

The multidimensional minimization problem Eq. (2.28) has been transformed to a local minimization problem where one  $A$ -matrix is optimized at a time and all others are kept constant. Such a procedure could, in principle, cause the system to get stuck in a local

minimum in energy, but it has been shown that for constant couplings and short-range interactions the procedure works well [3].

To obtain a solution for Eq. (2.29), one differentiates the equation with respect to  $(A_{l'r'}^{[\sigma']})^*$ , as the Hilbert space has an hermitian scalar product, obtaining

$$0 = \sum_{l'r'\sigma'} H_{l'r'\sigma'lr\sigma} A_{lr}^{[\sigma]} - \lambda A_{l'r'}^{[\sigma']}. \quad (2.30)$$

Changing to matrix notation and replacing  $\lambda$  with  $E_0$  in anticipation, one obtains an eigenvalue equation:

$$H A_{lr}^{[\sigma]} |l\rangle |\sigma\rangle |r\rangle = E_0 A_{lr}^{[\sigma]} |l\rangle |\sigma\rangle |r\rangle. \quad (2.31)$$

The minimization problem has been transformed to a local eigenvalue problem, which can be solved by standard techniques. The full Hilbert space of the current site has dimension  $dD^2$  and may become very large, but it is not necessary to determine the full spectrum of  $H$ , since but one is interested only in the ground state. The Lanczos algorithm [9] is an effective algorithm to achieve exactly that. The advantage of this algorithm is that one only has to compute  $H|\psi\rangle$ , which saves much effort. The matrix elements  $H_{l'r'\sigma'lr\sigma}$  may be calculated easily from Eq. (1.5) using the techniques introduced in Sec. 2.1 (see Sec. 2.2.2 for details).

## 2.2.2 Sweeping details

Before the actual sweeping may be started one has to set up an initial state, prepare a current site with orthonormal effective basis sets and calculate effective descriptions of operators which occur in the Hamiltonian. After this initialization one may determine the ground state with respect to this current site and shift the current site to the next site. That current site again has orthonormal effective basis sets due to the switching procedure introduced in Sec. 2.1.3, but one also needs effective representations of the operators occurring in the Hamiltonian. At this step the structure of the matrix product state saves much effort, as most of the needed representations are already calculated!

### Structure of the Hamiltonian terms

The Hamiltonian  $H_{l'r'\sigma'lr\sigma}$ , acting in the local space spanned by the states  $|l\rangle$ ,  $|\sigma\rangle$ ,  $|r\rangle$ , breaks up into several terms:

$$\begin{aligned} H_{l'r'\sigma'lr\sigma} = & \mathbb{1}_{l'l} \otimes (H_{\bullet})_{\sigma'\sigma} \otimes \mathbb{1}_{r'r} + (H_L)_{l'l} \otimes \mathbb{1}_{\sigma'\sigma} \otimes \mathbb{1}_{r'r} + \mathbb{1}_{l'l} \otimes \mathbb{1}_{\sigma'\sigma} \otimes (H_R)_{r'r} \\ & + (H_{L\bullet})_{l'l\sigma'\sigma} \otimes \mathbb{1}_{r'r} + \mathbb{1}_{l'l} \otimes (H_{\bullet R})_{r'r\sigma'\sigma} + (H_{L\bullet R})_{l'l r'r\sigma'\sigma}, \end{aligned} \quad (2.32)$$

where the indices denote on which parts of the system the respective term works on ( $L$  and  $R$  indicate left and right of the current site, respectively,  $\bullet$  locally on the current site). Of

course, the six terms of Eq. (2.32) depend on the current site  $k$ :  $H_{\bullet}^{(k)}$ ,  $H_L^{(k)}$ ,  $H_R^{(k)}$ ,  $H_{L\bullet}^{(k)}$ ,  $H_{\bullet R}^{(k)}$  and  $H_{L\bullet R}^{(k)}$ . In the case of the Hamiltonian in Eq. (1.5),  $(H_{\bullet})_{\sigma'\sigma}$  consists of the rung hopping terms and the nearest neighbour repulsion along the rung,  $(H_{L\bullet})_{l'l'\sigma'\sigma}$  consists of nearest neighbour hopping, correlated hopping and nearest neighbour repulsion along legs with site  $k$  as rightmost site.  $(H_{\bullet R})_{r'r'\sigma'\sigma}$  is defined similarly with site  $k$  as leftmost site and  $(H_{L\bullet R})_{l'l'r'r'\sigma'\sigma}$  consists of the correlated hopping terms with site  $k$  as middle site. The terms  $(H_L)_{l'l}$  and  $(H_R)_{r'r}$  contain all terms which involve only sites  $k' < k$  and  $k' > k$ , respectively. One easily verifies the following equalities:

$$H_L^{(k+1)} = H_L^{(k)} + H_{L\bullet}^{(k)} + H_{\bullet}^{(k)}, \quad (2.33a)$$

$$H_R^{(k-1)} = H_{\bullet}^{(k)} + H_{\bullet R}^{(k)} + H_R^{(k)}, \quad (2.33b)$$

where the terms on the right hand side are meant to be transformed in the effective basis of the operator on the left hand site (see Fig. 2.20).

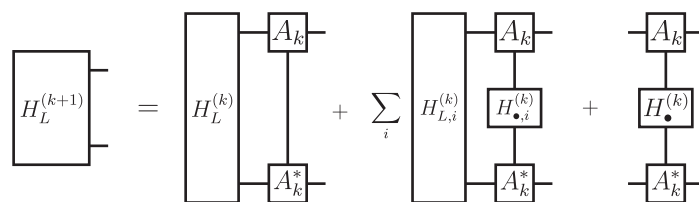


Figure 2.20: Iterative calculation of the operator  $H_L^{(k+1)}$ . The sum over  $i$  indicates that  $H_{L\bullet}^{(k)}$  has the form  $\sum_i H_{L,i}^{(k)} \otimes H_{\bullet,i}^{(k)}$ , where  $H_{L,i}^{(k)}$  acts only on sites  $k' < k$  and  $H_{i,\bullet}^{(k)}$  only on site  $k$ .

The calculation of  $H_R^{(k-1)}$  works analogously.

## Initialization

First of all one needs an initial matrix product state, which is most conveniently chosen to consist of identity transformations at the ends of the chain (see Sec. 2.1.2) and random  $A$ -matrices for the rest of the chain. One starts with the first site where Hilbert space truncation is applied as current site  $k$  and needs an orthonormal effective right basis (the effective left basis is already orthonormal). It can be obtained using the orthonormalization procedure introduced in Sec. 2.1.3 starting from site  $N$ . Additionally it is convenient, while dealing with site  $N$ , to calculate and *store* the operator  $H_R^{(N-1)}$  (see Eq. (2.33b)) and the effective description in the effective right basis of site  $N-1$  of all operators of site  $N$  (see Sec. 2.1.7), which contribute to  $H_{\bullet R}^{(k)}$  and  $H_{L\bullet R}^{(k)}$ . This ensures when the sweeping procedure reaches site  $N-1$ , that all necessary operators are already calculated. This is repeated from site  $N$  down to site  $k+1$ , and similarly for the sites  $k' < k$  in the other direction. The result of these initialization steps is that one has a current site  $k$  with orthonormal effective basis sets, effective descriptions of the Hamiltonian terms  $H_L^{(k)}$  and  $H_R^{(k)}$  and effective descriptions of all operators contributing to  $H_{L\bullet}^{(k)}$ ,  $H_{\bullet R}^{(k)}$  and  $H_{L\bullet R}^{(k)}$ . Moreover, with an appropriate extension to the switching procedure of Sec. 2.1.3, all effective descriptions for other current sites are available for use when needed in future sweeping steps.

### Extended switching procedure

The switching procedure of Sec. 2.1.3 is applied as before. Additionally, depending on the direction of the switch,  $H_L^{(k+1)}$  or  $H_R^{(k-1)}$  are calculated and stored. Also the operators needed for the Hamiltonian Eq. (2.32) are calculated and stored (see Fig. 2.21). This extended switching ensures that for the new current site all required operators are calculated and available, if they had been for the old current site.

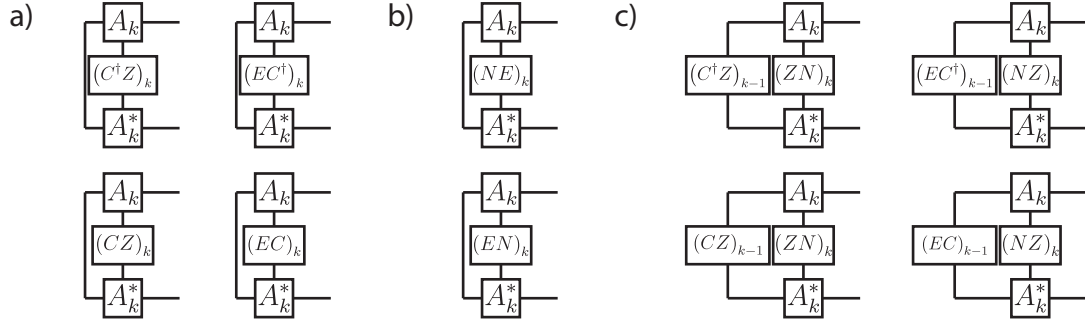


Figure 2.21: The operators, calculated in an extended switch from site  $k$  to site  $k + 1$ , for the Hamiltonian in Eq. (1.5) with site  $k + 1$  as current site. The operators a) are needed for the nearest neighbour hopping along legs, the operators b) are needed for the nearest neighbour repulsion along legs and the operators c) are needed for the correlated hops. The extended switch from site  $k$  to site  $k - 1$  works analogously.

### Complete ground state calculation

The methods introduced above make the procedure to determine the ground state very efficient, because the global problem is mapped onto many local problems involving only a few terms to calculate. The iterative structure of the matrix product states and the effective Hamiltonian terms strongly increase the efficiency. So one full ground state calculation consists of:

1. Initialization as described above
2. Full sweeps from site 2 to site  $N - 1$  and back to site 2.
3. After each sweep  $i$  the overlap  $\langle \psi_{i-1} | \psi_i \rangle$  between the state before and after the sweep is calculated. If the matrix product state does not change any more, stop the sweeping. A criterion, for example, for when to stop would be to require that

$$\frac{|\langle \psi_{i-1} | \psi_i \rangle - \langle \psi_{i-2} | \psi_{i-1} \rangle|}{|\langle \psi_{i-1} | \psi_i \rangle|} \leq \epsilon, \quad (2.34)$$

where  $\epsilon$  is a small control parameter, typically of order  $10^{-10}$  to  $10^{-13}$ .

### 2.2.3 Numerical costs

The step with the most impact on the numerical costs of the algorithm is the calculation of  $H|\psi\rangle$  in the Lanczos method. This method is an iterative scheme using several *Lanczos steps*, of which usually less than 100 are needed for one ground state calculation. Each Lanczos step calculates  $H|\psi\rangle$  exactly once. This calculation basically consists of elementary matrix multiplications, see App. A.4 for details on the numerical costs of such calculations.

The six terms introduced in Eq. (2.32) are not all equally time consuming. Most of them contain identity maps which do not need to be carried out. Furthermore it is more efficient to contract operators of different Hilbert spaces successively instead of contracting the direct product of them at once (see Fig. 2.22).

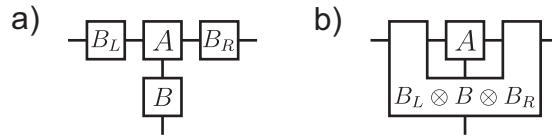


Figure 2.22: Two ways of contracting the operators  $B_L$  acting on the effective left basis,  $B$  acting on the local basis and  $B_R$  acting on the effective right basis onto an  $A$ -matrix: a) The efficient way, where the three operators are contracted onto  $A$  step by step. Its numerical cost is of order  $\mathcal{O}(dD^2(D + D + d))$  (the resulting object always consists of  $dD^2$  entries, and matrix multiplications by  $B_L$ ,  $B$  or  $B_R$  involves summing over an index with dimension  $D$ ,  $d$ , or  $D$  respectively). b) The inefficient way, where the three operators are contracted onto  $A$  in one step. It is of order  $\mathcal{O}(d^2D^4)$  (the resulting object consists of  $dD^2$  entries and one applies  $dD^2$  multiplications for each value).

Thus the term  $H_{L\bullet R}$  is the most time consuming term and it is of order

$$C_{L\bullet R} = \mathcal{O}(dD^2(2D + d)) , \quad (2.35)$$

where  $C$  stands for the cost. The other terms are of order  $C_\bullet = \mathcal{O}(d^2D^2)$ ,  $C_L = \mathcal{O}(dD^3) = C_R$  and  $C_{L\bullet} = \mathcal{O}(dD^2(D + d)) = C_{\bullet R}$ . Thus the total numerical cost for the minimization process is

$$C = N_{\text{Sweep}} \times 2N \times N_{\text{Lanczos}} \times (dD^2(2D + d)) , \quad (2.36)$$

where  $N_{\text{Sweep}}$  is the number of sweeps,  $N$  is the chain length and  $N_{\text{Lanczos}}$  is the number of Lanczos steps. In practice the cutoff dimension is significantly higher than the local Hilbert space dimension  $d$ . Thus the total cost is linear in  $d$ .

In Sec. 1.1 was stated that the numerical approach does not benefit as much from considering the limit of infinite nearest neighbour repulsion as the analytical approach. We are now in a position to make that statement somewhat more precise: this limit could in fact be exploited to achieve a modest speedup for the numerical approach if one would reduce the local Hilbert space dimension  $d$  from 4 to 3. But the numerical costs depend much more strongly on the

cutoff dimension  $D$ , and thus this reduction has not been implemented. Moreover, by not implementing this reduction in the local Hilbert space is to retain the possibility to set the nearest neighbour repulsion to zero, which is needed for comparison with the results of Sec. 1.2. Note that even for infinite nearest neighbour repulsion, the numerical approach cannot exclude a priori configurations containing nearest neighbours on the same leg, but different rungs. These are excluded by the energy minimization procedure.

## Chapter 3

# Matrix product state method for infinite systems

A method designed for finite systems, like the one introduced in Chap. 2, can in principle also be used to study the thermodynamic limit of infinite (one-dimensional) systems, provided that the properties of the finite system converge with increasing system sizes. Nevertheless, artefacts of the finite size will always remain. To overcome this weakness, G. Vidal proposed a method based on matrix product states and translational symmetry [7]. In this method (*infinite*) *matrix product states* are introduced, which describe an infinite one-dimensional system in an efficient way. Translational symmetry is exploited to reduce the number of independent  $A$ -matrices. This method may be improved in several ways [10], but in this thesis the original method of G. Vidal is presented.

Again, as in Chap. 2, the Jordan-Wigner transformation (see App. A.1) is applied throughout for practical purposes before any calculations are made.

### 3.1 Construction of infinite matrix product states

Consider an infinite one-dimensional lattice consisting of equivalent sites labeled by  $i \in \mathbb{Z}$ , with a local state space of dimension  $d$ . One may split this lattice into two semi-infinite sublattices  $L_k \equiv \{-\infty, \dots, k\}$  and  $R_{k+1} \equiv \{k+1, \dots, \infty\}$ . The Schmidt decomposition of a single state  $|\psi\rangle$  then reads as

$$|\psi\rangle = \sum_{n=1}^D s_n^{[k]} |\psi_n^{[L_k]}\rangle \otimes |\psi_n^{[R_{k+1}]}\rangle, \quad (3.1)$$

where  $|\psi_n^{[L_k]}\rangle$  and  $|\psi_n^{[R_{k+1}]}\rangle$  are the Schmidt basis sets describing the left and the right sublattice, respectively, which are not necessarily orthonormal in the given context. The coefficients  $s_n^{[k]}$  are defined to be positive (see Fig. 3.1). The Schmidt rank is called  $D$  in anticipation, because this turns out to be the parameter which governs truncation in a manner very similar to the two-site DMRG introduced in Sec. 2.1.4. Although for an infinite system  $D$  is a priori

infinite, we take it to be finite, thereby effectively implementing a truncation scheme. In contrast to the DMRG approach, it is unclear how to find an optimal choice for  $D$ . Starting from Eq. (3.1) one could construct reduced density matrices for the left or right system by tracing out the complementary system, but without an orthonormal basis, these reduced density matrices are not of much use and the cutoff of the Hilbert spaces is rather uncontrolled. In fact, this point is not addressed by G. Vidal and thus several values of  $D$  have to be tried and their influence on the result has to be compared.

It is straightforward to relate the Schmidt basis sets for two left (right) sublattices, referring to neighbouring sites  $k$  and  $k \pm 1$ :

$$|\psi_n^{[L_k]}\rangle = \sum_{m=1}^D \sum_{\sigma=1}^d s_m^{[k-1]} \Gamma_{mn\sigma}^{[k]} |\psi_m^{[L_{k-1}]}\rangle |\sigma^{[k]}\rangle, \quad (3.2a)$$

$$|\psi_n^{[R_k]}\rangle = \sum_{m=1}^D \sum_{\sigma=1}^d \Gamma_{mn\sigma}^{[k]} s_m^{[k]} |\sigma^{[k-1]}\rangle |\psi_m^{[R_{k+1}]}\rangle, \quad (3.2b)$$

where the basis sets are related by the three-index tensor  $\Gamma^{[k]}$ . One may write the state in terms of one of these tensors and obtains (see Fig. 3.1)

$$|\psi\rangle = \sum_{n,m=1}^D \sum_{\sigma=1}^d s_n^{[k-1]} \Gamma_{nm\sigma}^{[k]} s_m^{[k]} |\psi_n^{[L_{k-1}]}\rangle |\sigma^{[k]}\rangle |\psi_m^{[R_{k+1}]}\rangle, \quad (3.3)$$

which is very similar to Eq. (2.3) in structure. If one defines  $A_{l_k r_k \sigma_k}^{[\sigma_k]} \equiv \left( \sqrt{s^{[k-1]}} \Gamma^{[k]} \sqrt{s^{[k]}} \right)_{l_k r_k \sigma_k}$ ,  $|l_k\rangle \equiv |\psi_{l_k}^{[L_{k-1}]}\rangle$  and  $|r_k\rangle \equiv |\psi_{r_k}^{[R_{k+1}]}\rangle$  for all  $k$ , one actually obtains (see Fig. 3.1)

$$|\psi\rangle = \sum_{l_k r_k \sigma_k} A_{l_k r_k \sigma_k}^{[\sigma_k]} |l_k\rangle |\sigma_k\rangle |r_k\rangle, \quad (3.4)$$

where the effective basis sets transform exactly as in Eq. (2.4).

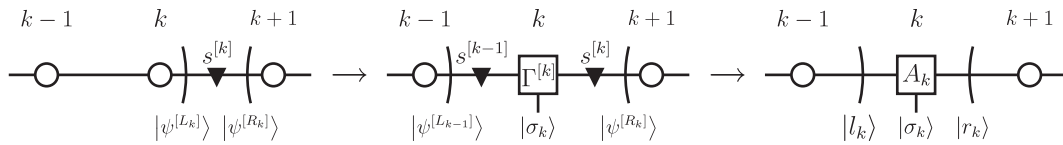


Figure 3.1: The steps which lead to a description of the infinite lattice via  $A$ -matrices.

Thus one has a description of the state by infinitely many  $A$ -matrices. This, of course, is not very convenient in practice and one has to exploit another property of the system: the assumed translational invariance of the Hamiltonian (e.g. that of Eq. (1.5)). Assuming the ground state to be invariant under translation, all  $A$ -matrices have to be equal to fulfill this property of a ground state. This simplifies the problem considerably, because one effectively

describes an infinite system by exactly one or more generally just by a few  $A$ -matrices. One may allow for a partial breaking of translational symmetry by introducing  $M$  independent  $A$ -matrices  $A^{[\sigma_1]}, \dots, A^{[\sigma_M]}$ , which form a *block*. This block is repeated infinitely often instead of a single  $A$ -matrix. This description of  $|\psi\rangle$  is still fully general, because if no long range order arises, the matrices  $A^{[\sigma_1]}, \dots, A^{[\sigma_M]}$  may become all the same. As the system is described by only these  $M$  matrices, the labeling of the  $A$ -matrices with  $i \in \mathbb{Z}$  is dropped and replaced by the labelling  $1, \dots, M$ . Thus for a certain site  $i$  the corresponding  $A$ -matrix is  $A^{[\sigma_n]}$  with  $n = (i - 1) \bmod (M + 1)$ .

The introduction of several  $A$ -matrices is useful to apply the time evolution operator onto an infinite matrix product state (see Sec. 3.3). It also allows for the  $A$ -matrices to be not all the same, which may be necessary for certain ground states. Consider a ground state being a charge density wave, i.e. every second site is occupied with the intermediate sites unoccupied. Obviously, this ground state is degenerate as one may shift the arrangement by one site without changing the energy. In general the ground state would be a linear superposition of these two states, but the matrix product state method tends to spontaneous symmetry breaking, by favouring one of the two states. For the linear superposition of the two symmetry-broken states every  $A$ -matrix may be the same, but for one of the two charge density waves two adjacent sites have to be different. Thus, if one describes the system by only one  $A$ -matrix the method may not converge, because it tries to describe one charge density wave, which it cannot. To overcome this problem, one would have to significantly increase the cutoff dimension  $D$ , which lowers the efficiency of the method.

## 3.2 Details of infinite matrix product states

Infinite matrix product states (IMPS) are, in spite of many similarities, quite different from finite matrix product states. It is not possible to implement a well-defined norm or scalar product between two different infinite matrix product states. In general it would be either zero or infinity due to the infinite repetition of the  $A$ -matrices. Furthermore, the effective basis sets  $|l_k\rangle$  and  $|r_k\rangle$  are not orthonormal in the prescription given by G. Vidal (there is one in [10]). There is no local view, and with non-orthonormal basis sets a local view would not be of much use. In fact it is not needed, because only a few matrices are considered in any case.

### 3.2.1 Expectation values

From the previous section it is clear in principle how to calculate an expectation value. Contract all  $A$ -matrices from left to right with their corresponding  $A^*$ -matrices (their complex conjugates) and insert the operators for the expectation value at the sites they are acting on. The contraction of the  $A$ -matrices of one block with their corresponding  $A^*$ -matrices is called  $\mathcal{P} = \mathcal{P}_{l_1 l'_1 r_M r'_M}$  (see Eq. (3.5) and Fig. 3.5) and the blocks on which the operators are acting, are called operator blocks,  $\mathcal{O} = \mathcal{O}_{l_1 l'_1 r_M r'_M}$  (see Fig. 3.2).

$$\begin{aligned}
 \mathcal{P} = \mathcal{P}_{l_1 l_1' r_M r_M'} &\equiv \langle \sigma'_1 | \dots \langle \sigma'_M | \left( \sum_{\sigma'_1, \dots, \sigma'_M} \left( A^{[\sigma'_1]} \dots A^{[\sigma'_M]} \right)^* \right)_{l_1' r_M'} \\
 &\left( \sum_{\sigma_1, \dots, \sigma_M} \left( A^{[\sigma_1]} \dots A^{[\sigma_M]} \right) \right)_{l_1 r_M} | \sigma_1 \rangle \dots | \sigma_M \rangle \\
 &= \sum_{\sigma_1, \dots, \sigma_M} \left( A^{[\sigma_1]} \dots A^{[\sigma_M]} \right)^*_{l_1' r_M'} \left( A^{[\sigma_1]} \dots A^{[\sigma_M]} \right)_{l_1 r_M} . \quad (3.5)
 \end{aligned}$$

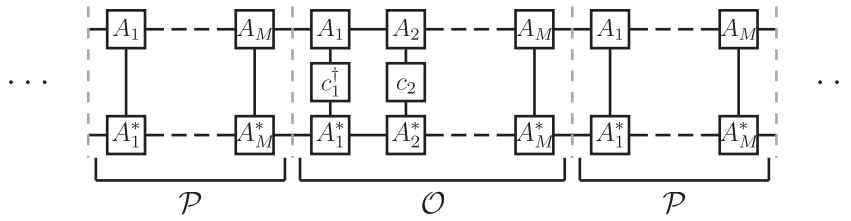


Figure 3.2: The expectation value  $\langle c_1^\dagger c_2 \rangle$  as generalized from Sec. 2.1.9. The block in the middle, where the operators are acting, is the operator block.

This generalization, however does not take into account that the state cannot be normalized. Moreover it is not possible to naively contract all matrices from minus infinity to plus infinity. The first problem may be overcome by calculating normalized expectation values:

$$\langle \cdot \rangle = \frac{\langle \psi | \cdot | \psi \rangle}{\langle \psi | \psi \rangle} , \quad (3.6)$$

though the norm is still ill-defined. Notice however, that apart from the operator blocks, the contraction of the  $A$ -matrices up to minus or plus infinity results in an infinite *repetition* of  $\mathcal{P}$  (see Fig. 3.3).

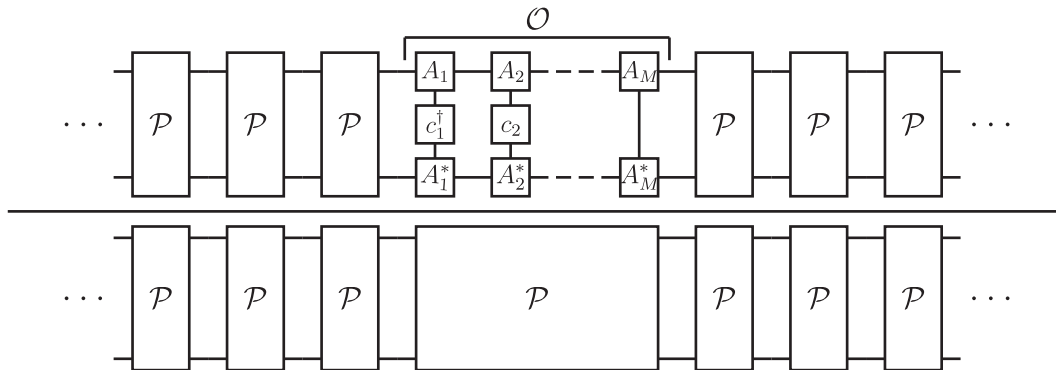


Figure 3.3: Calculation of expectation values via  $\mathcal{P}$ . The expectation value  $\langle c_1^\dagger c_2 \rangle$ , expressed by the operator block  $\mathcal{O}$  and  $\mathcal{P}$ . In this case there is only one operator block. For  $\langle c_1^\dagger c_{M+1} \rangle$  two operator blocks,  $\mathcal{O}_1$  and  $\mathcal{O}_2$ , would arise.

Consider the action of  $\mathcal{P}$  to the right of the operator blocks:  $\mathcal{P}$  is infinitely often multiplied onto the basis states  $|r_M\rangle$  and  $|r'_M\rangle$  of the operator block, the result of this infinite multiplications is nothing else than calculating the overlap matrix between  $|r_M\rangle$  and  $|r'_M\rangle$ . The same reasoning also applies to the left side of the operator block and thus to  $|l_1\rangle$  and  $|l'_1\rangle$ . For the denominator the same reasoning may be applied, except that one would retain one  $\mathcal{P}$  for each operator block in the numerator, to obtain a proper normalization (see Fig. 3.4).

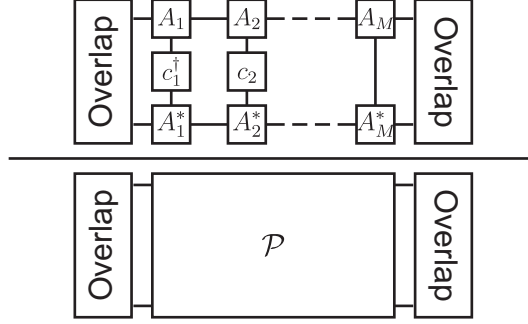


Figure 3.4: The expectation value  $\langle c_1^\dagger c_2 \rangle$ , expressed by the operator block  $\mathcal{O}$ ,  $\mathcal{P}$  and the overlap matrices for the left and the right part.

From the infinite repetition of  $\mathcal{P}$  it is obvious that the left and right eigenvectors  $\langle p_L|$  and  $|p_R\rangle$  associated with the *largest* eigenvalue  $p$  (with respect to the matrix  $\mathcal{P}_{(l_1 l'_1)(r_M r'_M)}$ , see Fig. 3.5) will dominate the result of the infinite multiplications [3, 6, Sec. III]. Thus the overlap matrix  $\langle l'_1 | l_1 \rangle$  between  $|l_1\rangle$  and  $|l'_1\rangle$  turns out to be proportional to  $\langle p_L|$  and the overlap matrix  $\langle r'_M | r_M \rangle$  to  $|p_R\rangle$ . The structure of an overlap matrix which is always hermitian by construction, requires that these eigenvectors, rearranged into matrices of the form  $(p_L)_{l_1 l'_1}$  and  $(p_R)_{r_M r'_M}$ , are hermitian, too.

$$\mathcal{P} = \begin{array}{c} l_1 \\ | \\ \mathcal{P} \\ | \\ l'_1 \end{array} \begin{array}{c} r_M \\ | \\ \mathcal{P} \\ | \\ r'_M \end{array} \equiv \begin{array}{c} l_1 \\ | \\ A_1 \\ | \\ l'_1 \end{array} \text{---} \begin{array}{c} A_M \\ | \\ r'_M \end{array} \begin{array}{c} r_M \\ | \\ \mathcal{P} \\ | \\ r'_M \end{array} = p \begin{array}{c} \langle p_L | \\ | \\ \mathcal{P} \\ | \\ \langle p_L | \end{array} = p \begin{array}{c} \mathcal{P} \\ | \\ |p_R\rangle \\ | \\ \mathcal{P} \end{array} = p \begin{array}{c} |p_R\rangle \\ | \\ \mathcal{P} \\ | \\ |p_R\rangle \end{array}$$

Figure 3.5:  $\mathcal{P}$  with its largest left and right eigenvectors.

The contributions of all other eigenvalues to Eq. (3.6) vanish since in the limit  $l \rightarrow \infty$  the greatest eigenvalue becomes dominant over all other eigenvalues. Thus one obtains the following result assuming only one operator block (see Fig. 3.6):

$$\begin{aligned} \langle \cdot \rangle &= \lim_{l \rightarrow \infty} \frac{\langle p_L | p^l \mathcal{O} p^l | p_R \rangle}{\langle p_L | p^l \mathcal{P} p^l | p_R \rangle} \\ &= \frac{\langle p_L | \mathcal{O} | p_R \rangle}{\langle p_L | p \mathcal{P} p | p_R \rangle}, \end{aligned} \quad (3.7)$$

where  $l$  is the number of multiplications of  $\mathcal{P}$  with itself. For  $n$  operator blocks, the only change is that  $p$  in the denominator is replaced by  $p^n$ . Thus, one arrives at a finite formula for an expectation value involving infinite products.

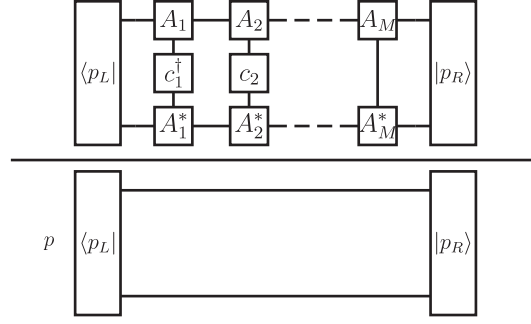


Figure 3.6: The expectation value  $\langle c_1^\dagger c_2 \rangle$  calculated by the finite expression Eq. (3.7).

### 3.2.2 Reduced density matrix

Following the derivation in Sec. 3.2.1, a reduced density matrix is calculated analogously to an expectation value. The operator blocks are replaced by blocks with open local indices, see Fig. 3.7 for a graphical representation.

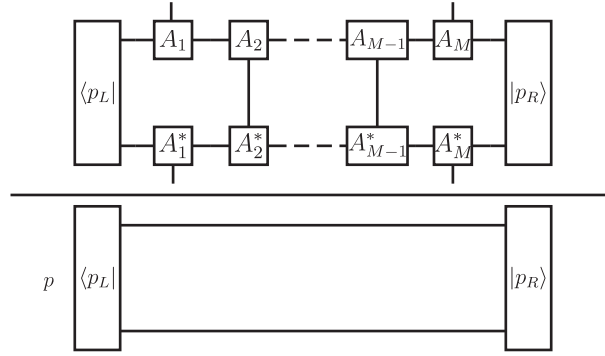


Figure 3.7: Reduced density matrix  $\rho_{kk'}$ , where the sites  $k$  and  $k'$  are within one block (e.g.  $k = 1$  and  $k' = M$ ).

## 3.3 Infinite time evolving block decimation

So far no scheme to obtain a ground state was introduced. Based on ground state calculations on finite systems by time evolving block decimation [11, 12, 13], G. Vidal introduced the infinite time evolving block decimation [7]. The basic idea is to obtain the time evolution of a state by real-time evolution as in Eq. (3.8a), and to obtain the ground state of a system by imaginary-time evolution as in Eq. (3.8b).

$$|\psi(t)\rangle = e^{-iHt} |\psi\rangle, \quad (3.8a)$$

$$|\psi^G\rangle = \lim_{\tau \rightarrow \infty} \frac{e^{-\tau H} |\psi\rangle}{\|e^{-\tau H} |\psi\rangle\|}. \quad (3.8b)$$

### 3.3.1 Decomposition of the time evolution

Eqs. (3.8a) and (3.8b) are standard equations. The question is how to calculate these in our present context, We shall focus on the imaginary time evolution to obtain the ground state. To apply the time evolution operator the Suzuki-Trotter decomposition [14] together with block decimation is used: the Hamiltonian is divided into several parts  $H = \sum_i H_i$ , chosen such that all terms within one part commute with each other. These terms have to contain at least as many as the most far-reaching term in the Hamiltonian (see Fig. 3.8),

$$e^{-\tau H} = e^{-\tau H_1} \dots e^{-\tau H_M} + \mathcal{O}\left(\tau^2 \max_{i,j} \|[H_i, H_j]\|\right), \quad (3.9)$$

where the number of Hamiltonian parts has been called  $M$  in anticipation that it has to be equal to the block size. The individual terms within  $H_i$  may be decomposed into several exponents one by one as they all commute with each other.

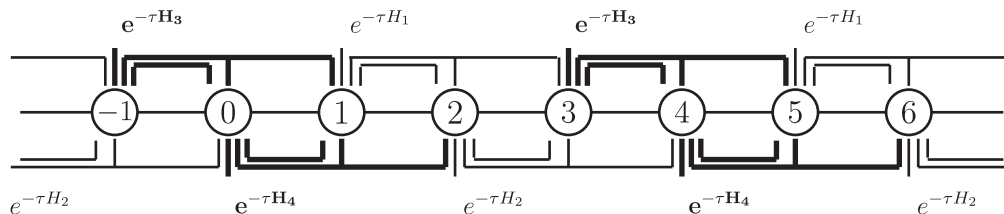


Figure 3.8: The Hamiltonian in Eq. (1.5) divided into four parts, where all terms within one part commute. Single bars denote local terms (rung hopping and nearest neighbour repulsion along rungs), bars connecting two sites denote nearest neighbour interaction (leg hopping and nearest neighbour repulsion along legs) and bars connecting three sites denote correlated hops.

This partitioning scheme is perfectly suited for infinite matrix product states. Consider an infinite matrix product state with a block of size  $M$  and a Hamiltonian that has been split into  $M$  parts,  $H_i$  with  $i = 1, \dots, M$ .  $H_i$  is chosen to contain all terms whose leftmost site is of the form  $i \pm zM$ ,  $z \in \mathbb{Z}$  and of these, all those having the same  $z$  are considered to constitute a single block, called block  $z$  (see Fig. 3.8). Since each block is described by the same  $A$ -matrices, the translational symmetry of the Hamiltonian implies, that the action of  $e^{-\tau H_i}$  on the whole system can be calculated by considering only the terms corresponding to a single choice of  $z$ , acting on the block  $z$  (see Fig. 3.9). After applying all parts of the imaginary time evolution operator one has applied a full imaginary time evolution of time  $\tau$ . Due to this periodic behaviour, the operator  $e^{-\tau H_i}$  will denote just the part acting on a single block in the following.

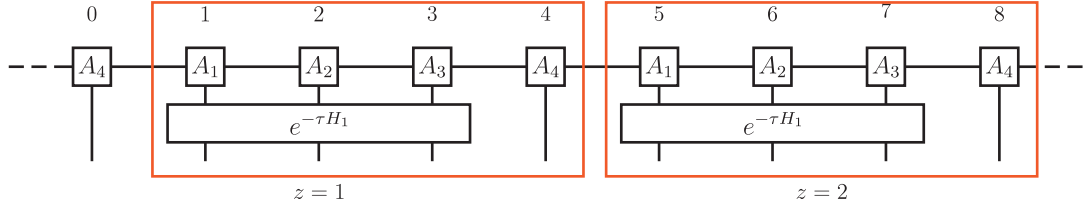


Figure 3.9: The action of  $e^{-\tau H_1}$  onto the infinite matrix product state for the Hamiltonian in Eq. (1.5) with  $M = 4$ .

### 3.3.2 Local operators acting on $|\psi\rangle$

The remaining task for the imaginary time evolution is to apply the operator  $e^{-\tau H_i}$  onto  $|\psi\rangle$ . For simplicity,  $e^{-\tau H_1}$  is chosen as introduced above, which acts on the sites 1, 2 and 3. This operator acts only on the local Hilbert spaces of the corresponding chain sites and thus one only needs to consider their respective  $A$ -matrices. Contracting the indices connecting the three  $A$ -matrices, one obtains (see Fig. 3.10)

$$e^{-\tau H_1} |\psi\rangle \hat{=} \sum_{l_1 \sigma_1 \sigma_2 \sigma_3 \sigma_4 r_4} \sum_{r_3} \left( \sum_{\sigma'_1 \sigma'_2 \sigma'_3} (e^{-\tau H_1})_{\sigma_1 \sigma_2 \sigma_3 \sigma'_1 \sigma'_2 \sigma'_3} (A^{[\sigma'_1]} A^{[\sigma'_2]} A^{[\sigma'_3]})_{l_1 r_3} \right) A^{[\sigma_4]}_{r_3 r_4} |l_1\rangle |\sigma_1\rangle |\sigma_2\rangle |\sigma_3\rangle |\sigma_4\rangle |r_4\rangle. \quad (3.10)$$

Afterwards one has to decompose the resulting object via the singular value decomposition. This is in complete analogy to the procedure introduced in Sec. 2.1.4 for two site DMRG, but in several steps. See Fig. 3.10 for a graphical explanation. Similar to the construction of infinite matrix product states the square root of the singular values is multiplied onto  $u$  and  $v^\dagger$ .

Figure 3.10: Decomposition of the object resulting out of Eq. (3.10) in two steps.

### 3.3.3 Determining the ground state

Summarizing everything introduced above, the ground state is determined by infinite time evolving block decimation as follows:

1. Initialization of a state consisting of  $M$   $A$ -matrices with random entries, where  $M$  has to be larger than the range of the most far-reaching term in the Hamiltonian. The Hamiltonian  $H$  is divided into  $M$  parts as depicted in Fig. 3.8.

2. The time evolution procedure for several choices of the parameter  $\tau$ . The process is sensitive to this choice, very small values of  $\tau$  would be required to minimize the error of the Suzuki-Trotter decomposition (Eq. (3.9)) on the one hand, but large values of  $\tau$  would be required to ensure that  $e^{-\tau H}$  represents a projector onto the ground state. Thus starting with large values of  $\tau$  to reach far in the time-line and to get rid of high energy contributions, one reduces  $\tau$  more and more to minimize the Suzuki-Trotter error (see Eq. (3.9)) and to access smaller energy scales, which are insensitive to greater values of  $\tau$ . There is no best choice as long as one applies the imaginary time evolution for each value of  $\tau$  often enough the energy does not decrease significantly any more. The final  $\tau$  depends on the desired maximal error and on the greatest terms in the Hamiltonian (see Eq. (3.9)).



# Chapter 4

## Correlations

The calculation of the ground state itself in the  $d^N$ -dimensional Hilbert space is only the mathematical prerequisite for calculating the properties of the ground state, even though it is the most time-consuming part. To investigate several properties of a state, one has to calculate appropriate correlators. A correlator is the expectation value of two operators acting on different sites. If one fixes one site and calculates the correlator to another site, which is  $r$  sites apart, one obtains the *correlation function* as a function of the distance  $r$ . Of course this concept is not restricted to two operators acting on two sites. In general one may define a *cluster* as several connected sites and calculate the correlation function of some operators between two clusters as a function of distance.

### 4.1 Correlation functions

One may imagine any combination of operators for a correlation function, but in this thesis basically three correlation functions are considered:  $\langle n_i n_{i+r} \rangle$  and  $\langle c_i^\dagger c_{i+r} \rangle$  as two-site correlation functions (each cluster consists of one site) and  $\langle c_i^\dagger c_{i+1}^\dagger c_{i+r} c_{i+r+1} \rangle$  as four-site correlation function (each cluster consists of two sites). There is one important technicality, since one works with fermionic creation and annihilation operators: correlators with an odd number of creation and annihilation operators in one cluster 'produce' fermionic signs. This can be seen in the Jordan-Wigner transformed (see App. A.1) basis, for example

$$\langle c_i^\dagger c_{i+r} \rangle = \left\langle \tilde{c}_i^\dagger \left( \prod_{k=i+1}^{i+r-1} z_k \right) \tilde{c}_{i+r} \right\rangle. \quad (4.1)$$

Of course these signs occur also in the old basis, but in the Jordan-Wigner transformed basis they are seen most explicitly.

To obtain 'reduced' correlations, it is convenient to subtract the product of the expectation values of the two clusters, i.e. for two operators  $O_1$  and  $O_2$ , acting on one or the other cluster, one obtains the 'reduced' correlator

$$\langle O_1 O_2 \rangle - \langle O_1 \rangle \langle O_2 \rangle , \quad (4.2)$$

describing the correlations. For most cases the latter part will be zero, due to an unequal number of creation and annihilation operators in  $O_1$  and  $O_2$ . In the following only the 'reduced' correlation functions are considered.

The correlation function  $C_{\text{CDW}}(i, r) = \langle n_i n_{i+r} \rangle - \langle n_i \rangle \langle n_{i+r} \rangle$  may be identified with a charge density wave (CDW), because it reproduces the oscillating behaviour of occupancy of the charge density wave.

The correlation function  $C_{\text{FL}}(i, r) = \langle c_i^\dagger c_{i+r} \rangle$  may be associated with Fermi liquid behaviour (FL). This correlation function determines whether the system is conducting or not. A vanishing correlation function reveals an isolator and a large value indicates good conductance.

Similarly, the correlation function  $C_{\text{SC}}(i, r) = \langle c_i^\dagger c_{i+1}^\dagger c_{i+r} c_{i+r+1} \rangle$  shows whether the transport of pairs of fermions is possible or not. Thus it is associated with superconducting behaviour (SC).

What one can see from these correlation functions, is that all operators of a correlation function belong to the same, clearly distinguishable symmetry class. The easiest symmetry classes one can think of is to sort correlation functions by the change in the fermion number  $\Delta F$  in each cluster. The CDW correlation function conserves the fermion number,  $\Delta F = 0$ , the FL correlation function changes the fermion number by one in each cluster (of course totally particle conservation is fulfilled),  $\Delta F = 1$ , and the SC correlation function changes the fermion number by two,  $\Delta F = 2$ .

## 4.2 Correlation density matrix

When trying to characterize the properties of a given ground state in terms of the behaviour of its correlation function, one encounters the problem, that one has to guess in advance which one could have a contribution or not. Thus one might miss a type of correlation that is uncommon or new. A concept to determine the dominant correlations in an unbiased fashion without prior knowledge is the *correlation density matrix (CDM)* [1], defined as follows:

$$\rho^C \equiv \rho^{AB} - \rho^A \otimes \rho^B . \quad (4.3)$$

$A$  and  $B$  are two clusters,  $\rho^{AB}$  is the reduced density matrix of the combined clusters and  $\rho^A$  and  $\rho^B$  are the reduced density matrices of the single clusters. This definition is motivated by Eq. (4.2) and the general connection between density matrices  $\rho$  and expectation values of operators  $O$ :

$$\langle O \rangle = \text{Tr}(\rho O) . \quad (4.4)$$

For two operators  $O_A$  and  $O_B$  acting on the clusters  $A$  and  $B$ , respectively, the correlation function reads as

$$\begin{aligned}
\langle O_A O_B \rangle - \langle O_A \rangle \langle O_B \rangle &= \text{Tr}(\rho^{AB} O_A O_B) - \text{Tr}(\rho^A O_A) \text{Tr}(\rho^B O_B) \\
&= \text{Tr}(\rho^{AB} (O_A \otimes O_B) - (\rho^A \otimes \rho^B) (O_A \otimes O_B)) \\
&= \text{Tr}(\rho^C (O_A \otimes O_B)) .
\end{aligned} \tag{4.5}$$

Thus the correlation density matrix Eq. (4.3) contains all possible inter-cluster correlations, both classical and quantum correlations [1]. If there were no correlations, the correlation density matrix vanishes, because then  $\rho^{AB} = \rho^A \otimes \rho^B$ ! This has to be considered carefully. The Heisenberg chain as a product state yields a vanishing correlation density matrix! But one cannot say that two parts of the Heisenberg chain have nothing to do with each other as one knows *exactly* the spin of all other sites, if one knows the spin of one site. Nevertheless, there are no correlations in the sense, that an operation on one site, for example a measurement, would affect other sites.

It is convenient to define the size of the clusters  $A$  and  $B$  to be the same, which will be assumed for the rest of this thesis. Then there exists an upper bound for the correlation density matrix [1]:

$$\|\rho^C\|^2 \leq 1 - \frac{1}{d_c^2}, \tag{4.6}$$

where  $d_c$  is the dimension of the reduced Hilbert spaces  $\mathcal{H}^A$  and  $\mathcal{H}^B$  of cluster  $A$  and  $B$ , respectively. To study the long range behaviour of the system one may calculate a series of correlation density matrices, where the two clusters depart more and more from each other. Thus one obtains the correlation density matrix as a function of distance  $r$  and has something comparable to the correlation functions, but with the great advantage that all possible correlations are included!

The correlation density matrix itself does not reveal the properties of the system as directly as the correlation functions do (see Sec. 4.1). To study the various parts of the correlation density matrix, we apply a singular value decomposition (see App. A.3) [1]. Consider two clusters  $A$  and  $B$ , whose Hilbert spaces  $\mathcal{H}^A$  and  $\mathcal{H}^B$  have dimension  $d_c$  respectively. The correlation density matrix of these two clusters reads as

$$\rho^C = (\rho^C)_{a'ab'b}, \tag{4.7}$$

where the indices  $a, a'$  belong to the Hilbert space  $\mathcal{H}^A$  and the indices  $b, b'$  belong to the Hilbert space  $\mathcal{H}^B$ . On both Hilbert spaces, we use the Frobenius norm and inner product:

$$\|O\|_F^2 = \sum_{i,j} |O_{ij}|^2 = \text{Tr}(O^\dagger O), \tag{4.8}$$

$$\langle O_1, O_2 \rangle_F = \sum_{i,j} (O_1^*)_{ij} (O_2)_{ij} = \text{Tr}(O_1^\dagger O_2). \tag{4.9}$$

After fusing the indices  $(a'a)$  and  $(b'b)$  one may apply the singular value decomposition and *unfuse* the indices again:

$$\rho^C = (\rho^C)_{a'ab'b} = \sum_{\alpha} w^{[\alpha]} \left( O_A^{[\alpha]} \right)_{a'a} \otimes \left( O_B^{[\alpha]} \right)_{b'b} , \quad (4.10)$$

where  $w^{[\alpha]}$  are the singular values and  $O_A^{[\alpha]}$  and  $O_B^{[\alpha]}$  the corresponding operators acting on cluster  $A$  and  $B$  respectively. By definition, all operators have norm one with respect to the Frobenius norm, and the singular values  $w^{[\alpha]}$  are positive. Thus the norm of  $\rho^C$  is simply

$$\rho^C = \sum_{\alpha} (w^{[\alpha]})^2 . \quad (4.11)$$

The technicality of fermionic signs, see Eq. (4.1), of course also occurs here and thus one has to calculate two correlation density matrices: one where the  $z$ -operators from the Jordan-Wigner transformation are considered and one where they do not occur. From the one with  $z$ -operators only correlations with an odd number of fermionic creation and annihilation operators may be extracted and from the other one only those with an even number of fermionic creation and annihilation operators.

The operators  $O_A^{[\alpha]}$  and  $O_B^{[\alpha]}$  are classified as follows, according to the three symmetry classes introduced in Sec. 4.1. Consider the projection operators  $E_{k,l}$  for both Hilbert spaces  $\mathcal{H}^A$  and  $\mathcal{H}^B$ , respectively:

$$(E_{k,l})_{ij} = \begin{cases} 1 & \text{for } (i,j) = (k,l) \\ 0 & \text{else} \end{cases} , \quad (4.12)$$

where the indices  $i, j, k, l$  each run from 1 to  $d_c$ . They form a complete basis for both operator spaces. A symmetry class, expressed in this basis, is taken to be the set of all projectors that produce the same change  $\Delta F$  in particle number in the cluster:

$$S_i = \{E_{k,l} | \Delta F = |F_l - F_k| = i\} . \quad (4.13)$$

A given (normalized) operator  $O$  can be decomposed as

$$O = \sum_{k,l} E_{k,l} O_{k,l} , \quad (4.14)$$

where the weights are given by  $O_{k,l} = \text{Tr}(E_{k,l}O)$ . Thus the weight of operator  $O$  in symmetry class  $S_i$  is defined as

$$w_i(O) = \sum_{E_{k,l} \in S_i} |O_{kl}|^2 , \quad (4.15)$$

where these weights add up to one when summed over all symmetry classes, due to the operators being normalized:  $\sum_i w_i(O) = 1$ . To get a measure for the contribution of a given

symmetry class to the complete correlation density matrix, the squares of the weights of all singular values  $w^{[\alpha]}$  are added up:

$$W_{ij}^{AB} = \sum_{\alpha} (w^{[\alpha]})^2 w_i \left( O_A^{[\alpha]} \right) w_j \left( O_B^{[\alpha]} \right) = \delta_{ij} W_i^{AB}. \quad (4.16)$$

The last equality expresses the fact, that it is not possible for terms of the singular value decomposition to mix symmetry classes, i.e. for a given  $\alpha$ ,  $O_A^{[\alpha]}$  and  $O_B^{[\alpha]}$  have to be in the same symmetry class, else particle conservation would be violated.

These weights add up to the sum of the squares of all the singular values  $w^{[\alpha]}$ , which makes them comparable to the upper bound Eq. (4.6) of the correlation density matrix:

$$W^{AB} = \sum_i W_i^{AB} = \sum_{\alpha} (w^{[\alpha]})^2 = \|\rho^C\|_F^2 \leq 1 - \frac{1}{d_c^2}. \quad (4.17)$$



# Chapter 5

## Results

In this chapter we present our results, obtained by the techniques introduced in the preceding chapters. To have an idea of the reliability of the methods, the parameters of the Hamiltonian have been chosen such, that we could compare the results of both methods with the analytical results of Sec. 1.2. Unfortunately, the infinite time evolving block decimation turned out to be not very reliable. Thus we decided to concentrate on the results obtained with the variational matrix product state method. Then, we calculated the ground state for various parameter values and checked on the reliability of these results in terms of numerical criteria. Before we investigated the correlation density matrix, the three limiting cases of Sec. 1.3 were compared with the analytical solution.

Within this realization of the variational matrix product state method we fix a certain particle filling by choosing a certain chemical potential (otherwise one would have to include Abelian symmetries), and thus all calculations refer to the grand canonical ground state. The Fermi energy has been set to zero for simplicity.

### 5.1 Consistency check for the noninteracting case

Without electron-electron interaction the results from the numerical methods can be compared directly with the analytical solutions of Sec. 1.2 without any further mapping.

#### 5.1.1 Infinite time evolving block decimation

A description of this method was given in Sec. 3.3. In practice the values for  $\tau$  are changed dynamically within the calculation. We tried two approaches, starting with  $\tau = 1$  and decreasing it to  $\tau \approx 10^{-7}$ , which corresponds to a Suzuki-Trotter error, see Eq. (3.9), of about  $10^{-6}$ .

In the first approach  $\tau$  was decreased in  $N_\tau$  equal steps, where the imaginary time evolution for each  $\tau_n$  was repeated  $K$  times. It turned out that  $K$  could be chosen rather small (typically  $K \lesssim 10$ ), because the action of the imaginary time evolution converged to a fixed value very fast. Based on this, we tried to study the influence of the choice of  $N_\tau$  and  $K$

by fixing the product  $N_\tau K = \text{const}$ . We expected to obtain higher accuracy for results with large  $N_\tau$ , but  $K$  still large enough that the action of the imaginary time evolution converged. But this was not the case; even worse, the influence of the values of  $N_\tau$  and  $K$  was rather irregular. The relative error, both in ground state energy and particle filling, compared to the analytical results was always about  $10^{-2}$ , which was disappointingly high.

The second approach modified this scheme to an exponential decrease of the  $\tau$ -values. Starting with the first  $\tau$  the imaginary time evolution is applied  $K$  times and then changed to a smaller value, determined by

$$\tau_n = 2^{-\sqrt{n}}, \quad (5.1)$$

where  $n = 0$  corresponds to the first  $\tau$ . This scheme emphasizes the smaller values of  $\tau$  more than the greater ones, in contrast to the previous scheme. The exact choice of the exponent may be varied for best results. Nevertheless, the results were as irregular as before and the relative error in ground state energy and particle filling again about  $10^{-2}$ .

The irregular  $\tau$ -dependence, combined with the fact that the Hilbert space truncation involves a few uncontrolled approximations, led us to the conclusion that the infinite time evolving block decimation requires several improvements, which are beyond the scope of this thesis. Thus this method has not been investigated further, especially as the correlation functions could not be reproduced faithfully.

### 5.1.2 Variational matrix product state method

We have implemented this method as described in Chap. 2. The results obtained by this method have been compared with both the analytical results for finite chains as well as the analytical result for infinite chains. To check on the influence of the chain length, ground state energy and filling have been analyzed for various chain lengths.

#### Zero inter-leg hopping

The parameters of the Hamiltonian in Eq. (1.5) have been chosen such that it may be compared with a single tight binding chain, i.e. the inter-leg hopping is zero,  $t_\perp = 0$ , as well as the electron-electron interaction terms,  $t_c = 0$  and  $V = 0$ . The only remaining Hamiltonian term is  $t_\parallel = 1$ . The ground state energy per unit cell and the filling are shown in Figs. 5.1 and 5.2 as functions of the chain length  $N$ .

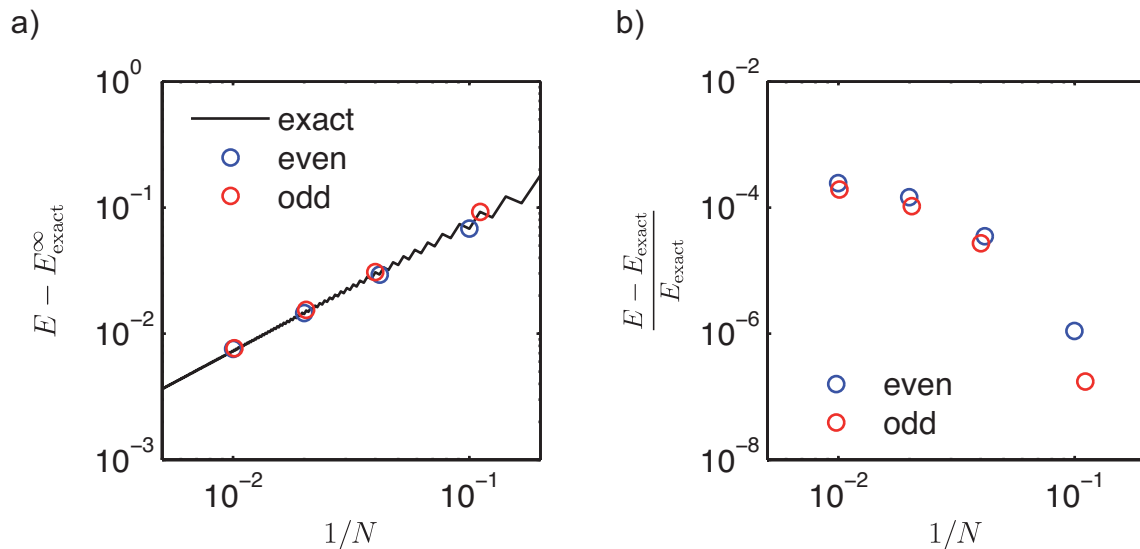


Figure 5.1: Ground state energy per unit cell  $E$  and the corresponding error for several chain lengths. The black curve shows the exact result for finite chains. The numerical results are divided into even (blue) and odd (red) chain lengths. a) The ground state energy per unit cell of the infinite chain  $E_{\text{exact}}^{\infty}$  is used as reference energy to see how good the finite chain simulates the infinite system. The x-axis shows the inverse chain length  $\frac{1}{N}$ , which can be extrapolated to  $N \rightarrow \infty$ , i.e.  $\frac{1}{N} \rightarrow 0$ . b) The relative error of the DMRG results with respect to the exact result for finite chain length  $E_{\text{exact}}$ .

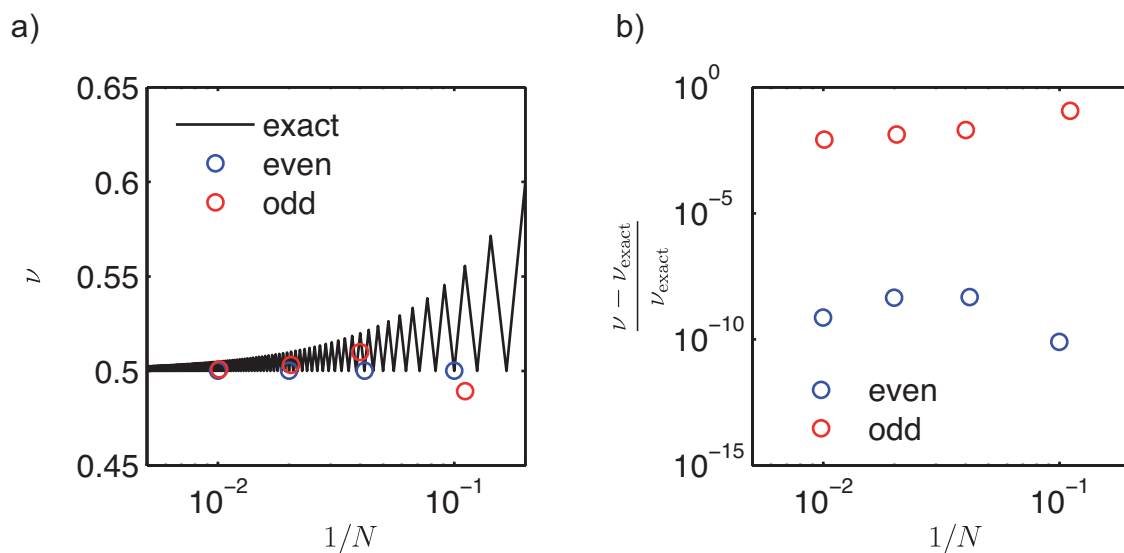


Figure 5.2: Ground state filling  $\nu$  and the corresponding error for several chain lengths. The black curve shows the exact result for finite chains. The numerical results are divided into even (blue) and odd (red) chain lengths. a) Chain filling. b) Relative error, where  $\nu_{\text{exact}}$  is the filling of the exact result for finite chain length.

One can clearly see that the results for the filling are less accurate for odd chain lengths, because the ground state is degenerate in this case. This does not appear to make a significant difference for the energy, however. Because of the good agreement between analytical and numerical results and good convergence with respect to numerical criteria, we calculated the correlation functions as introduced in Sec. 1.2.1. The results are shown in Fig. 5.3.

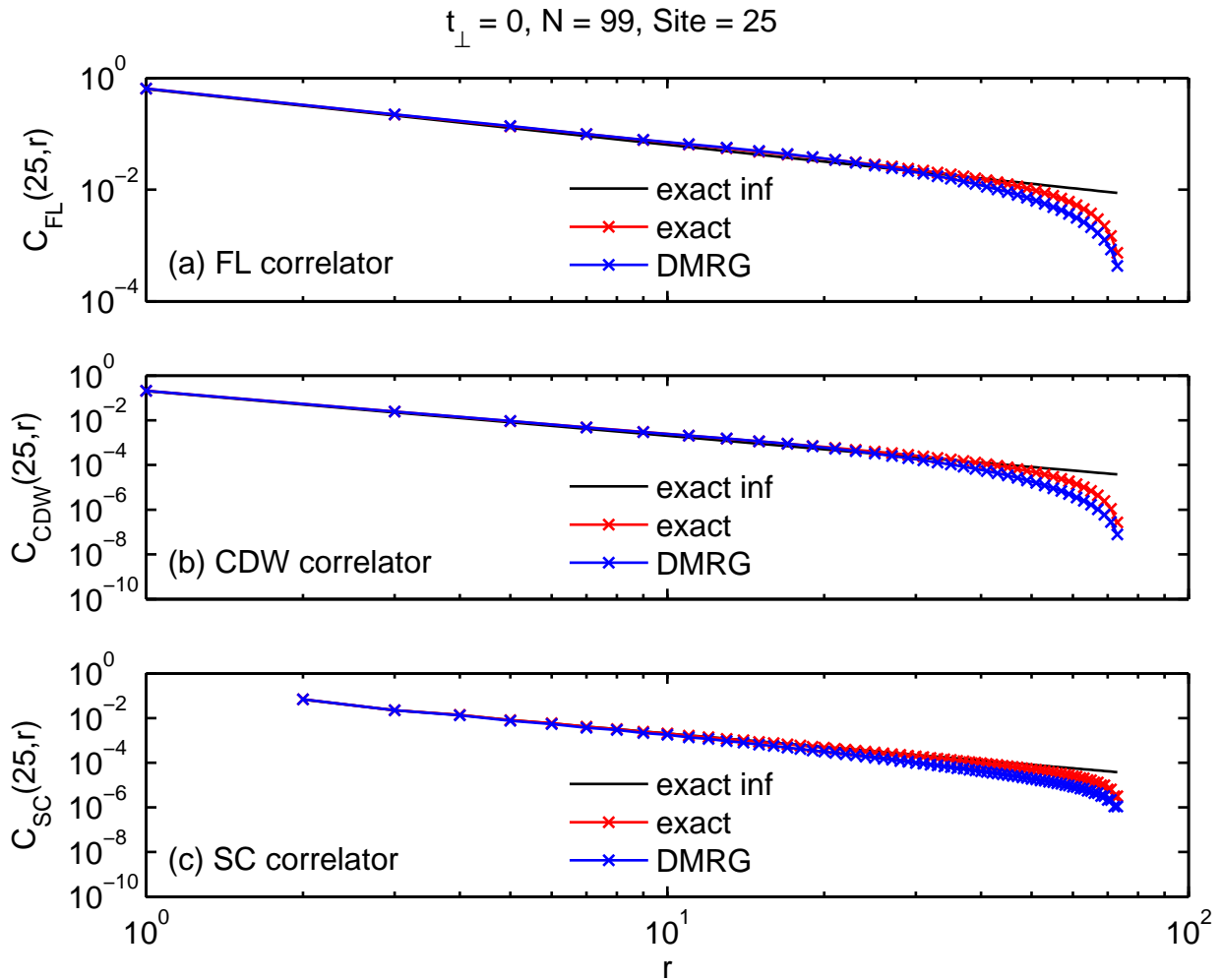


Figure 5.3: Correlation functions as introduced in Sec. 1.2.1 for chain length  $N = 99$  calculated relative to site 25. All correlation functions are plotted versus the distance  $r$ . a) The FL correlation function. Only odd distances are plotted because the even ones are zero in the exact case. b) The CDW correlation function. Again only odd distances are plotted. c) The SC correlation function. For all three cases the error for the values that are zero in the exact case is about  $10^{-4}$  and the relative error for the non-zero values is about  $10^{-2}$  up to distances of 20.

To get an estimate on the accuracy of the correlation density matrix, it has been calculated similarly with cluster  $A$  fixed at the same site as the correlation functions in Fig. 5.3 (site 25) and with cluster  $B$  moved to the right to vary the distance. To include not only the CDW and FL correlations, but also the SC correlations, the size of the clusters were chosen

as two neighbouring rungs on the ladder. We assigned the weights of the singular value decomposition of these correlation density matrices to the symmetry classes as introduced in Sec. 4.2. The result is plotted in Fig. 5.4 together with the correlation functions for the exact result of the infinite chain for comparison. To obtain a curve which lies close to the fitting curve, these correlation functions were squared and adjusted, by a factor of  $\frac{1}{8}$ , for the following reasons. First, as we sum over the square of the weights, the correlation functions had to be squared, too. Also, the operators involved in these correlation functions ( $c, n, \dots$ ) are not normalized in the sense of the singular value decomposition in Eq. (4.10), thus one has to divide through this norm. On the other hand, the chosen correlation functions are each only one of several similar correlation functions within a given block configuration  $A$  and  $B$ . Thus for a correlation function  $C$ , based on operators which have norm  $N$  in each cluster and for which  $n$  similar correlation functions exist, we plot

$$C' = \frac{1}{N^2} n C^2 . \quad (5.2)$$

For example in the case of the FL correlation with two clusters of size 2, there are 8 possibilities for a particle to move from cluster  $A$  to cluster  $B$  for vanishing inter-leg hopping, and the corresponding operators, e.g.  $c_{\uparrow i} \otimes \mathbb{1}_{\downarrow i} \otimes \mathbb{1}_{\uparrow i+1} \otimes \mathbb{1}_{\downarrow i+1}$ , which acts on one cluster in this case, have Frobenius norm  $N = 8$ . The resulting factor is  $\frac{1}{8}$ , as well as for the CDW and SC correlations.

We applied a polynomial fit on the DMRG results to obtain the exponent of the power law, but not over the full range of  $r$ , only for the part away from the open boundary where the fluctuations are not too strong as indicated by the grey region in Fig. 5.4.

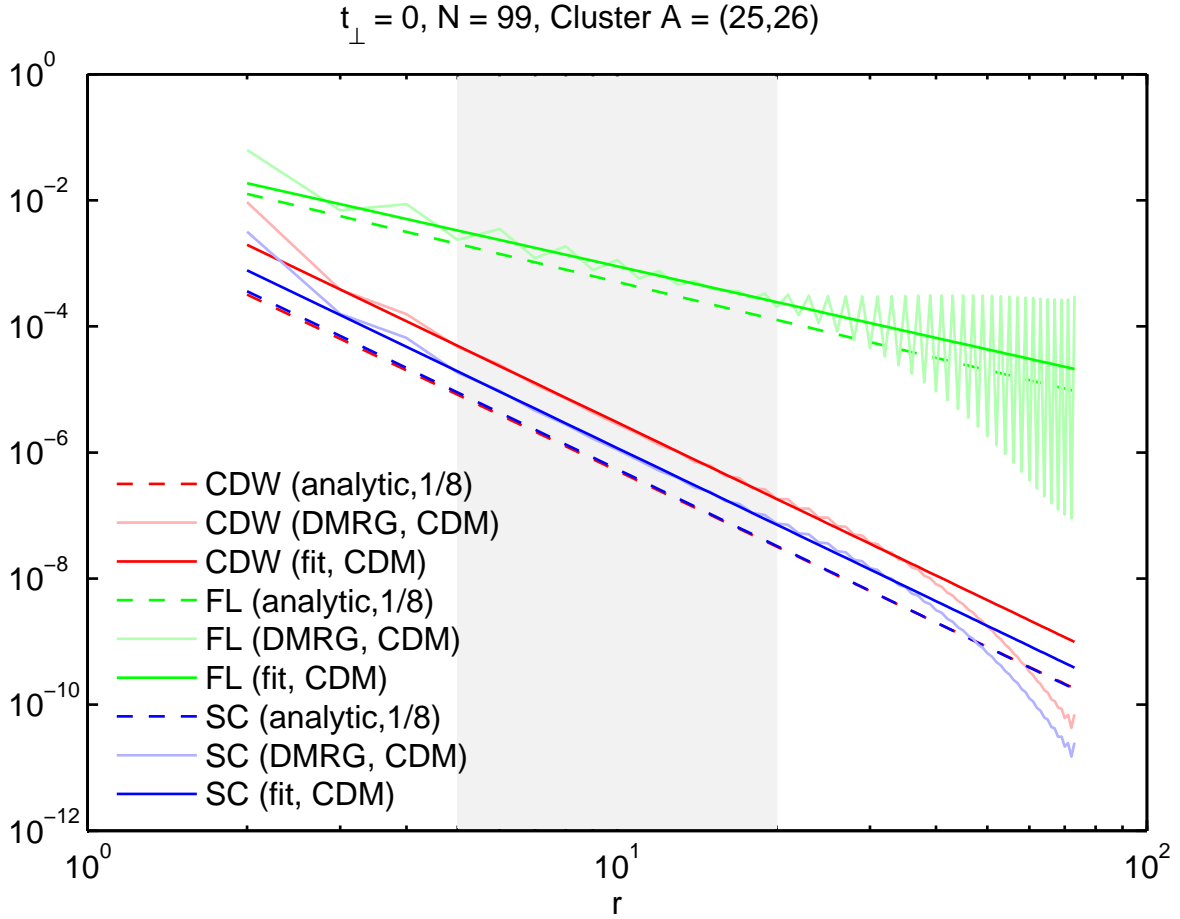


Figure 5.4: The symmetry ordered weights of the correlation density matrices as a function of distance. Cluster  $A$  is fixed on the sites  $(25, 26)$  and cluster  $B$  separated from it by  $r$  sites, starting from sites  $(27, 28)$  on to the right. The light, solid curves show the weights of the CDM, the dark, solid curves the polynomial fit and the dashed curves the analytical correlation function for the infinite chain. The polynomial fits  $cr^{-2\alpha}$  (the factor of two in the exponent accounts for the singular values being squared) yield the following critical exponents:  $\alpha(\text{CDW}) = 2.02$ ,  $\alpha(\text{FL}) = 0.94$  and  $\alpha(\text{SC}) = 2.02$ , which is in acceptable agreement with the exact results, namely  $\alpha_{\text{exact}}(\text{CDW}) = 2$ ,  $\alpha_{\text{exact}}(\text{FL}) = 1$  and  $\alpha_{\text{exact}}(\text{SC}) = 2$  as can be seen in Sec. 1.2. Even and odd distances have been fitted separately and the middle of these two fits is used. The range of  $r$ -values that was used for the fitting has been shaded grey.

### Finite inter-leg hopping

The same comparisons as for the zero inter-leg hopping are applied in the case of finite inter-leg hopping (with  $t_{\perp} = 1$  for simplicity). Again the ground state energy per unit cell and the filling are plotted as a function of chain length  $N$  (see Figs. 5.5 and 5.6).

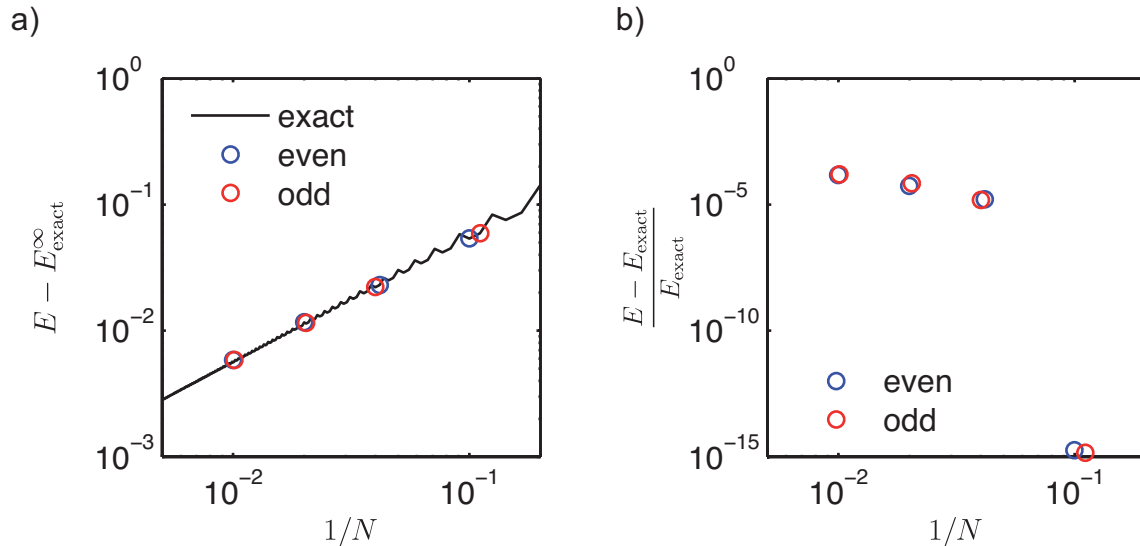


Figure 5.5: Ground state energy and the corresponding error for several chain lengths for  $t_{\perp} = 1$ , otherwise as plotted in Fig. 5.1. For more information see the caption of that figure.

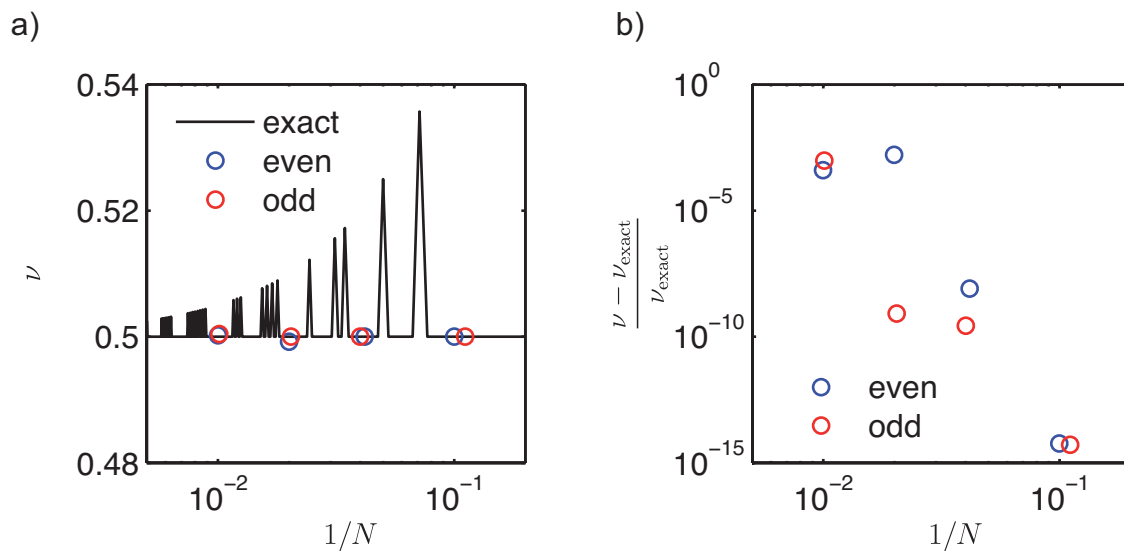


Figure 5.6: Ground state filling and the corresponding error for several chain lengths, otherwise as plotted in Fig. 5.2. For more information see the caption of that figure.

In this case there is no difference in accuracy between even and odd chain lengths, because the ground state is typically not degenerate for the calculated chain lengths. The agreement between analytical and numerical results is good and the numerical calculations are sufficiently converged. The resulting correlation functions are plotted in Fig. 5.7, as well as the results derived from the correlation density matrix similar to the zero inter-leg hopping case (see Fig. 5.8).

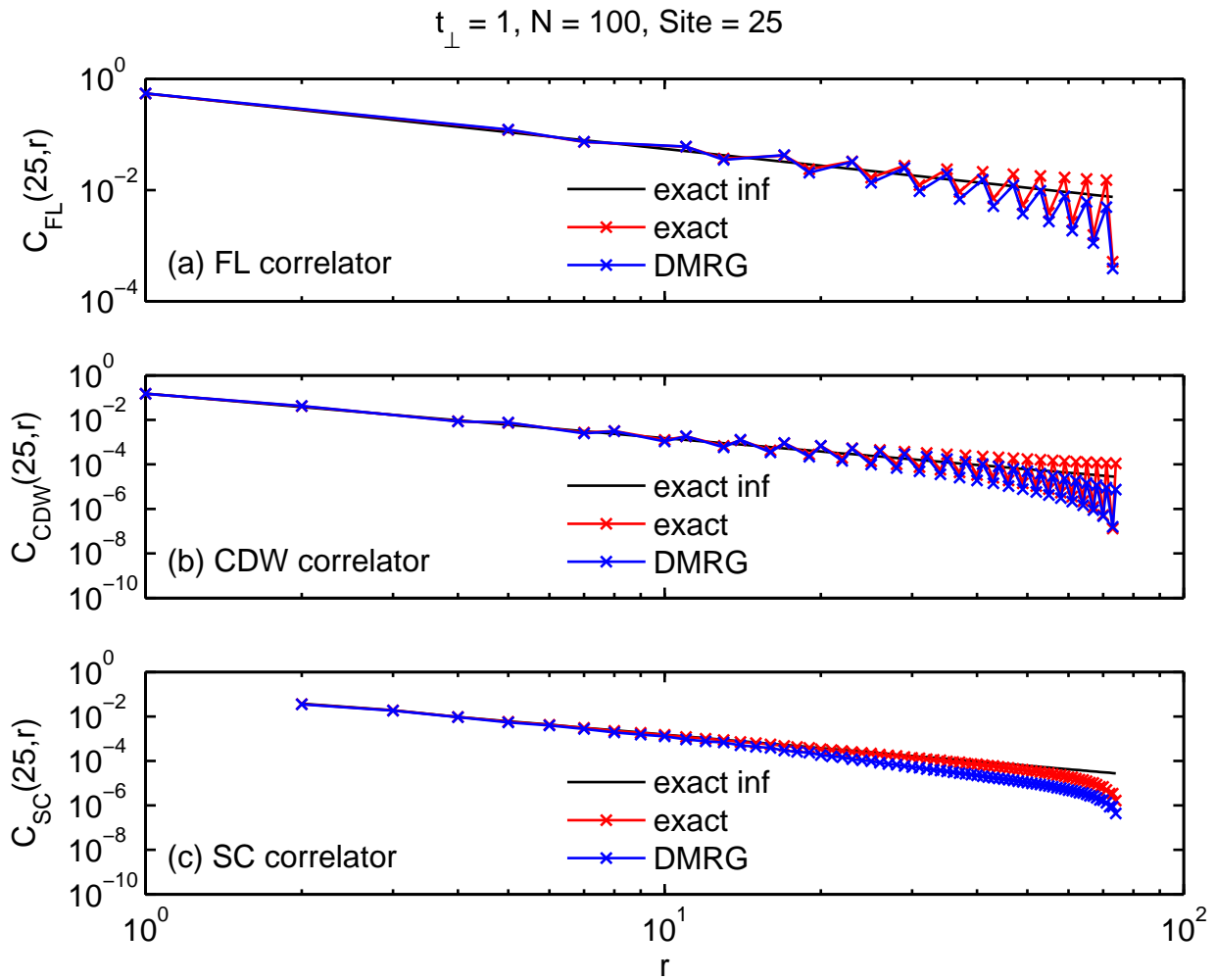


Figure 5.7: The three correlation functions for a chain with length  $N = 100$ , with reference to site 25: a) FL, but only values that are non-zero in the exact result are plotted. b) CDW, again with only non-zero values of the exact case plotted. c) SC. See Fig. 5.3 for a detailed explanation. The errors are within the same range as for the zero inter-leg hopping.

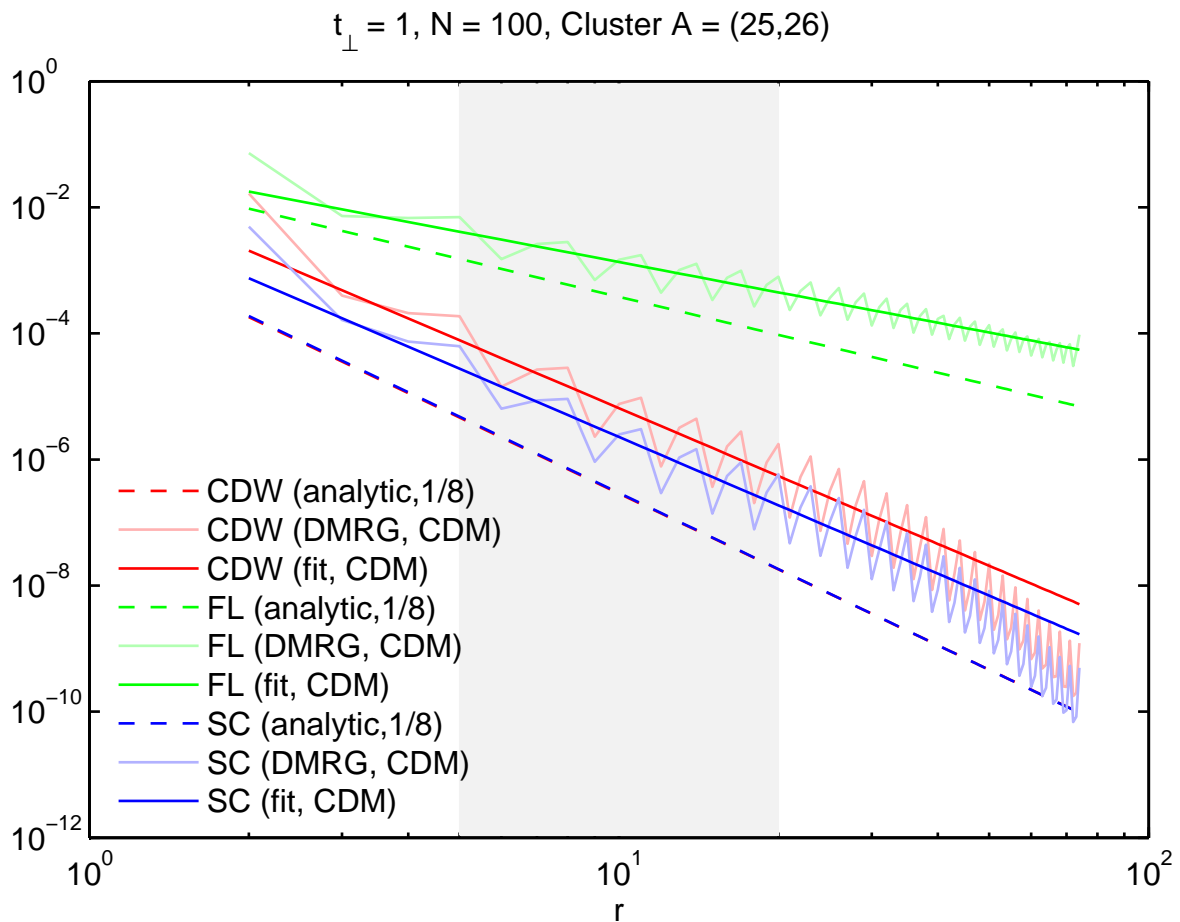


Figure 5.8: The symmetry ordered weights of the correlation density matrices as a function of distance. Cluster  $A$  is fixed on the sites  $(25, 26)$  and cluster  $B$  moves from sites  $(27, 28)$  to the right. See Fig. 5.4 for a detailed explanation. The fitted critical exponents  $\alpha$  as in  $cr^{-2\alpha}$  are:  $\alpha(\text{CDW}) = 1.79$ ,  $\alpha(\text{FL}) = 0.80$  and  $\alpha(\text{SC}) = 1.80$ , which is not in good agreement with the exact results  $\alpha_{\text{exact}}(\text{CDW}) = 2$ ,  $\alpha_{\text{exact}}(\text{FL}) = 1$  and  $\alpha_{\text{exact}}(\text{SC}) = 2$ , but gives the correct tendency and the correct dominant correlation.

### Outlook on the results with electron-electron interaction

The results of both cases are good enough that we expected meaningful results for the Hamiltonian as in Eq. (1.5). For the cases which are described in Sec. 1.3, we want to reproduce the results. At least a tendency of the correlation functions or of the correlation density matrix may be extracted from the numerical simulations.

## 5.2 Numerical checks on the DMRG results

For the rest of the thesis we investigate the interacting case, i.e. including infinite nearest neighbour repulsion and correlated hopping. Before we investigated any correlation func-

tions, several checks on the numerical results had to be done. We calculated the ground state for  $t_{\perp}$  and  $t_c$  taking the values 0,  $10^{-2}$ ,  $10^{-1}$ , 1,  $10^1$  and  $10^2$  for chain lengths  $N = 99$  and  $N = 100$  with a cutoff dimension of  $D = 64$ . The infinite nearest neighbour repulsion was simulated by  $V = 10^4$ . These are the calculations, where all results in the next sections come from. First of all we checked on the numerical convergence of the results, using the criterion given by Eq. (2.34), see Fig. 5.9.

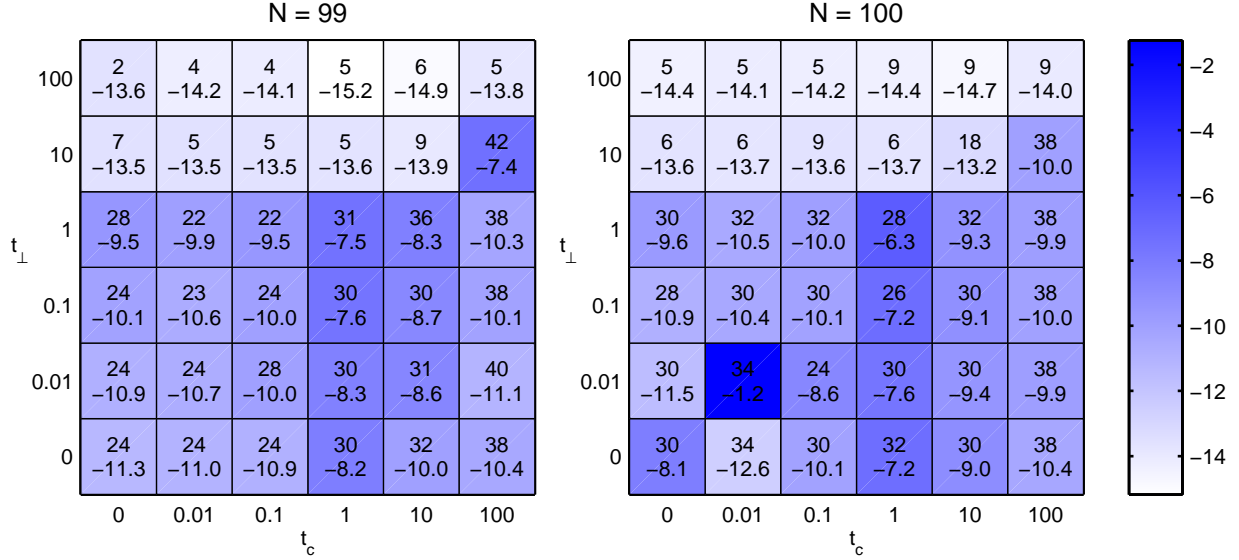


Figure 5.9: The number of sweeps (upper number) with dimension  $D = 64$  and the grade of convergence with respect to Eq. (2.34) (lower number, not  $\varepsilon$  is plotted, but  $\log_{10}(\varepsilon)$ ) for all calculated ground states. The colouring scheme is determined by the grade of convergence, where white denotes good convergence and blue bad convergence. The result for  $N = 100$ ,  $t_{\perp} = 0.01$  and  $t_c = 0.01$  is converged very bad despite of many sweeps. After a closer investigation, we found that it had been stuck in a local minimum for about 30 sweeps, because in that sweep the energy dropped drastically over a few site optimizations and started to converge again afterwards.

This is a first clue on the complexity of the system for different parameter values. A more difficult description of the complexity of the system gives the bond entropy, introduced in Sec. 2.1.4. In principle we applied the two-site Hilbert space truncation scheme to obtain the bond entropy, but without changing the state. Starting with the contraction and decomposition of sites one and two, then going on to the sites two and three and so on, we obtained the bond entropy for the whole chain (see Fig. 5.10). We investigated not  $S$ , but rather  $e^S$ , which has two interesting features. If it is one, the bond entropy is zero and thus the state is a product state with no entanglement at all. Second, its upper bound is the cutoff dimension  $D$  (easily shown for a  $D \times D$  density matrix with equal weights, which corresponds to the density matrix with the greatest entropy). Moreover we could check on the ratio of the largest ( $s_1$ ) to the smallest ( $s_D$ ) singular value, which was not discarded (see Fig. 5.11):  $\frac{s_D}{s_1}$ . The smaller this ratio, the smaller the part of the reduced density matrix that is discarded and thus the error made in the Hilbert space truncation is smaller.

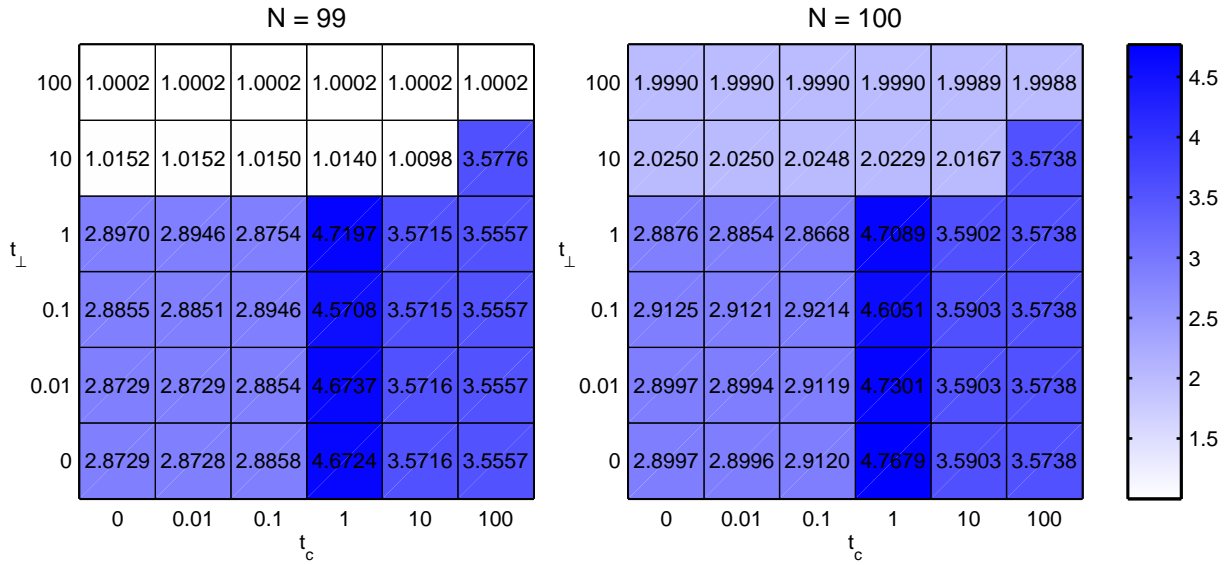


Figure 5.10: The maximal bond entropy  $e^S$  along the chain for all calculated ground states. We calculated the bond entropy for all bonds of the chain and took the largest value for each chain for this plot.

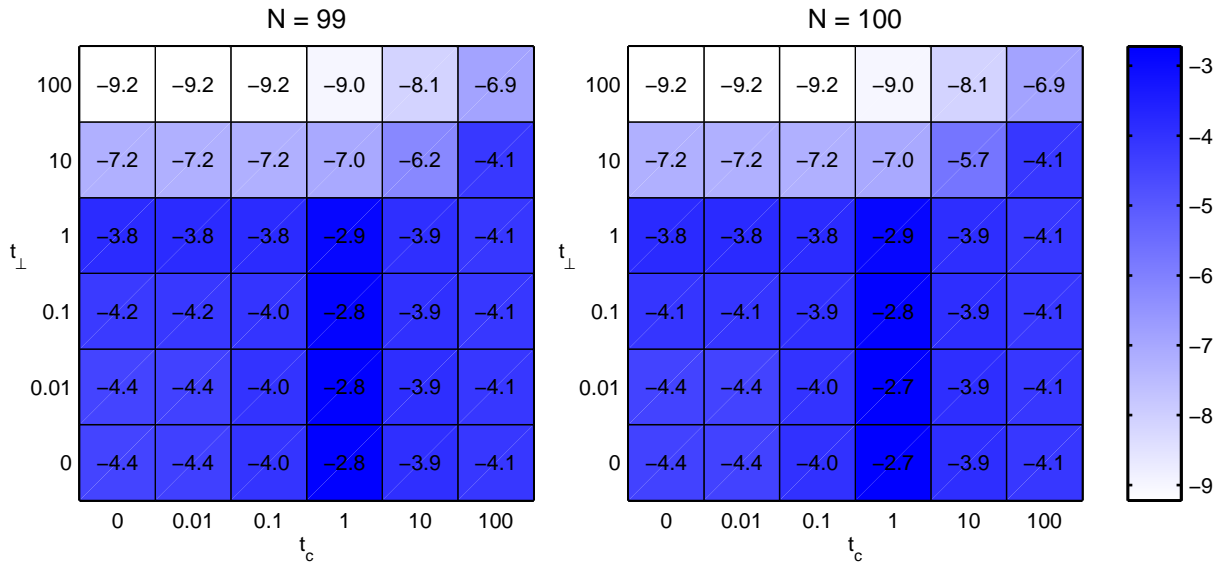


Figure 5.11: The ratio of the largest singular value to the smallest  $\frac{s_D}{s_1}$  along the chain. From the calculation of the bond entropy we had a singular value spectrum for each bond and calculated the ratio of the first (largest) singular value to the  $D$ th (smallest kept) singular value. The maximal ratio for each chain is plotted.

A remarkable feature of the maximal bond entropy is the discrepancy between the results for  $N = 99$  and  $N = 100$  for large values of  $t_\perp$ . The maximal bond entropy for the  $N = 100$

results is nearly twice the value of the  $N = 99$  results (see Fig. 5.10), but the ratio of the singular values is nearly the same (see Fig. 5.11). Thus we had a closer look on these parameter values. Choosing a bond in the middle of the chain, we compared the complete singular value spectrum of the two chain lengths. It turned out that for the chain with length  $N = 100$  each singular value has a second singular value with nearly the same value (see Fig. 5.12). This indicates degeneracy of the ground state which is reasonable because for dominating inter-leg hopping one expects fermions which are delocalized over one rung with every second rung occupied due to the infinite nearest neighbour repulsion (see Sec. 1.3). For a chain length of  $N = 100$  (or more generally for even chain lengths) this is accomplished by two states, one where all even rungs are occupied and one where all odd rungs are occupied. This is not the case for the chain with length  $N = 99$  (odd chain lengths).

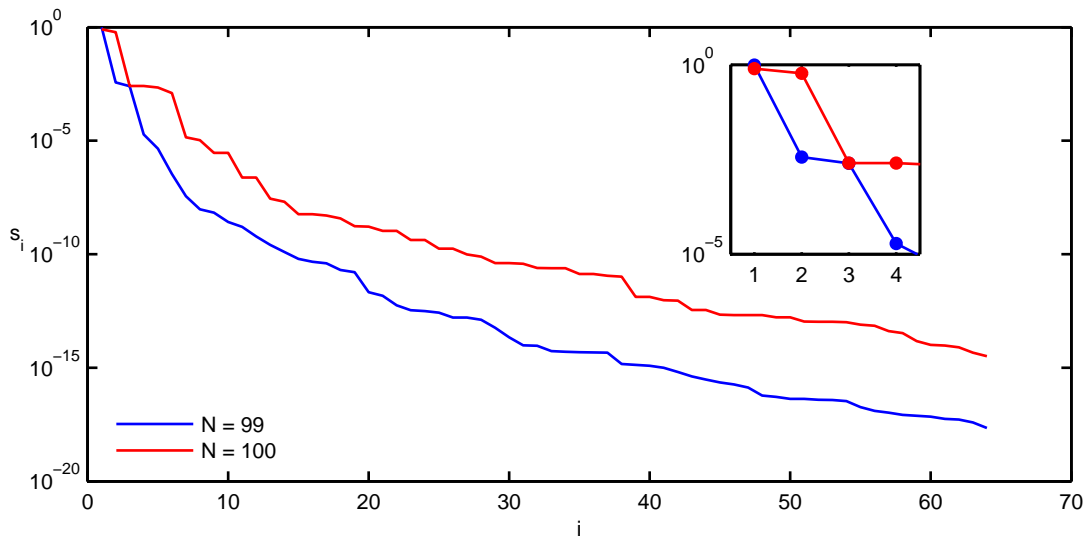


Figure 5.12: The complete singular value spectrum of the bond between site 50 and site 51 for a chain length of  $N = 99$  (blue) and  $N = 100$  (red). There are  $D = 64$  singular values plotted. The remaining singular values (in total there are  $dD$ ) are zero by construction of variational single site DMRG.

The preceding checks are concerning the numerical method and give a hint on the accuracy we can expect. A concrete physical condition is the demand that the total particle number has to be an integer number. A deviation of the total particle number from an integer number gives a direct estimate on the error of our method, see Fig. 5.13.

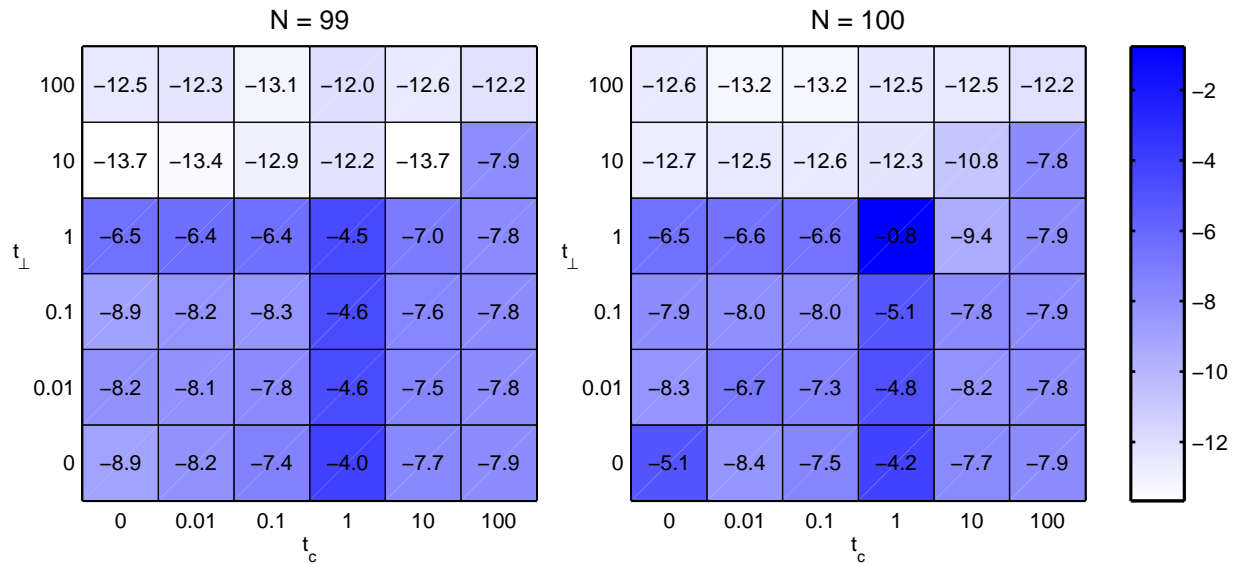


Figure 5.13: The deviation of the total particle number  $N_{\text{tot}}$  from an integer number for all calculated results:  $\Delta N_{\text{tot}} = |N_{\text{tot}} - \text{round}(N_{\text{tot}})|$ , but the plot shows  $\log_{10}(\Delta N_{\text{tot}})$ . One can clearly see that ground states with good numerical convergence have smaller values of  $\Delta N_{\text{tot}}$ .

Of course we cannot treat the preceding figures as a phase diagram, but they look similar to the phase diagram in Fig. 1.5. Something which may show the structure of the phase diagram is the filling of the sites  $\nu = \frac{N_{\text{tot}}}{2N}$  of the grand canonical ground state, see Fig. 5.14.

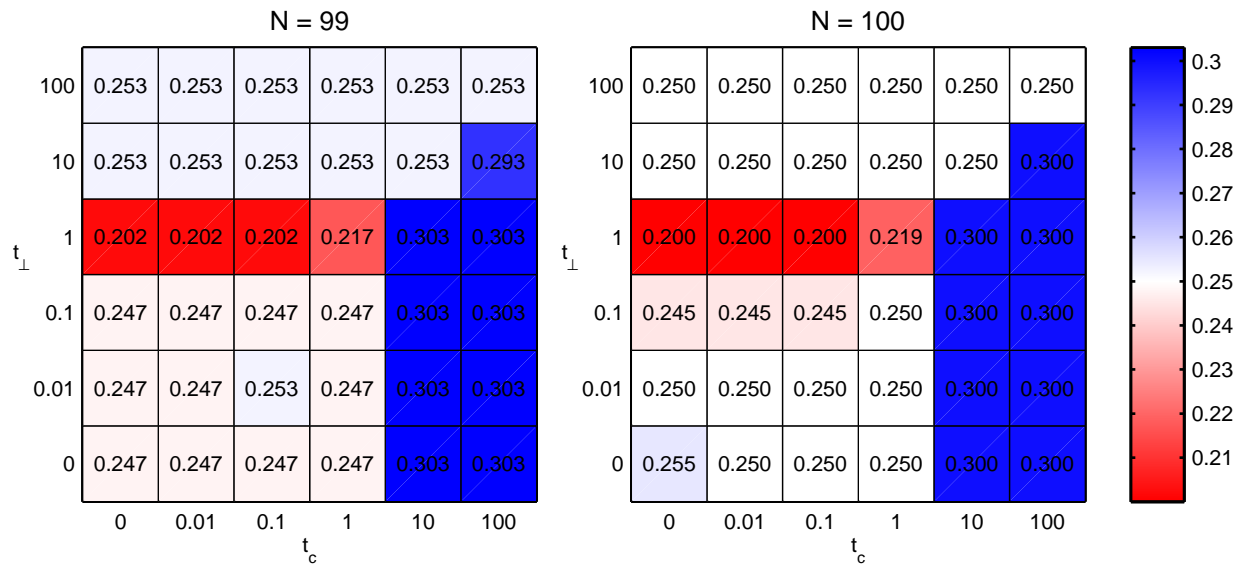


Figure 5.14: The ground state filling for all our calculations. The colouring scheme is chosen such that white corresponds to quarter filling.

## Reproduced features

All these diagrams mimic the structure of Fig. 1.5. Moreover, some of them reproduce the predictions made in [2] on the phase boundaries. The bond entropy in Fig. 5.10 shows a significant increase for  $t_c = 1$  and  $t_\perp \lesssim 1$ , which means that the bonds carry more information, i.e. the state is more complex. This indicates that there might be two competing states and thus a phase transition. The filling shows something similar, but for  $t_\perp = 1$  and  $t_c \lesssim 1$ . It clearly drops down compared to other values of  $t_\perp$  in the surrounding. There is no interpretation as for the bond entropy, one can only see that there is something different for these parameters.

## 5.3 Investigation of correlation functions and expectation values

The diagrams in Sec. 5.2 suggest, that we can reproduce the phase diagram in Fig. 1.5. Thus we investigated the limiting cases, which have been solved analytically in Sec. 1.3, to get a better impression of the numerical results in these cases. In each case we calculated the average occupancy for several sites in the middle of the chain, the FL correlation function  $C_{\text{FL}}(i', |i - i'|) = \langle c_{a,i}^\dagger c_{a',i'} \rangle$  and the CDW correlation function  $C_{\text{CDW}}(i', |i - i'|) = \langle n_{a,i} n_{a',i'} \rangle$ . To illustrate the expectation values, we depicted them by circles located on the sites of the ladder. The radius of the circles is proportional to the absolute value of the expectation value. In the case of the FL and CDW correlation functions site  $a', i'$  is indicated by a black circle, because it is fixed as starting site. The circle on the site  $a, i$  gives the value of the correlator. Further we calculated the bond entropy along the chain, as in Sec. 5.2. For some cases this exposes interesting features.

### (i) Strong correlated hops

The parameters are chosen as  $t_\perp = 0$  and  $t_c = 100$ . It is not easy to reproduce the structure of the ground state in this case with the expectation values introduced above, because it bases on the hard-core bosons introduced in Sec. 1.3.1. Nevertheless one can see several features which denote the hardcore bosons, see Fig. 5.15. The results for chain lengths of  $N = 99$  and  $N = 100$  are nearly the same and thus only one case is plotted.

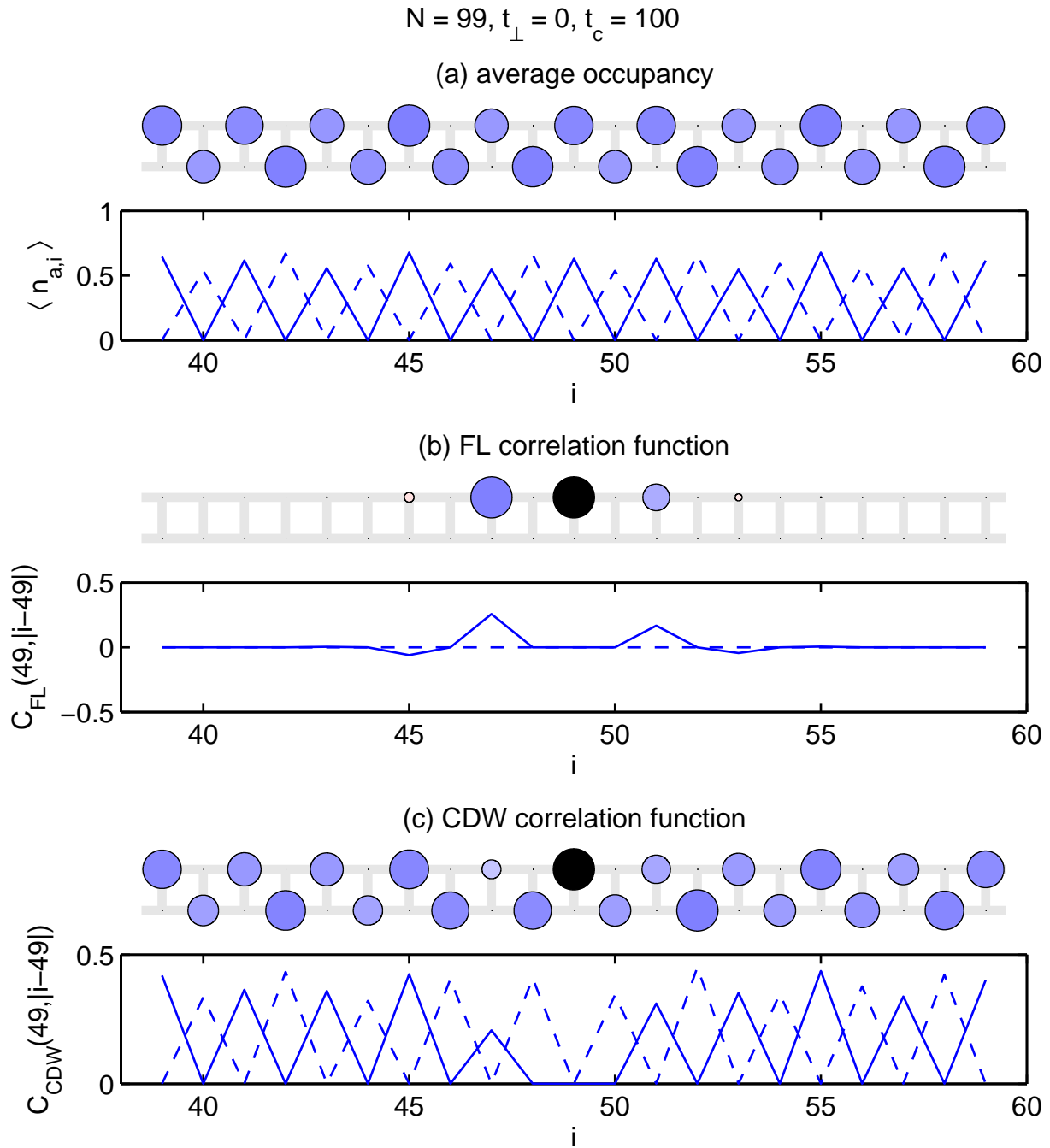


Figure 5.15: Average occupancy and correlation functions for a chain of length  $N = 99$  around rung 49 ( $V = 10^4, t = 1$ ). The solid lines correspond to the upper leg and the dashed lines correspond to the lower leg. a) The average occupancy. One can clearly see that one only has values distinct from zero which always allow for correlated hops and thus may form hardcore bosons. b) The correlation function  $C_{FL}(49, |i - 49|) = \langle c_{a,i}^\dagger c_{\uparrow,49} \rangle$ . The non-vanishing values for the upper sites of rungs 47 and 51 require an occupied site on the lower leg at rungs 48 and 50, respectively. c) The correlation function  $C_{CDW}(49, |i - 49|) = \langle n_{a,i} n_{\uparrow,49} \rangle$ . This correlation function yields no more information than the average occupancy.

The expectation values show expected behaviour and are in agreement with the analytical results. The bond entropy on the other hand has an unexpected regularity for which we don't have an explanation, see Fig. 5.16.

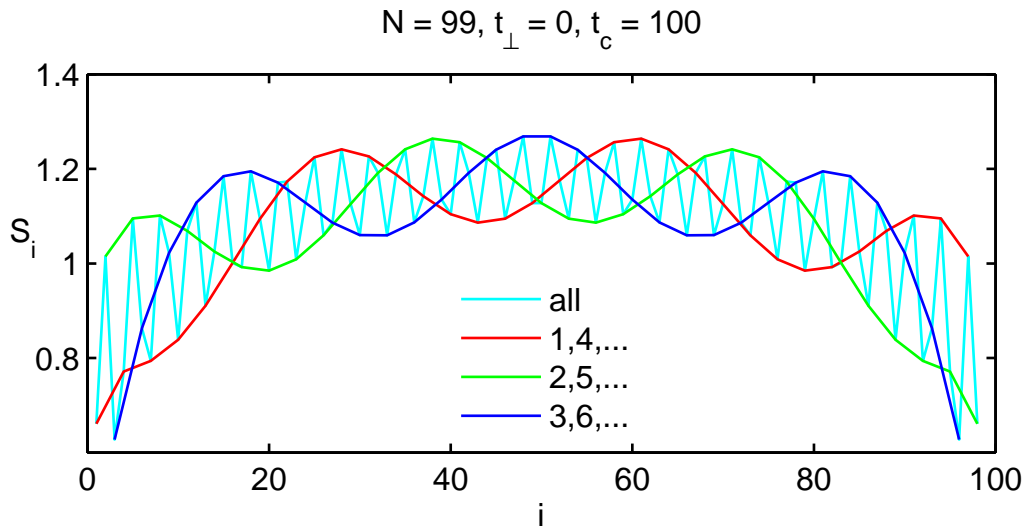


Figure 5.16: The bond entropy along the whole chain with chain length  $N = 99$ . On a first glance the bond entropy looks very irregular (cyan curve), but on a closer look it reveals regularity. Interestingly, if one arranges the sites in intervals of three sites (sites 1,4,... - red curve; sites 2,5,... - green curve; sites 3,6,... - blue curve) they show oscillating behaviour.

## (ii) Zero inter-leg hopping

The parameters are chosen as  $t_{\perp} = 0$  and  $t_c = 0$ . The staggered ground state is clearly reproduced for a chain length of  $N = 99$ , see Fig. 5.17. For  $N = 100$  the results look very similar, but the particles are delocalized over two adjacent sites on a leg. There is no new feature as this behaviour still represents the staggered ground state and thus these results are not shown.

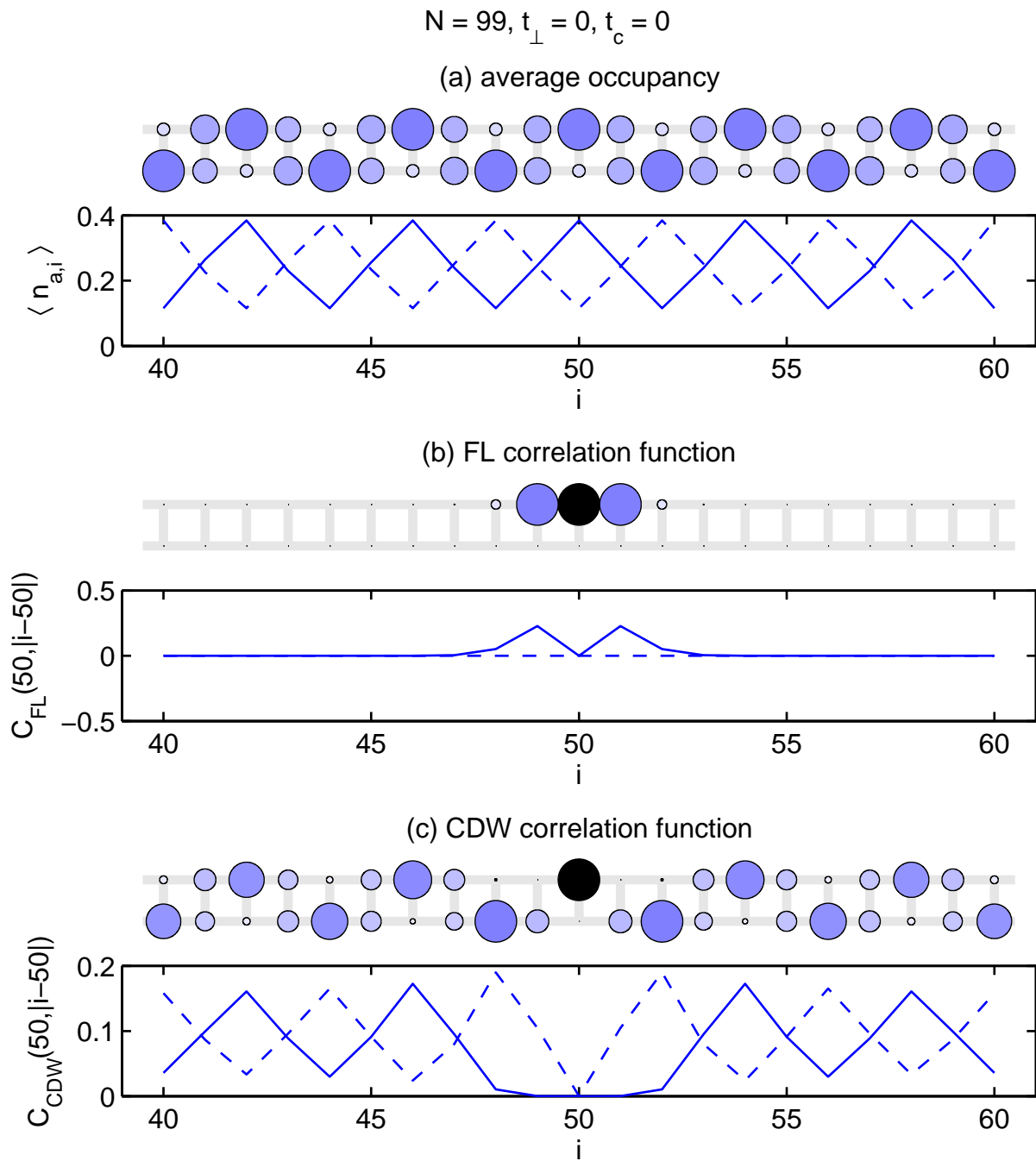


Figure 5.17: Average occupancy and correlation functions for a chain of length  $N = 99$  around rung 50 ( $V = 10^4, t = 1$ ). The solid lines correspond to the upper leg and the dashed lines correspond to the lower leg. a) The average occupancy. One can clearly see the alternating behaviour of occupancy, which indicates the staggered ground state. b) The correlation function  $C_{\text{FL}}(50, |i - 50|) = \langle c_{a,i}^\dagger c_{\uparrow,50} \rangle$ . The confinement of a particle between two other particles shows up. c) The correlation function  $C_{\text{CDW}}(50, |i - 50|) = \langle n_{a,i} n_{\uparrow,50} \rangle$ . This correlation function yields no more information than the average occupancy.

The bond entropy of this ground state shows a sub-structure which distinguishes between

even and odd sites. This is reasonable as for example the average occupancy also shows different values for even and odd sites.

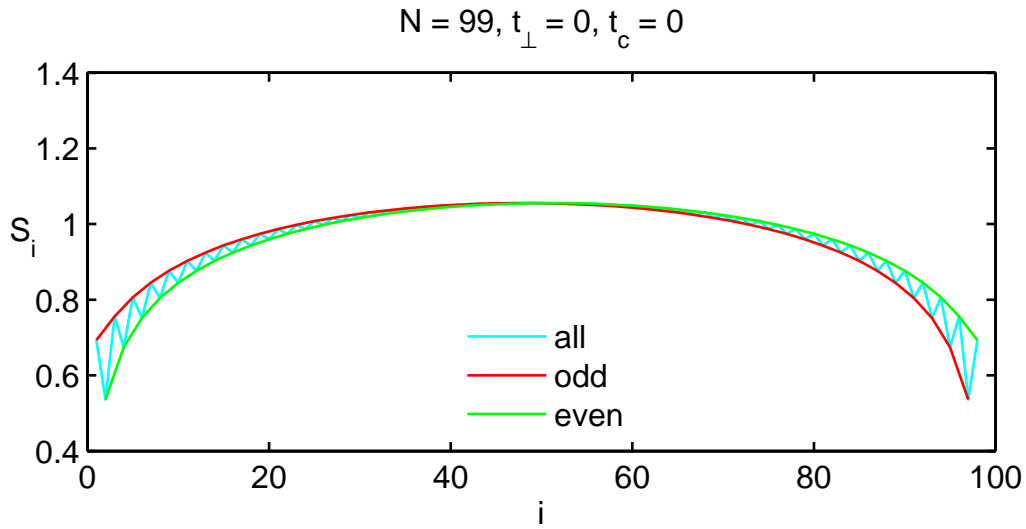


Figure 5.18: The bond entropy along the whole chain for a chain length of  $N = 99$ . The entropies of all bonds (cyan curve) is divided into the entropies of even (green curve) and odd (red curve) bonds.

### (iii) Strong inter-leg hopping

The parameters are chosen as  $t_{\perp} = 100$  and  $t_c = 0$ . The fermions are delocalized over the rungs and as explained in Sec. 5.2, the ground state is degenerate for  $N = 100$ , see Fig. 5.20. For  $N = 99$  the structure of the ground state is quite simple, see Fig. 5.19.

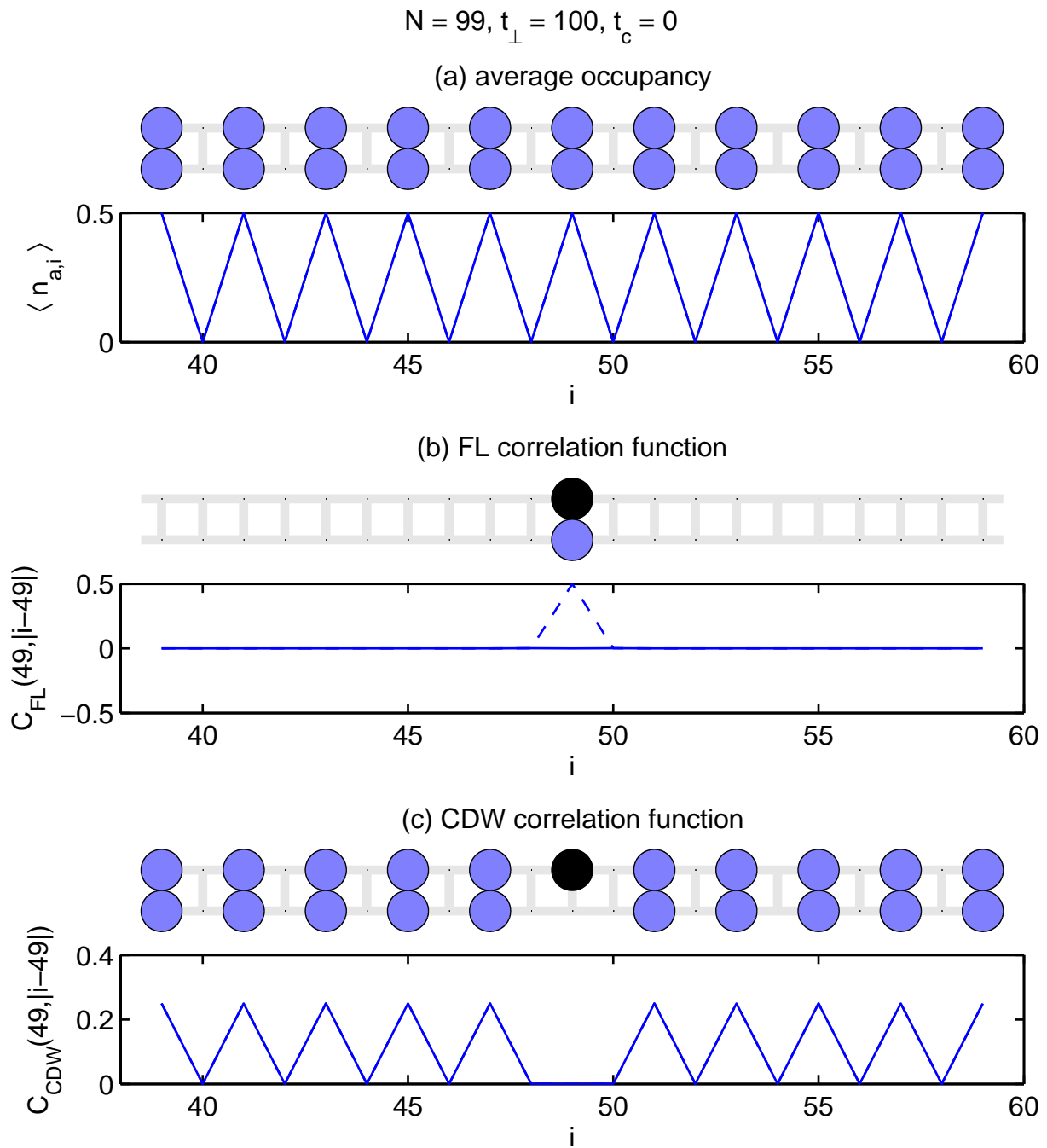


Figure 5.19: Average occupancy and correlation functions for a chain of length  $N = 99$  around rung 49 ( $V = 10^4, t = 1$ ). The solid lines correspond to the upper leg and the dashed lines correspond to the lower leg, but due to the dominating inter-leg hopping the ground state is symmetric under leg interchange and the lines coincide for the most part. a) The average occupancy. The fermions are delocalized on the odd legs. b) The correlation function  $C_{FL}(49, |i - 49|) = \langle c_{a,i}^\dagger c_{\uparrow,49} \rangle$ . Current is only possible along rungs due to the infinite nearest neighbour repulsion. c) The correlation function  $C_{CDW}(49, |i - 49|) = \langle n_{a,i} n_{\uparrow,49} \rangle$ . This correlation function yields no more information than the average occupancy.

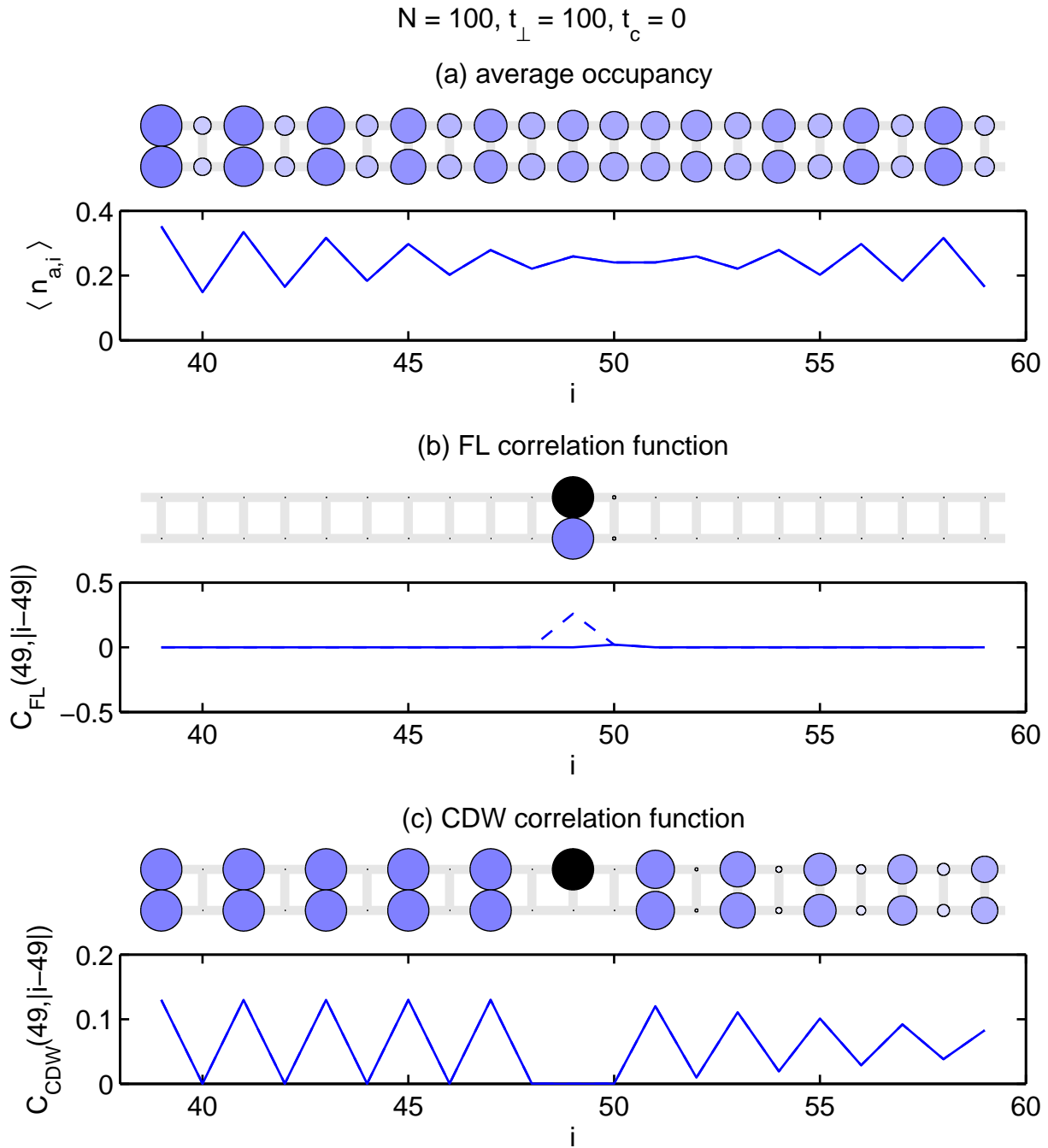


Figure 5.20: Average occupancy and correlation functions for a chain of length  $N = 100$  around rung 49 ( $V = 10^4, t = 1$ ). The solid lines correspond to the upper leg and the dashed lines correspond to the lower leg, but due to the dominating inter-leg hopping the ground state is symmetric under leg interchange and the lines coincide for the most part. a) The average occupancy. The fermions are delocalized on the rungs and one has a superposition of the two states, where the fermions are on the even and odd rungs, respectively. There seems to be a relative phase between the two ground states and thus one obtains oscillating behaviour. b) The correlation function  $C_{FL}(49, |i - 49|) = \langle c_{a,i}^\dagger c_{\uparrow,49} \rangle$ . Current is only possible along rungs due to the infinite nearest neighbour repulsion. c) The correlation function  $C_{CDW}(49, |i - 49|) = \langle n_{a,i} n_{\uparrow,49} \rangle$ . This correlation function picks one of the two degenerate states, in this case the one with fermions on the odd rungs, and shows its CDW behaviour. The asymmetry comes from the fact, that a division of a chain with even length into two parts left and right of one site is already asymmetric. If one chooses site 50 for the division the picture is mirrored.

The bond entropy of the chain with length  $N = 99$  reflects the simple structure of the ground state. The very small entropy indicates that the state is nearly a product state like the Heisenberg chain, see Fig. 5.21. In contrast the result for a chain length of  $N = 100$  shows a division of the entropy in two curves for even and odd bonds, see Fig. 5.22. It becomes larger to the middle of the chain, which is reasonable as more information has to be carried through these bonds.

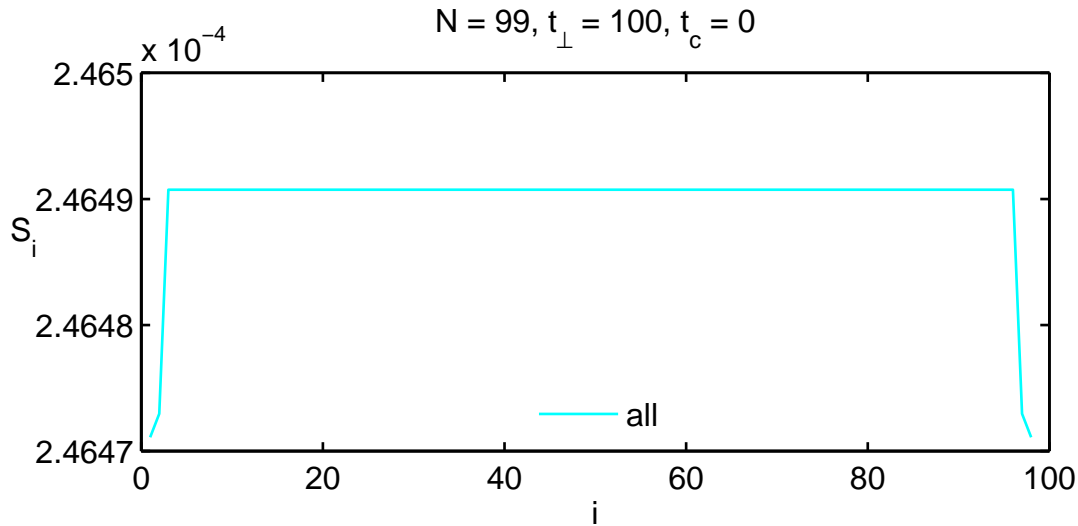


Figure 5.21: The bond entropy for chain with length  $N = 99$ . The small value, which is constant over nearly the full chain indicates a product state.

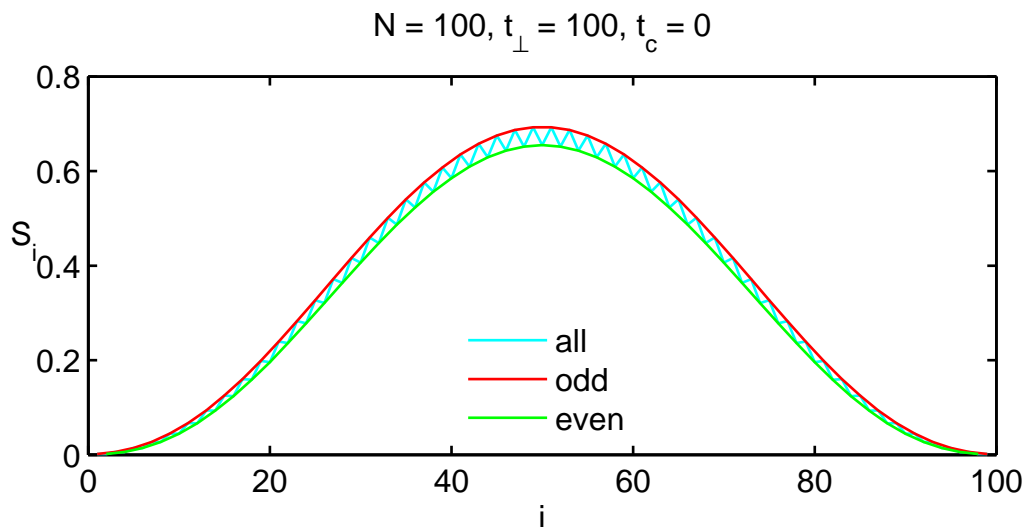


Figure 5.22: The bond entropy for a chain with length  $N = 100$ . One can see the even-odd structure of the bond entropy.

## 5.4 Investigation of the correlation density matrix

After all the numerical checks and investigations of expectation values and correlation functions, we have enough knowledge of the system to investigate the correlation density matrix for various parameters. We extract the behaviour of the correlations for the three limiting cases for which an analytical solution exists.

For a given ground state with chain length  $N = 99$  or  $N = 100$  we calculated several correlation density matrices with cluster size 2 and made the average over them to reduce finite size effects. The CDMs were calculated as follows. Choosing two starting sites for cluster  $A$  and two adjacent sites for cluster  $B$ , e.g. sites (49, 50) for cluster  $A$  and (51, 52) for cluster  $B$ , we calculated the CDM for these two clusters, obtaining the CDM for a distance of 2. Afterwards the two clusters depart symmetrically from each other, i.e. cluster  $A$  moves one site to the left, a CDM is calculated (with distance 3), cluster  $B$  moves one site to the right, and so on. This procedure gives the most cluster configurations, which are far apart from the boundaries, and the longest distances. This procedure is repeated for several starting sites, ranging from site 40 to 60, in particular for every configuration its mirrored configuration with respect to the middle of the chain is calculated. All these CDMs are decomposed as described in Sec. 4.2 and the resulting curves for the symmetry classes are averaged. A first result is, that the 'offdiagonal' symmetry weights  $W_{ij}^{AB}$  with  $i \neq j$  are all smaller than about  $10^{-10}$ , which was demanded by particle conservation.

For correlations with a power law decay we extracted the critical exponent from fitting curves of the type

$$cr^{-2\alpha}, \quad (5.3)$$

where  $c$  is a prefactor and  $\alpha$  the desired exponent. The reason for the factor of two in the exponent is, that the symmetry weights consist of the squares of the singular values (see Sec. 4.2). To compare the fitting curves with the exact results one has to extract the root of the fitting curves, which eliminates the factor of 2. Thus  $\alpha$  gives the exponent of the power law correlation function and may be compared directly with the exact exponent. The range for the fitting goes from site 4 (to exclude the first few comparatively great values) up to distances of about 20 to 30 sites. The exact value depends on the curve under consideration. These comparatively small ranges (the CDM goes to distances of about 80) take the results from Sec. 5.1.2 into account, from which one could see that the correlations are given faithfully only for distances of about these values.

### (i) Strong correlated hops

In this parameter range, i.e.  $t_{\perp} = 0$  and  $t_c = 100$ , we expect from Tbl. 1.1 a leading correlation exponent of  $\frac{9}{8}$  for a filling fraction of 0.25 for the CDW correlations and an exponent of  $\frac{1}{2}$  for the SC correlations. The FL correlations are expected to decay exponentially. The results for a chain length of  $N = 99$  and  $N = 100$  show the same behaviour and thus we only investigate more closely the  $N = 99$  results. The averaged symmetry weights as a function of the distance  $r$  are shown in Fig. 5.23 on a double logarithmic plot to stress the power law

behaviour of the CDW and SC correlations. The FL correlation decays exponentially, which is shown in detail in Fig. 5.24.

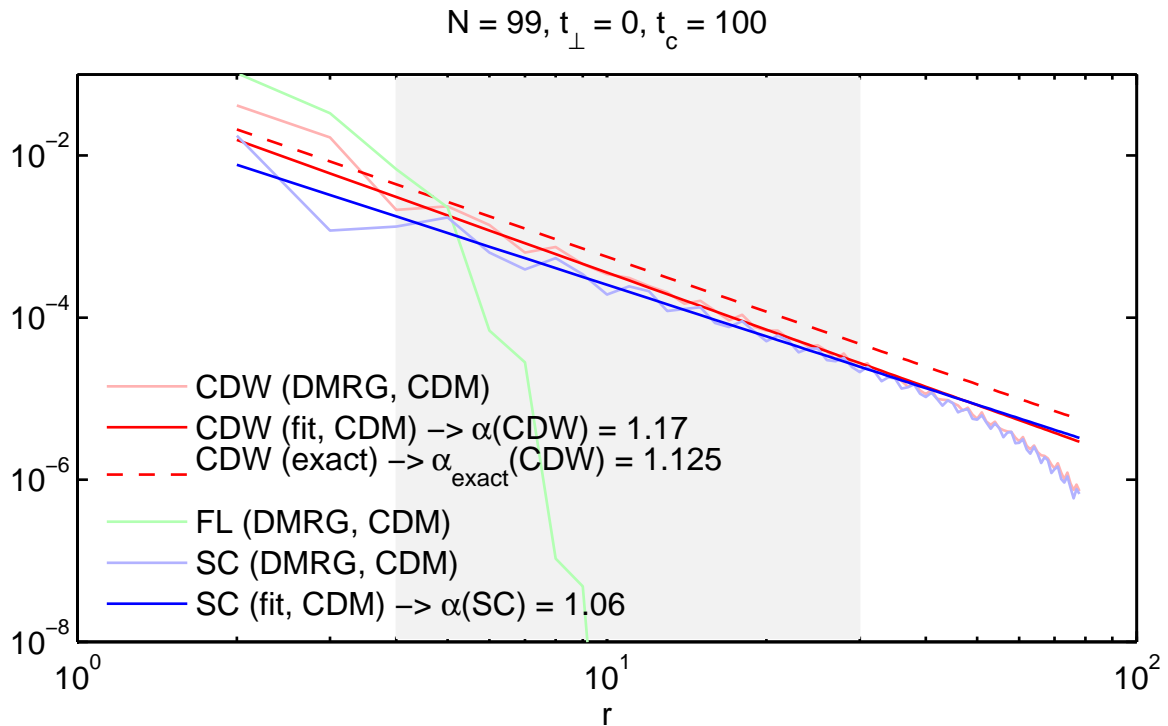


Figure 5.23: The three symmetry weights for CDW, FL and SC correlations. The FL correlations are the greatest for short distances, but decay exponentially fast and have no influence on the long-range behaviour. The CDW and SC correlations decay as a power law and a fitting is applied to obtain the exponent. The range that was used for the fitting has been shaded in grey. For the CDW correlations the extracted exponent  $\alpha(\text{CDW}) = 1.17$  fits good to the exact result  $\alpha_{\text{exact}}(\text{CDW}) = 1.125$ . The exact curve is plotted for comparison, whereas the constant factor of the power law is chosen such that the curves are close together. We do not have an exact value for this constant. The SC correlation does not yield such an agreement, the extracted exponent  $\alpha(\text{SC}) = 1.06$  is more than twice the exact value of  $\alpha_{\text{exact}}(\text{SC}) = 0.5$ .

In this limiting case the numerical results reproduce the basic features of the exact results, the power law behaviour of the CDW and SC correlations and the exponential decay of the FL correlations. Moreover, at least one critical exponent is extracted which is close to the expected exact value (see Tbl. 1.1).

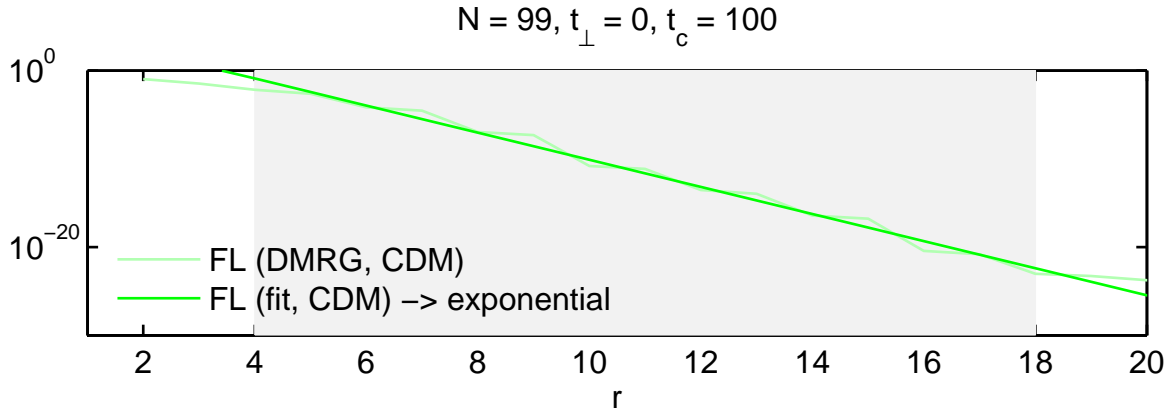


Figure 5.24: The exponential decay of the FL correlation. The range that was used for the fitting has been shaded in grey. One can clearly see the exponential decay down to values below  $10^{-20}$ .

## (ii) Zero inter-leg hopping

In this parameter range, i.e.  $t_{\perp} = 0$  and  $t_c = 0$ , we expect from Tbl. 1.1 a leading correlation exponent of  $\frac{1}{2}$  for the CDW correlations and an exponent of 2 for the SC correlations. The FL correlations are expected to decay exponentially. Our results for the averaged symmetry weights as a function of the distance  $r$  are shown in Fig. 5.25. The results for a chain length of  $N = 99$  and  $N = 100$  show similar behaviour and thus we only investigated more closely the  $N = 99$  results closer. The FL correlation decays exponentially, which is shown in detail in Fig. 5.26.

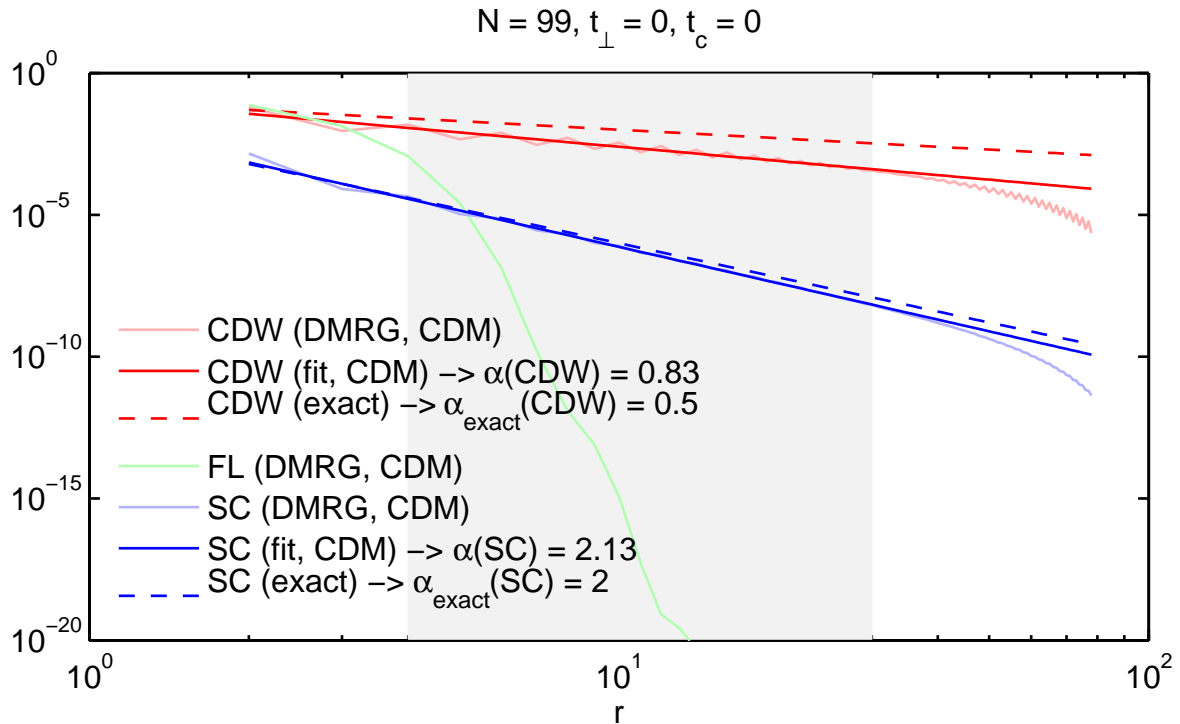


Figure 5.25: The three symmetry weights for CDW, FL and SC correlations. The FL correlations are about the greatest for short distances, but decay exponentially fast and have no influence on the long-range behaviour. The CDW and SC correlations decay as a power law and a fitting is applied to obtain the exponent. The range that was used for the fitting has been shaded in grey. For the CDW correlations the extracted exponent  $\alpha(\text{CDW}) = 0.83$  does not fit very well to the exact result  $\alpha_{\text{exact}}(\text{CDW}) = 0.5$ . The SC correlation yields a better agreement, the extracted exponent  $\alpha(\text{SC}) = 2.13$  is close to the exact value of  $\alpha_{\text{exact}}(\text{SC}) = 2$ . The exact curves are plotted for comparison, whereas the constant factors of the power law are chosen such that corresponding curves are close together. We do not have exact values for these constants.

In this case we could again reproduce the basic features of the exact solution. A power law for the CDW and SC correlations and exponential decay for the FL correlations was found. The critical exponents extracted from our calculations are not contra-dictionary to the exact values.

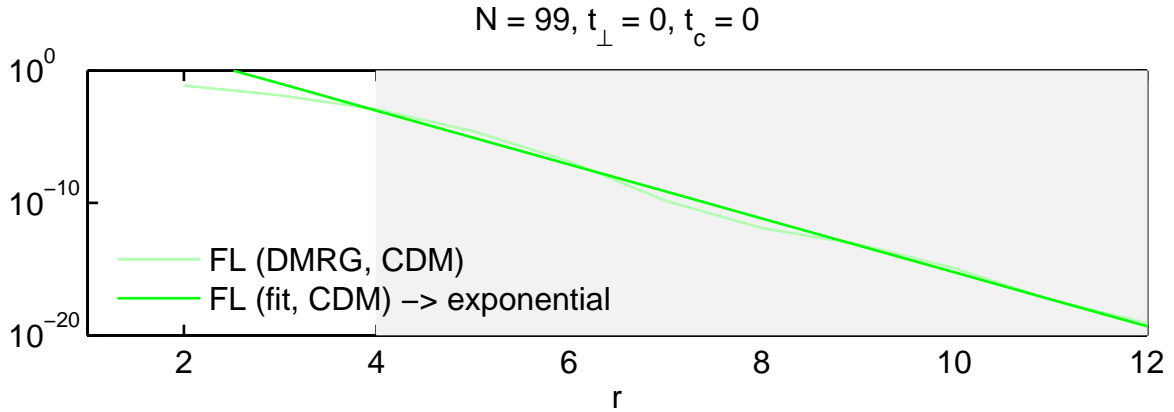


Figure 5.26: The exponential decay of the FL correlation. The range that was used for the fitting has been shaded in grey. One can clearly see the exponential decay down to values below  $10^{-20}$ .

### (iii) Strong inter-leg hopping

In this parameter range, i.e.  $t_{\perp} = 100$  and  $t_c = 0$ , we expect from Sec. 1.3 power laws for all three symmetry types. We did not find this behaviour, neither for a chain length of  $N = 99$ , nor for  $N = 100$ . This discrepancy is surprising because from numerical criteria the results in this case appear more accurate compared to in the other cases. For  $N = 99$  we find essentially no correlations, which is reasonable for a product state, see Fig. 5.27. The system seems to be gaped in this case with the chemical potential within the gap, so that excitations are very unlikely.

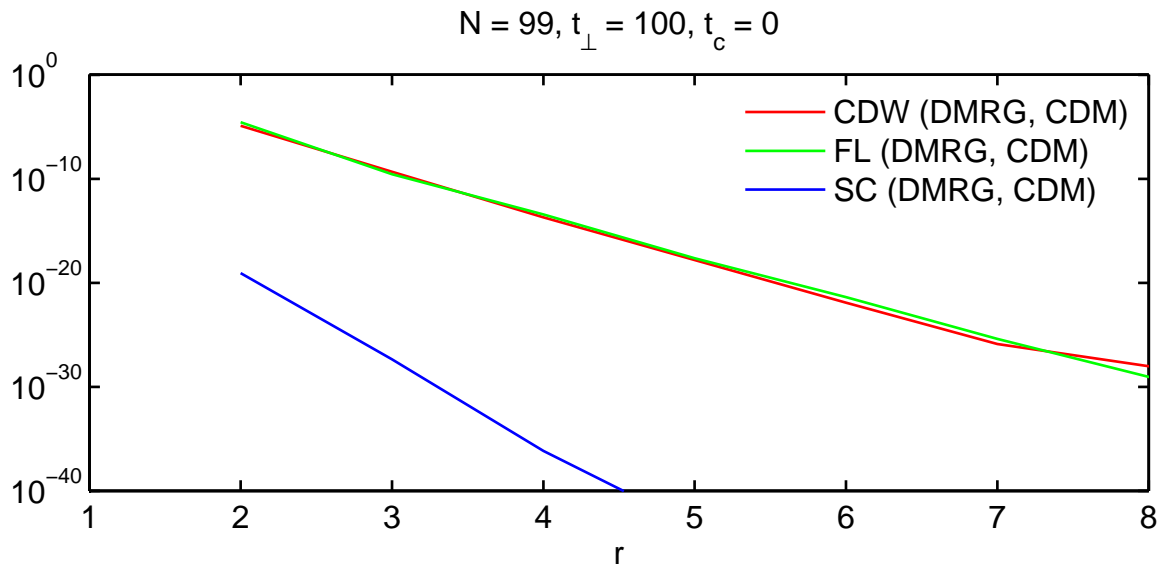


Figure 5.27: Correlations for the chain with length  $N = 99$ . The correlations have a very small value for  $r = 2$  and decay afterwards. From these small values one cannot extract any conclusive information.

For  $N = 100$  we find a CDW correlation with non-vanishing values over long distances, but the curve is neither a power law, nor an exponential decay. The FL and SC correlations decay very fast and have no influence over long distances, see Fig. 5.28.

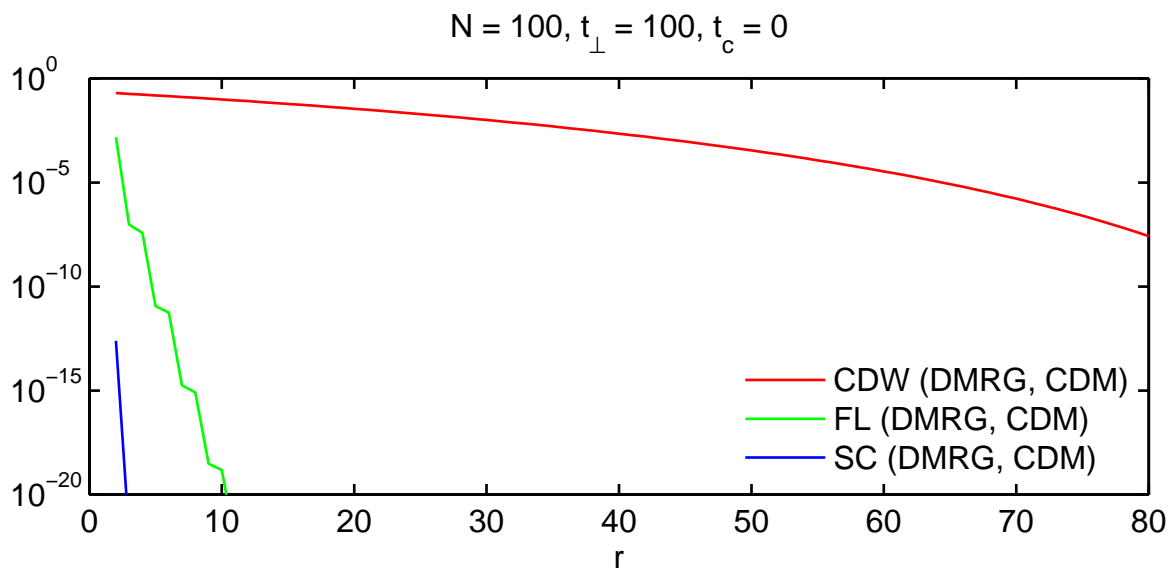


Figure 5.28: Correlations for the chain with length  $N = 99$ . The FL and SC correlations decay quickly. The CDW correlations decay very slow, but it is unclear in which way.

In this parameter regime, we could not reproduce the exact results at all. As mentioned

above, we do not have an explanation for this discrepancy, because we expected better results from the numerical checks.

# Chapter 6

## Outlook

### **Accuracy of the DMRG calculations**

The accuracy of our DMRG method is reasonable, but is also not very high. One can clearly see that for good results of correlations one needs states which are well converged numerically. To increase the accuracy the increase of the cutoff dimension  $D$  becomes prohibitive. Our choice of  $D = 64$  already requires a lot of time and an increase of  $D$  appears unefficient. This clearly suggests the implementation of (Abelian) symmetries, i.e. to account for symmetries conserved by the Hamiltonian to reduce the full matrix space to an efficiently sparse block matrix space.

### **Investigation of the correlation density matrix**

We succeeded to reproduce several features of the results of [1, 2] as presented Sec. 1.3. The structure of the phase diagram in Fig. 1.5 is supported by our results. The investigation of the correlation density matrix did not yield complete agreement, but some results are very promising. To obtain better results, we have to increase the dimension of the matrix product state to obtain better ground states. Moreover, our investigation of the correlation density matrix is on a rather crude level. One can analyze the operators from the singular value decomposition in a more diligent way, which has been done by Siew-Ann Cheong and Christopher L. Henley [2] and could be similarly complemented by DMRG calculations in the full parameter range of the model analyzed.



# Appendix A

## Further details

### A.1 Jordan-Wigner transformation

The Jordan-Wigner transformation, which was first introduced by Jordan and Wigner in 1928 [15], transforms fermionic creation and annihilation operators in a way that they obtain almost bosonic commutator relations instead of the fermionic anti-commutator relations. This greatly simplifies the numerical treatment of these operators as one can ignore for most part fermionic signs. This approach works well in one dimension, which is sufficient for this thesis, but becomes more complex for higher dimensions [8].

#### A.1.1 Definition

To correctly apply fermionic operators one needs an order in which fermionic operators are applied on the totally empty or 'vacuum' state. If one has such an order for a set  $\{c_i\}$  with  $i = 1 \dots N$ , one can make the following transformation

$$\tilde{c}_i \equiv \left( (-1)^{\sum_{k<i} c_k^\dagger c_k} \right) c_i = \left( \prod_{k<i} (-1)^{c_k^\dagger c_k} \right) c_i = \left( \prod_{k<i} z_k \right) c_i = Z_i c_i, \quad (\text{A.1})$$

with the local and non-local sign operators

$$z_k = (-1)^{c_k^\dagger c_k} = z_k^\dagger \quad Z_i = \prod_{k<i} z_k = Z_i^\dagger. \quad (\text{A.2})$$

One immediately sees that  $\tilde{c}_i^\dagger \tilde{c}_i = Z_i^2 c_i^\dagger c_i = c_i^\dagger c_i$  and so the inverse transformation is

$$c_i \equiv \left( (-1)^{\sum_{k<i} \tilde{c}_k^\dagger \tilde{c}_k} \right) \tilde{c}_i. \quad (\text{A.3})$$

## A.1.2 Commutator relations

With the fermionic anti-commutator relations and the identity

$$z_k = (-1)^{c_k^\dagger c_k} = 1 - 2c_k^\dagger c_k = [c_k, c_k^\dagger], \quad (\text{A.4})$$

one easily obtains

$$\{\tilde{c}_i, \tilde{c}_i^\dagger\} = Z_i^2 \{c_i, c_i^\dagger\} = \{c_i, c_i^\dagger\}, \quad (\text{A.5})$$

$$\{\tilde{c}_i^\dagger, \tilde{c}_i^\dagger\} = Z_i^2 \{c_i^\dagger, c_i^\dagger\} = \{c_i^\dagger, c_i^\dagger\}, \quad (\text{A.6})$$

$$\{\tilde{c}_i, \tilde{c}_i\} = Z_i^2 \{c_i, c_i\} = \{c_i, c_i\}, \quad (\text{A.7})$$

and for  $i \neq j$  (assuming  $i \leq j$  without restricting the case)

$$\begin{aligned} [\tilde{c}_i, \tilde{c}_j^\dagger] &= Z_i c_i Z_j c_j^\dagger - Z_j c_j^\dagger Z_i c_i = Z_i^2 \left( c_i z_i \left( \prod_{k=i+1}^{j-1} z_k \right) c_j^\dagger - z_i \left( \prod_{k=i+1}^{j-1} z_k \right) c_j^\dagger c_i \right) \\ &= \left( \prod_{k=i+1}^{j-1} z_k \right) \left( \underbrace{c_i c_i}_{=0} c_j^\dagger c_j^\dagger - \underbrace{c_i c_i^\dagger c_i c_j^\dagger}_{c_j^\dagger c_i} - \underbrace{c_i c_i^\dagger c_j^\dagger c_i}_{c_j^\dagger c_i} + \underbrace{c_i^\dagger c_i c_j^\dagger c_i}_{-c_j^\dagger c_i} \underbrace{c_i c_i}_{=0} \right) \\ &= 0, \end{aligned} \quad (\text{A.8})$$

$$[\tilde{c}_i^\dagger, \tilde{c}_j^\dagger] = Z_i^2 \left( c_i^\dagger z_i \left( \prod_{k=i+1}^{j-1} z_k \right) c_j^\dagger - z_i \left( \prod_{k=i+1}^{j-1} z_k \right) c_j^\dagger c_i^\dagger \right) = 0, \quad (\text{A.9})$$

$$[\tilde{c}_i, \tilde{c}_j] = Z_i^2 \left( c_i z_i \left( \prod_{k=i+1}^{j-1} z_k \right) c_j - z_i \left( \prod_{k=i+1}^{j-1} z_k \right) c_j c_i \right) = 0. \quad (\text{A.10})$$

Thus the fermionic anti-commutator relations have been transformed to commutator relations, which are locally fermionic and otherwise bosonic:

$$\begin{aligned} [\tilde{c}_i, \tilde{c}_j^\dagger] &= \delta_{ij} [c_i, c_i^\dagger] & [\tilde{c}_i^\dagger, \tilde{c}_j^\dagger] &= 0 & [\tilde{c}_i, \tilde{c}_j] &= 0 \end{aligned} \quad (\text{A.11})$$

$$\{\tilde{c}_i, \tilde{c}_i^\dagger\} = 1 \quad \{\tilde{c}_i^\dagger, \tilde{c}_i^\dagger\} = 0 \quad \{\tilde{c}_i, \tilde{c}_i\} = 0$$

The Pauli exclusion principle is conserved as  $\tilde{c}_i^\dagger \tilde{c}_i^\dagger = 0$  and physics are unchanged, but the fermionic signs are obtained much simpler. But this has the price that for every operator in the old basis new operators occur. First noting that

$$\tilde{c}_i^\dagger z_i = \tilde{c}_i^\dagger, \quad (\text{A.12})$$

$$z_i \tilde{c}_i = \tilde{c}_i, \quad (\text{A.13})$$

$$z_i n_i = n_i z_i = -n_i, \quad (\text{A.14})$$

one sees that for a pair of operators (creation or annihilation) the sign operators on all sites which are between them - in the sense of the chain ordering, not spatially between them - have to be evaluated. For example the operators for the correlation function  $c_i^\dagger c_j$  become

$$c_i^\dagger c_j = Z_i \tilde{c}_i^\dagger Z_j \tilde{c}_j = Z_i^2 \tilde{c}_i^\dagger z_i \left( \prod_{k=i+1}^{j-1} z_k \right) \tilde{c}_j = \tilde{c}_i^\dagger \left( \prod_{k=i+1}^{j-1} z_k \right) \tilde{c}_j. \quad (\text{A.15})$$

This has to be worked out for every term separately.

### A.1.3 Application to a ladder model

First one has to implement an ordering scheme. The order starts at the leftmost rung, taking the upper site as the first site and the lower one as second. Then it goes to the right, setting site  $(a, i) = (1, 2)$  as third, site  $(a, i) = (2, 2)$  as fourth and so on. For an infinite ladder the order is the same, but the limits of  $i$  are minus and plus infinity.

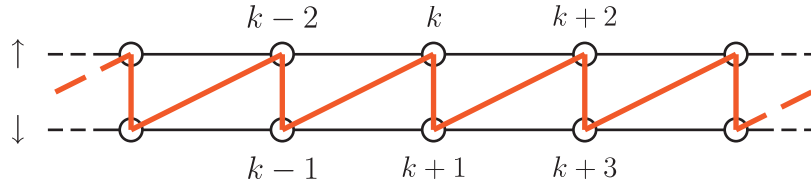


Figure A.1: Ordering scheme for the ladder model

In this order the Hamiltonian as in Eq. (1.1) acquires several additional terms. In particular the mapping onto a one-dimensional Hamiltonian does not mean that one may abandon the substructure of individual sites for the operators in the Jordan-Wigner basis. After the transformation the Hamiltonian has the form:

$$\begin{aligned} H = & -t_{\parallel} \sum_i (\tilde{c}_{1,i}^\dagger z_{2,i} \tilde{c}_{1,i+1} + \tilde{c}_{1,i+1}^\dagger z_{2,i} \tilde{c}_{1,i} + \tilde{c}_{2,i}^\dagger z_{1,i+1} \tilde{c}_{2,i+1} + \tilde{c}_{2,i+1}^\dagger z_{1,i+1} \tilde{c}_{2,i}) \\ & -t_{\perp} \sum_i (\tilde{c}_{1,i}^\dagger \tilde{c}_{2,i} + \tilde{c}_{2,i}^\dagger \tilde{c}_{1,i}) \\ & -t_c \sum_i (\tilde{c}_{1,i-1}^\dagger z_{2,i-1} z_{1,i} (-n_{2,i}) \tilde{c}_{1,i+1} + \tilde{c}_{1,i+1}^\dagger (-n_{2,i}) z_{1,i} z_{2,i-1} \tilde{c}_{1,i-1} \\ & \quad + \tilde{c}_{2,i-1}^\dagger (-n_{1,i}) z_{2,i} z_{1,i+1} \tilde{c}_{2,i+1} + \tilde{c}_{2,i+1}^\dagger z_{1,i+1} z_{2,i} (-n_{1,i}) \tilde{c}_{2,i-1}) \\ & +V \sum_{a=1}^2 \sum_i n_{a,i} n_{a,i+1} + V \sum_i n_{1,i} n_{2,i}, \end{aligned} \quad (\text{A.16})$$

which acquires several local  $z$  operators that must be accounted for.

## A.2 Derivation of the orthonormality condition

The orthonormality condition Eq. (2.7) is easily shown by a complete induction. Starting point is the condition Eq. (2.6).

### Effective left basis

First one has to notice that the left basis of site one is orthonormal as it consists only of the vacuum state. So the induction starts with site one having an orthonormal effective left basis. Now, considering the case that site  $k$  has an orthonormal effective left basis, what condition is needed for site  $k + 1$  to have an orthonormal effective left basis, too?

$$\begin{aligned}
\langle l'_{k+1} | l_{k+1} \rangle &= \left( \sum_{l'_k \sigma'_k} \langle l'_k | \langle \sigma'_k | \left( A^{[\sigma'_k]} \right)_{l'_k l'_{k+1}}^* \right) \left( \sum_{l_k \sigma_k} A_{l_k l_{k+1}}^{[\sigma_k]} | l_k \rangle | \sigma_k \rangle \right) \\
&= \sum_{l'_k l_k \sigma'_k \sigma_k} \left( A^{[\sigma'_k]} \right)_{l'_k l'_{k+1}}^* A_{l_k l_{k+1}}^{[\sigma_k]} \underbrace{\langle l'_k | l_k \rangle}_{\delta_{l'_k l_k}} \underbrace{\langle \sigma'_k | \sigma_k \rangle}_{\delta_{\sigma'_k \sigma_k}} \\
&= \sum_{l_k \sigma_k} \left( A^{[\sigma_k]} \right)_{l'_{k+1} l_k}^\dagger A_{l_k l_{k+1}}^{[\sigma_k]} \\
&= \left( \sum_{\sigma_k} \left( A^{[\sigma_k]} \right)^\dagger A^{[\sigma_k]} \right)_{l'_{k+1} l_{k+1}}. \tag{A.17}
\end{aligned}$$

Condition Eq. (2.7) follows with  $\langle l'_{k+1} | l_{k+1} \rangle \stackrel{!}{=} \delta_{l'_{k+1} l_{k+1}}$ .

### Effective right basis

The same arguments as for the effective left basis are applied. As one goes from right to left the induction is changed from  $k \rightarrow k + 1$  to  $k \rightarrow k - 1$ . One obtains the following relation:

$$\begin{aligned}
\langle r'_{k-1} | r_{k-1} \rangle &= \sum_{r_k \sigma_k} A_{r_{k-1} r_k}^{[\sigma_k]} \left( A^{[\sigma_k]} \right)_{r_k r'_{k-1}}^\dagger \\
&= \left( \sum_{\sigma_k} A^{[\sigma_k]} \left( A^{[\sigma_k]} \right)^\dagger \right)_{r_{k-1} r'_{k-1}}. \tag{A.18}
\end{aligned}$$

Condition Eq. (2.7) follows with  $\langle r'_{k-1} | r_{k-1} \rangle \stackrel{!}{=} \delta_{r'_{k-1} r_{k-1}}$ .

## A.3 Singular value decomposition

The singular value decomposition can be seen as a generalization of the spectral theorem, i.e. of the eigenvalue decomposition. It is valid for any real or complex  $m \times n$  rectangular matrix, see [16] for details. Let  $M$  be such a matrix, then it can be written in a singular value decomposition

$$M = U\Sigma V^\dagger, \quad (\text{A.19})$$

where  $U$  is a  $m \times m$  unitary matrix,  $\Sigma$  a  $m \times n$  matrix with nonnegative numbers on the diagonal and zeros off the diagonal, and  $V$  a  $n \times n$  unitary matrix. The numbers on the diagonal of  $\Sigma$  - the singular values, there are  $p = \min(n, m)$  of them - are unique, but  $U$  and  $V$  are not in general. It is convenient to truncate and reorder these matrices to  $U$  as  $m \times p$ ,  $\Sigma$  as  $p \times p$  (with the singular values ordered in a non-increasing fashion) and  $V$  as  $n \times p$  ( $V^\dagger$  as  $p \times n$ ). Of course  $U$ ,  $\Sigma$  and  $V$  are reordered in the same way. A consequence of this truncation is that  $U$  or  $V$  is no longer quadratic and unitarity is not defined for such matrices. This property is replaced by *column unitarity* (orthonormal columns) of  $U$  and *row unitarity* (orthonormal rows) for  $V^\dagger$  - no matter which one is no longer quadratic. In this thesis all singular value decompositions are ordered in this fashion.

## A.4 Numerical costs of matrix multiplications and index contractions

The numerical costs of matrix multiplications and index contractions of multi-index objects depend on the dimension of both the resulting object and of the contracted indices. In the case of matrix multiplications this is quite simple. Consider a  $n \times m$  matrix  $M_1$  multiplied with a  $m \times p$  matrix  $M_2$ . The result is a  $n \times p$  matrix  $M$ :

$$M_{ij} = \sum_{k=1}^m (M_1)_{ik} (M_2)_{kj}. \quad (\text{A.20})$$

Evidently, each of the  $np$  matrix elements  $M_{ij}$  requires a sum over  $m$  products of the form  $(M_1)_{ik} (M_2)_{kj}$ . Thus the process for calculating  $M_1 M_2$  is of order  $\mathcal{O}(nmp)$ .

The numerical costs of multi-index objects are obtained analogously. Consider two multi-index objects,  $M_1$  with indices  $i_1, \dots, i_n$  and dimensions  $p_1 \times \dots \times p_n$  and  $M_2$  with indices  $j_1, \dots, j_m$  and dimensions  $q_1 \times \dots \times q_m$ . If one contracts the indices  $i_1$  and  $i_2$  of  $M_1$  with the indices  $j_1$  and  $j_2$  of  $M_2$  (assuming that  $p_1 = q_1$  and  $p_2 = q_2$ ), one obtains the multi-index object  $M$ :

$$M_{i_3 \dots i_n j_3 \dots j_m} = \sum_{k=1}^{p_1} \sum_{l=1}^{p_2} (M_1)_{k l i_3 \dots i_n} (M_2)_{k l j_3 \dots j_m}. \quad (\text{A.21})$$

Thus for every entry of  $M$ ,  $p_1$  times  $p_2$  multiplications have to be done, so that the process is of order  $\mathcal{O}((p_3 \dots p_n)(p_1 p_2)(q_3 \dots q_m))$ .

# List of Figures

1.1	Ladder model . . . . .	4
1.2	Hamiltonian terms (from left to right): rung hopping, leg hopping, correlated hopping and nearest neighbour repulsion. Black circles denote occupied sites and white circles unoccupied ones. . . . .	4
1.3	Tight binding chain . . . . .	6
1.4	Transformation of open boundary conditions: a) Initial boundary conditions. b) Boundary conditions with additional sites at the ends. c) Final periodic boundary conditions. . . . .	9
1.5	The zeroth-order ground-state phase diagram of the quarter-filled spinless extended Hubbard model with infinite nearest neighbour repulsion and correlated hopping on a two-leg ladder. The three limiting cases investigated by Cheong and Henley are depicted by the two dots and the thick solid line. Taken from [2]. . . . .	12
1.6	Effective extended hardcore bosons with even (red) and odd (green) flavour. It is not possible for an extended hardcore boson to change its flavour by correlated hopping. Taken from [2]. . . . .	15
1.7	Possible configurations of fermions in the zero inter-leg hopping case: a) the staggered ground state with fermions on alternating legs b) another state with the same number of fermions, but all on the same leg. The fermions have less degrees of freedom and thus the state is of higher energy. Taken from [2]. . . . .	15
2.1	Current site with effective basis sets. . . . .	18
2.2	Graphical representation of a matrix product state in the a) global view and b) local view. . . . .	20
2.3	Singular value decomposition of the $A$ -matrices . . . . .	21
2.4	Rearrangement of the $A$ -matrices to switch the current site from site $k$ to $k + 1$ . . . . .	21
2.5	Orthonormal effective right basis for site $k - 1$ . . . . .	22
2.6	Procedure for site update within two-site DMRG. The grey line under the $s$ indicates that $s$ is the diagonal matrix of singular values. . . . .	23

2.7	Scalar product, computed in two different orders. a) First all $A$ -matrices of $ \psi\rangle$ and $ \psi'\rangle$ are contracted and then one contracts over the local indices. This last contraction is carried out over the full Hilbert space, i.e. a $1 \times d^N$ matrix is multiplied with a $d^N \times 1$ matrix, and thus of order $\mathcal{O}(d^N)$ , which is completely unfeasible for practical purposes. b) First, for site one, one contracts over the local indices of $A_1$ and $A'_1$ . Then one contracts over the effective index between $A_1$ and $A_2$ and afterwards over the indices between the resulting object and $(A'_2)^*$ . One proceeds with site three and so on over the whole chain. The most 'expensive' contraction is in the middle of the chain, say at site $k$ , and it is of order $\mathcal{O}(dD^3)$ . Here the $A$ -matrices are viewed as three-index objects $A_{l_k r_k \sigma_k}$ with dimension $D \times D \times d$ . All sites left of site $k$ are represented by a $D \times D$ matrix, say $L_{l_k}^{l_k}$ . Contracting this with the matrix at site $k$ yields the object $\sum_{l_k} L_{l_k}^{l_k} A_{l_k r_k \sigma_k}$ , which has dimensions $D \times D \times d$ , and since the s contains $D$ terms, the overall cost is $\mathcal{O}(dD^3)$ . . . . .	25
2.8	Partial products associated with site $k$ . . . . .	26
2.9	Density Matrix . . . . .	26
2.10	Reduced density matrix a) $\rho_{\{k\}}$ for site $k$ and b) $\rho_{\{kk'\}}$ for sites $k$ and $k'$ , where $k < l < k'$ . . . . .	27
2.11	The $k$ -left-representation of the operator $B$ , obtained from its $(k-1)$ -local-representation. . . . .	28
2.12	The $k$ -left-representation of the operator $C$ , obtained from its $(k-1)$ -left-representation. . . . .	28
2.13	Iterative calculation of the $k$ -left-description of an operator $B$ , given in the $i$ -local-description, by Eqs. (2.23) and (2.24) for any $k > i$ . . . . .	28
2.14	The $(j+1)$ -left-representation of the operator $C$ , given in the $j$ -local-representation, and $B$ , given in the $j$ -left-representation. . . . .	29
2.15	The nearest neighbour hopping term $c_k^\dagger c_{k+1}$ acting on $ \psi\rangle$ in the global view. . . . .	29
2.16	The nearest neighbour hopping term $c_k^\dagger c_{k+1}$ acting on $ \psi\rangle$ in the local view. . . . .	30
2.17	The expectation value of the nearest neighbour hopping $c_k^\dagger c_{k+1}$ in a) the global view and b) the local view. . . . .	30
2.18	One complete sweep. . . . .	31
2.19	The minimization problem expressed in the current site. . . . .	31
2.20	Iterative calculation of the operator $H_L^{(k+1)}$ . The sum over $i$ indicates that $H_{L,\bullet}^{(k)}$ has the form $\sum_i H_{L,i}^{(k)} \otimes H_{\bullet,i}^{(k)}$ , where $H_{L,i}^{(k)}$ acts only on sites $k' < k$ and $H_{i,\bullet}^{(k)}$ only on site $k$ . The calculation of $H_R^{(k-1)}$ works analogously. . . . .	33

2.21	The operators, calculated in an extended switch from site $k$ to site $k + 1$ , for the Hamiltonian in Eq. (1.5) with site $k + 1$ as current site. The operators a) are needed for the nearest neighbour hopping along legs, the operators b) are needed for the nearest neighbour repulsion along legs and the operators c) are needed for the correlated hops. The extended switch from site $k$ to site $k - 1$ works analogously. . . . .	34
2.22	Two ways of contracting the operators $B_L$ acting on the effective left basis, $B$ acting on the local basis and $B_R$ acting on the effective right basis onto an $A$ -matrix: a) The efficient way, where the three operators are contracted onto $A$ step by step. Its numerical cost is of order $\mathcal{O}(dD^2(D + D + d))$ (the resulting object always consists of $dD^2$ entries, and matrix multiplications by $B_L$ , $B$ or $B_R$ involves summing over an index with dimension $D$ , $d$ , or $D$ respectively). b) The inefficient way, where the three operators are contracted onto $A$ in one step. It is of order $\mathcal{O}(d^2D^4)$ (the resulting object consists of $dD^2$ entries and one applies $dD^2$ multiplications for each value). . . . .	35
3.1	The steps which lead to a description of the infinite lattice via $A$ -matrices. . . . .	38
3.2	The expectation value $\langle c_1^\dagger c_2 \rangle$ as generalized from Sec. 2.1.9. The block in the middle, where the operators are acting, is the operator block. . . . .	40
3.3	Calculation of expectation values via $\mathcal{P}$ . The expectation value $\langle c_1^\dagger c_2 \rangle$ , expressed by the operator block $\mathcal{O}$ and $\mathcal{P}$ . In this case there is only one operator block. For $\langle c_1^\dagger c_{M+1} \rangle$ two operator blocks, $\mathcal{O}_1$ and $\mathcal{O}_2$ , would arise. . . . .	40
3.4	The expectation value $\langle c_1^\dagger c_2 \rangle$ , expressed by the operator block $\mathcal{O}$ , $\mathcal{P}$ and the overlap matrices for the left and the right part. . . . .	41
3.5	$\mathcal{P}$ with its largest left and right eigenvectors. . . . .	41
3.6	The expectation value $\langle c_1^\dagger c_2 \rangle$ calculated by the finite expression Eq. (3.7). . . . .	42
3.7	Reduced density matrix $\rho_{kk'}$ , where the sites $k$ and $k'$ are within one block (e.g. $k = 1$ and $k' = M$ ). . . . .	42
3.8	The Hamiltonian in Eq. (1.5) divided into four parts, where all terms within one part commute. Single bars denote local terms (rung hopping and nearest neighbour repulsion along rungs), bars connecting two sites denote nearest neighbour interaction (leg hopping and nearest neighbour repulsion along legs) and bars connecting three sites denote correlated hops. . . . .	43
3.9	The action of $e^{-\tau H_1}$ onto the infinite matrix product state for the Hamiltonian in Eq. (1.5) with $M = 4$ . . . . .	44
3.10	Decomposition of the object resulting out of Eq. (3.10) in two steps. . . . .	44

- 5.1 Ground state energy per unit cell  $E$  and the corresponding error for several chain lengths. The black curve shows the exact result for finite chains. The numerical results are divided into even (blue) and odd (red) chain lengths. a) The ground state energy per unit cell of the infinite chain  $E_{\text{exact}}^{\infty}$  is used as reference energy to see how good the finite chain simulates the infinite system. The x-axis shows the inverse chain length  $\frac{1}{N}$ , which can be extrapolated to  $N \rightarrow \infty$ , i.e.  $\frac{1}{N} \rightarrow 0$ . b) The relative error of the DMRG results with respect to the exact result for finite chain length  $E_{\text{exact}}$ . . . . . 55
- 5.2 Ground state filling  $\nu$  and the corresponding error for several chain lengths. The black curve shows the exact result for finite chains. The numerical results are divided into even (blue) and odd (red) chain lengths. a) Chain filling. b) Relative error, where  $\nu_{\text{exact}}$  is the filling of the exact result for finite chain length. 55
- 5.3 Correlation functions as introduced in Sec. 1.2.1 for chain length  $N = 99$  calculated relative to site 25. All correlation functions are plotted versus the distance  $r$ . a) The FL correlation function. Only odd distances are plotted because the even ones are zero in the exact case. b) The CDW correlation function. Again only odd distances are plotted. c) The SC correlation function. For all three cases the error for the values that are zero in the exact case is about  $10^{-4}$  and the relative error for the non-zero values is about  $10^{-2}$  up to distances of 20. . . . . 56
- 5.4 The symmetry ordered weights of the correlation density matrices as a function of distance. Cluster  $A$  is fixed on the sites (25, 26) and cluster  $B$  separated from it by  $r$  sites, starting from sites (27, 28) on to the right. The light, solid curves show the weights of the CDM, the dark, solid curves the polynomial fit and the dashed curves the analytical correlation function for the infinite chain. The polynomial fits  $cr^{-2\alpha}$  (the factor of two in the exponent accounts for the singular values being squared) yield the following critical exponents:  $\alpha$  (CDW) = 2.02,  $\alpha$  (FL) = 0.94 and  $\alpha$  (SC) = 2.02, which is in acceptable agreement with the exact results, namely  $\alpha_{\text{exact}}$  (CDW) = 2,  $\alpha_{\text{exact}}$  (FL) = 1 and  $\alpha_{\text{exact}}$  (SC) = 2 as can be seen in Sec. 1.2. Even and odd distances have been fitted separately and the middle of these two fits is used. The range of  $r$ -values that was used for the fitting has been shaded grey. . . . . 58
- 5.5 Ground state energy and the corresponding error for several chain lengths for  $t_{\perp} = 1$ , otherwise as plotted in Fig. 5.1. For more information see the caption of that figure. . . . . 59
- 5.6 Ground state filling and the corresponding error for several chain lengths, otherwise as plotted in Fig. 5.2. For more information see the caption of that figure. . . . . 59
- 5.7 The three correlation functions for a chain with length  $N = 100$ , with reference to site 25: a) FL, but only values that are non-zero in the exact result are plotted. b) CDW, again with only non-zero values of the exact case plotted. c) SC. See Fig. 5.3 for a detailed explanation. The errors are within the same range as for the zero inter-leg hopping. . . . . 60

- 5.8 The symmetry ordered weights of the correlation density matrices as a function of distance. Cluster  $A$  is fixed on the sites (25, 26) and cluster  $B$  moves from sites (27, 28) to the right. See Fig. 5.4 for a detailed explanation. The fitted critical exponents  $\alpha$  as in  $cr^{-2\alpha}$  are:  $\alpha(\text{CDW}) = 1.79$ ,  $\alpha(\text{FL}) = 0.80$  and  $\alpha(\text{SC}) = 1.80$ , which is not in good agreement with the exact results  $\alpha_{\text{exact}}(\text{CDW}) = 2$ ,  $\alpha_{\text{exact}}(\text{FL}) = 1$  and  $\alpha_{\text{exact}}(\text{SC}) = 2$ , but gives the correct tendency and the correct dominant correlation. . . . . 61
- 5.9 The number of sweeps (upper number) with dimension  $D = 64$  and the grade of convergence with respect to Eq. (2.34) (lower number, not  $\varepsilon$  is plotted, but  $\log_{10}(\varepsilon)$ ) for all calculated ground states. The colouring scheme is determined by the grade of convergence, where white denotes good convergence and blue bad convergence. The result for  $N = 100$ ,  $t_{\perp} = 0.01$  and  $t_c = 0.01$  is converged very bad despite of many sweeps. After a closer investigation, we found that it had been stuck in a local minimum for about 30 sweeps, because in that sweep the energy dropped drastically over a few site optimizations and started to converge again afterwards. . . . . 62
- 5.10 The maximal bond entropy  $e^S$  along the chain for all calculated ground states. We calculated the bond entropy for all bonds of the chain and took the largest value for each chain for this plot. . . . . 63
- 5.11 The ratio of the largest singular value to the smallest  $\frac{s_D}{s_1}$  along the chain. From the calculation of the bond entropy we had a singular value spectrum for each bond and calculated the ratio of the first (largest) singular value to the  $D$ th (smallest kept) singular value. The maximal ratio for each chain is plotted. . . . . 63
- 5.12 The complete singular value spectrum of the bond between site 50 and site 51 for a chain length of  $N = 99$  (blue) and  $N = 100$  (red). There are  $D = 64$  singular values plotted. The remaining singular values (in total there are  $dD$ ) are zero by construction of variational single site DMRG. . . . . 64
- 5.13 The deviation of the total particle number  $N_{\text{tot}}$  from an integer number for all calculated results:  $\Delta N_{\text{tot}} = |N_{\text{tot}} - \text{round}(N_{\text{tot}})|$ , but the plot shows  $\log_{10}(\Delta N_{\text{tot}})$ . One can clearly see that ground states with good numerical convergence have smaller values of  $\Delta N_{\text{tot}}$ . . . . . 65
- 5.14 The ground state filling for all our calculations. The colouring scheme is chosen such that white corresponds to quarter filling. . . . . 65

- 5.15 Average occupancy and correlation functions for a chain of length  $N = 99$  around rung 49 ( $V = 10^4$ ,  $t = 1$ ). The solid lines correspond to the upper leg and the dashed lines correspond to the lower leg. a) The average occupancy. One can clearly see that one only has values distinct from zero which always allow for correlated hops and thus may form hard-core bosons. b) The correlation function  $C_{\text{FL}}(49, |i - 49|) = \langle c_{a,i}^\dagger c_{\uparrow,49} \rangle$ . The non-vanishing values for the upper sites of rungs 47 and 51 require an occupied site on the lower leg at rungs 48 and 50, respectively. c) The correlation function  $C_{\text{CDW}}(49, |i - 49|) = \langle n_{a,i} n_{\uparrow,49} \rangle$ . This correlation function yields no more information than the average occupancy. . . . . 67
- 5.16 The bond entropy along the whole chain with chain length  $N = 99$ . On a first glance the bond entropy looks very irregular (cyan curve), but on a closer look it reveals regularity. Interestingly, if one arranges the sites in intervals of three sites (sites 1,4,... - red curve; sites 2,5,... - green curve; sites 3,6,... - blue curve) they show oscillating behaviour. . . . . 68
- 5.17 Average occupancy and correlation functions for a chain of length  $N = 99$  around rung 50 ( $V = 10^4$ ,  $t = 1$ ). The solid lines correspond to the upper leg and the dashed lines correspond to the lower leg. a) The average occupancy. One can clearly see the alternating behaviour of occupancy, which indicates the staggered ground state. b) The correlation function  $C_{\text{FL}}(50, |i - 50|) = \langle c_{a,i}^\dagger c_{\uparrow,50} \rangle$ . The confinement of a particle between two other particles shows up. c) The correlation function  $C_{\text{CDW}}(50, |i - 50|) = \langle n_{a,i} n_{\uparrow,50} \rangle$ . This correlation function yields no more information than the average occupancy. . . . . 69
- 5.18 The bond entropy along the whole chain for a chain length of  $N = 99$ . The entropies of all bonds (cyan curve) is divided into the entropies of even (green curve) and odd (red curve) bonds. . . . . 70
- 5.19 Average occupancy and correlation functions for a chain of length  $N = 99$  around rung 49 ( $V = 10^4$ ,  $t = 1$ ). The solid lines correspond to the upper leg and the dashed lines correspond to the lower leg, but due to the dominating inter-leg hopping the ground state is symmetric under leg interchange and the lines coincide for the most part. a) The average occupancy. The fermions are delocalized on the odd legs. b) The correlation function  $C_{\text{FL}}(49, |i - 49|) = \langle c_{a,i}^\dagger c_{\uparrow,49} \rangle$ . Current is only possible along rungs due to the infinite nearest neighbour repulsion. c) The correlation function  $C_{\text{CDW}}(49, |i - 49|) = \langle n_{a,i} n_{\uparrow,49} \rangle$ . This correlation function yields no more information than the average occupancy. . . . . 71

- 5.20 Average occupancy and correlation functions for a chain of length  $N = 100$  around rung 49 ( $V = 10^4$ ,  $t = 1$ ). The solid lines correspond to the upper leg and the dashed lines correspond to the lower leg, but due to the dominating inter-leg hopping the ground state is symmetric under leg interchange and the lines coincide for the most part. a) The average occupancy. The fermions are delocalized on the rungs and one has a superposition of the two states, where the fermions are on the even and odd rungs, respectively. There seems to be a relative phase between the two ground states and thus one obtains oscillating behaviour. b) The correlation function  $C_{\text{FL}}(49, |i - 49|) = \langle c_{a,i}^\dagger c_{\uparrow,49} \rangle$ . Current is only possible along rungs due to the infinite nearest neighbour repulsion. c) The correlation function  $C_{\text{CDW}}(49, |i - 49|) = \langle n_{a,i} n_{\uparrow,49} \rangle$ . This correlation function picks one of the two degenerate states, in this case the one with fermions on the odd rungs, and shows its CDW behaviour. The asymmetry comes from the fact, that a division of a chain with even length into two parts left and right of one site is already asymmetric. If one chooses site 50 for the division the picture is mirrored. . . . . 72
- 5.21 The bond entropy for chain with length  $N = 99$ . The small value, which is constant over nearly the full chain indicates a product state. . . . . 73
- 5.22 The bond entropy for a chain with length  $N = 100$ . One can see the even-odd structure of the bond entropy. . . . . 73
- 5.23 The three symmetry weights for CDW, FL and SC correlations. The FL correlations are the greatest for short distances, but decay exponentially fast and have no influence on the long-range behaviour. The CDW and SC correlations decay as a power law and a fitting is applied to obtain the exponent. The range that was used for the fitting has been shaded in grey. For the CDW correlations the extracted exponent  $\alpha(\text{CDW}) = 1.17$  fits good to the exact result  $\alpha_{\text{exact}}(\text{CDW}) = 1.125$ . The exact curve is plotted for comparison, whereas the constant factor of the power law is chosen such that the curves are close together. We do not have an exact value for this constant. The SC correlation does not yield such an agreement, the extracted exponent  $\alpha(\text{SC}) = 1.06$  is more than twice the exact value of  $\alpha_{\text{exact}}(\text{SC}) = 0.5$ . . . . . 75
- 5.24 The exponential decay of the FL correlation. The range that was used for the fitting has been shaded in grey. One can clearly see the exponential decay down to values below  $10^{-20}$ . . . . . 76

5.25	The three symmetry weights for CDW, FL and SC correlations. The FL correlations are about the greatest for short distances, but decay exponentially fast and have no influence on the long-range behaviour. The CDW and SC correlations decay as a power law and a fitting is applied to obtain the exponent. The range that was used for the fitting has been shaded in grey. For the CDW correlations the extracted exponent $\alpha(\text{CDW}) = 0.83$ does not fit very well to the exact result $\alpha_{\text{exact}}(\text{CDW}) = 0.5$ . The SC correlation yields a better agreement, the extracted exponent $\alpha(\text{SC}) = 2.13$ is close to the exact value of $\alpha_{\text{exact}}(\text{SC}) = 2$ . The exact curves are plotted for comparison, whereas the constant factors of the power law are chosen such that corresponding curves are close together. We do not have exact values for these constants. . . . .	77
5.26	The exponential decay of the FL correlation. The range that was used for the fitting has been shaded in grey. One can clearly see the exponential decay down to values below $10^{-20}$ . . . . .	78
5.27	Correlations for the chain with length $N = 99$ . The correlations have a very small value for $r = 2$ and decay afterwards. From these small values one cannot extract any conclusive information. . . . .	79
5.28	Correlations for the chain with length $N = 99$ . The FL and SC correlations decay quickly. The CDW correlations decay very slow, but it is unclear in which way. . . . .	79
A.1	Ordering scheme for the ladder model . . . . .	85

# List of Tables

- 1.1 Leading correlation exponents of the correlation functions that decay as power laws. Most of them are universal, but some depend on the filling fraction. Taken from [2]. . . . . 14



# Bibliography

- [1] S.-A. Cheong and C. L. Henley. Correlation density matrix: an unbiased analysis of exact diagonalizations. *to be published*.
- [2] S.-A. Cheong and C. L. Henley. Exact ground state and correlation functions of chain and ladder models of interacting hardcore bosons or spinless fermions. *to be published*.
- [3] U. Schollwöck. The density-matrix renormalization group. *Reviews of Modern Physics*, 77(1):259, 2005.
- [4] F. Verstraete, A. Weichselbaum, U. Schollwöck, J. I. Cirac, and J. von Delft. Variational matrix product state approach to quantum impurity models. *condmat/0504305*.
- [5] A. M. Holzner. Matrix product state approach for a multi-lead anderson model. Master's thesis, Fakultät für Physik der Ludwig-Maximilians-Universität München, 2006.
- [6] J. Dukelsky, M. A. Martín-Delgado, T. Nishino, and G. Sierra. Equivalence of the variational matrix product method and the density matrix renormalization group applied to spin chains. *Europhys. Lett*, 43:pp. 457–462, 1998.
- [7] G. Vidal. Classical simulation of infinite-size quantum lattice systems in one spatial dimension. *Physical Review Letters*, 98(7):070201, 2007.
- [8] F. Verstraete and J. I. Cirac. Mapping local hamiltonians of fermions to local hamiltonians of spins. *Journal of Statistical Mechanics: Theory and Experiment*, 2005(09):P09012, 2005.
- [9] J. W. Demmel. *Applied numerical linear algebra*. SIAM, Philadelphia, 1997.
- [10] A. Weichselbaum. *to be published elsewhere*.
- [11] G. Vidal. Efficient classical simulation of slightly entangled quantum computations. *Phys. Rev. Lett.*, 91(14):147902, Oct 2003.
- [12] G. Vidal. Efficient simulation of one-dimensional quantum many-body systems. *Phys. Rev. Lett.*, 93(4):040502, Jul 2004.
- [13] S. R. White and A. E. Feiguin. Real-time evolution using the density matrix renormalization group. *Phys. Rev. Lett.*, 93(7):076401, Aug 2004.

- [14] M. Suzuki. Fractal decomposition of exponential operators with applications to many-body theories and monte carlo simulations. *Physics Letters A*, 146(6):319–323, June 1990.
- [15] P. Jordan and E. Wigner. Über das paulische äquivalenzverbot. *Zeitschrift für Physik*, 47:631–651, September 1928.
- [16] H. R. Schwarz. *Numerische Mathematik*. Teubner, 1997.

# Acknowledgements

At the end of this thesis, I would like to thank all people, who were involved in this thesis.

Prof. Dr. Jan von Delft for the opportunity to join his group and his advice.

My adviser Andreas Weichselbaum, who was always there for my questions. I learned a lot from him.

Christopher L. Henley for discussions about the physical background of my thesis.

Andreas Holzner, helping me in the first few weeks with the entrance into numerical physics and Linux.

Alex Buchner and Sefa Arslan for being my roommates over several months. I enjoyed physical and non-physical discussions very much.

All people from the Chair for Theoretical Condensed Matter Physics at the LMU. All of you create a great climate in a very friendly group.

The team of the rbg, first of all Ralf Simmler, for keeping the computers up and running (and setting my quota higher and higher).

My parents Renate and Hacki Mnder for being always there.

My fiancée Sandra Eberheißinger for bringing my mind back to the essentials.